Pushing the boundaries of the LHCb rare decays program: search for the Λ0b→ Λγ decay

Carla Marin Benito

PhD thesis

Pushing the boundaries of the LHCb rare decays program: search for the $\Lambda_b^0 \to \Lambda\gamma$ decay

Carla Marin Benito

supervised by
Dr. Lluís Garrido Beltrán
Dr. Albert Puig Navarro

February 2018

UNIVERSITAT DE BARCELONA

Pushing the boundaries of the LHCb rare decays program: search for the $\Lambda_b^0 \to \Lambda\gamma$ decay

Memòria presentada per optar al grau de doctor per la

Universitat de Barcelona

Programa de doctorat en Física

Autora:
Carla Marin Benito

Directors:
Dr. Lluís Garrido Beltrán
Dr. Albert Puig Navarro

Tutor:
Dr. Joan Soto Riera

UNIVERSITAT DE
BARCELONA

Aknowledgments

Contents

Resum

Aquesta tesi té per objectiu l'estudi i comprovació del Model Estàndard (MS) de la física de partícules utilitzant les dades enregistrades pel detector LHCb. Aquest marc tèoric ha demostrat un gran èxit en la descripció dels resultats obtinguts pels experiments però hi ha fenòmens que no es capaç d'explicar, com la gravetat, la matèria i enèrgia fosques, l'asimètria entre matèria i anti-matèria i la massa dels neutrins. És per això que noves teories es desenvolupen contínuament i cal explorar experimentalment aquells esdeveniments observables per als quals les seves prediccions disten de les del MS, doncs la seva mesura permet discernir la teoria correcta.

Processos rars

Amb aquest pròposit ens centrem en l'anàlisi de processos rars, aquells que estan molt suprimits al MS, concretament en desintegracions radiatives d'hadrons b i decaïments rars de mesons estranys. Ambdós són exemples de Corrents Neutres de Canvi de Sabor (CNCS), els quals estan prohibits al MS a nivell àrbre i només tenen lloc a través de cercles, fet que els fa molt sensibles a possibles noves partícules entrant en ells. Des del punt de vista teòric, dos efectes es barrejen a l'hora de fer prediccions sobre aquests processos, un que governa la transició a nivell dels quarks, mitjançada per la interacció electrofeble, i l'altre relacionat amb l'hadronització dels quarks degut a la força forta. L'Expansió en Productes d'Operadors (OPE) és una teòria efectiva que permet separar-los concentrant els efectes de curta distància en els anomenats coeficients de Wilson i la part no pertorbativa de la teoria cromodinàmica en un conjunt d'operadors locals. Donat un conjunt complet d'aquests operadors es pot descriure qualsevol procés com la suma dels elements rellevants. Amb la mesura de processos lliures de contribucions de nova física es pot restringir el valor dels coeficients en el MS i per comparació amb observables sensibles a efectes més enllà del MS, com els CNCS, detectar si aquests són presents. Les prediccions obtingudes utilitzant aquest tipus de tècniques pels casos estudiats en aquesta tesi estan presentades a les seccions rellevants.

El detector LHCb

Les dades utilitzades en aquesta tesi han estat enregistrades pel detector LHCb en col·lisions protó-protó (pp) produïdes a l'LHC, l'accelerador de partícules més gran del món. Durant el primer període de funcionament, entre els anys 2010 i 2012, conegut com a Run 1, les col·lisions es van produïr a energies al centre de masses de 7 i 8 TeV. Al 2015 va començar una segona etapa, coneguda com a Run 2, amb un increment en l'energia fins als 13 TeV.

LHCb va ser dissenyat per a l'estudi de violacions de la simètria de càrrega-paritat i decaïments rars d'hadrons b i c però el programa de física s'ha ampliat importantment a altres àrees de recerca, com les col·lisions d'hadrons pesats, les cerces de partícules exòtiques i l'estudi d'hadrons s.

En les col·lisions pp que tenen lloc a l'LHC les parelles $b\bar{b}$ es produeixen molt paral·leles a la direcció dels feixos incidents. Per explotar aquesta característica, LHCb va ser construit com un espectròmetre d'un sol braç amb una cobertura angular de 15 a 300 mrad en el pla horitzontal, sotmés a l'efecte de curvatura de l'iman, i de 15 a 250 mrad en el vertical, com es mostra a la Fig. 1.
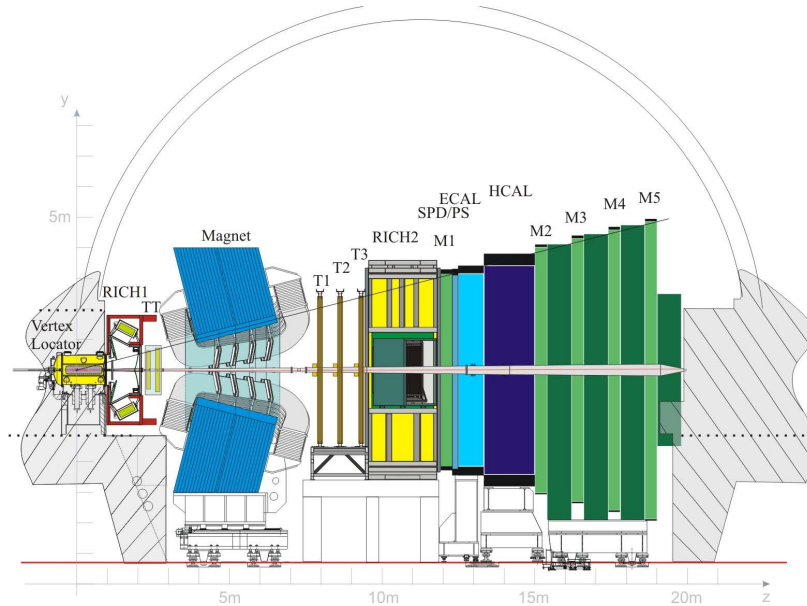
Figure 1: Vista lateral del detector LHCb.

El detector està equipat amb un sistema de reconstrucció de traces que permet mesurar el moment de les partícules carregades amb una precisió que varia del 0.5% a baix moment fins al 1.0% a 200 MeV. A més, gràcies al precís localitzador de vèrtexs (VELO), s'aconsegueix una resolució en el paràmetre d'impacte d'una traça respecte del punt d'interacció o vèrtex primari (PV) que escala inversament amb el seu moment tranvers com $(15 + 29/p_{\mathrm{T}}[\,\mathrm{GeV}])\,\mu$m. Aquestes característiques permeten explotar una de les particularitats principals dels hadrons b, que és el recorregut d'una distància finita dins del detector abans de decaure, donant lloc a traces desplaçades respecte el PV.

El programa central d'LHCb implica l'estudi de decaïments de partícules pesades a estats finals exclusius. Això requereix una indetificació i separació precisa de les diferents espècies que en resulten que s'aconsegueix per mitjà del sistema de detecció de partícules, convinant la informació del qual es construeixen variables que donen la probabilitat que una partícula reconstruïda pertanyi a una espècie o una altra. El poder de separació d'aquestes variables permet típicament identificar correctament un 95% dels kaons amb tan sols una probabilitat d'indentificació incorrecta $\pi \rightarrow K$ del 5%. En el cas de les partícules neutres, la reconstrucció, mesura del moment i identificació té lloc exclusivament als calorímetres, formats per un conjunt de detectors amb diferents gruixos i longituds de radiació que permeten distingir-les. D'especial interés per a l'estudi de modes de desintergació radiatius és la distinció entre π^0 i photons a altes energies. Durant els primers anys de funcionament del detector s'ha aconseguit una selecció del 98% dels fotons amb un rebuig al mateix temps del 45% dels π^0.

Utilitzant informació de tots aquests detectors, el sistema activador (trigger) fa un primer filtrat de les dades per destriar dels 40 MHz de col·lisions que proporciona l'LHC només aquelles que són d'interés per a la física que es vol realitzar. El trigger està dividit en dos nivells: el L0, implementat en hardware, i l'HLT basat en software. El primer selecciona senyals d'alt moment transvers (p_{T}) i rebutja esdeveniments d'alta complexitat, reduint el volum de dades per sota d'1 MHz, al qual es pot llegir i processar la informació de tots els detectors. L'HLT està sots-dividit al seu torn en dos sots-nivells: l'HLT1 selecciona traces d'alt p_{T} desplaçades del PV i l'HLT2 realitza una reconstrucció completa de l'esdeveniment i convina filtres inclusius i exclusius.

El trigger inclusiu per a modes radiatius al Run 2

Per als processos rars és clau tenir totalment optimitzat el filtratge d'esdeveniments a nivell de trigger, doncs degut a la seva extremadament baixa producció cal seleccionar-ne una alta proporció reduint al mateix temps l'alt fons que es genera en les col·lisions pp. El disseny flexible de l'HLT2 permet la incorporació d'algoritmes dedicats a la selecció de processos concrets. Durant el Run 1, els decaïments radiatius van ser filtrats primer amb seleccions totalment exclusives dels principals modes d'interés i després amb algoritmes inclusius que requerien la presència d'un fotó d'alta energia transversa (E_{T}) a l'estat final. El major inconvenient d'aquest HLT2 era el fet que la selecció no estava optimitzada especialment per a esdeveniments radiatius sinó que provenia d'un filtre genèric per a decaïments d'hadrons b. Això va motivar el desenvolupament d'una selecció totalment dedicada per al Run 2.

Selecció

La nova selecció d'HLT2 per a processos radiatius segueix una estratègia inclusiva basada en algoritmes multivariats. Dues configuracions, denominades `Hlt2RadiativeIncHHGamma` i `Hlt2RadiativeIncHHHGamma` seleccionen respectivament combinacions de dos i tres traces més un fotó d'alta E_{T}. En primer lloc, es requereix que els fotons hagin passat el nivell L0 del trigger a través de les línies[1] `L0Electron` or `L0Photon` i les traces el nivell HLT1 a través de `Hlt1TrackMVA` or `Hlt1TwoTrackMVA`. Després es creen els candidats de dos i tres traces, de forma compartida amb la selecció genèrica de decaïments d'hadrons b per estalviar temps de processament, i a continuació s'hi afegeix el fotó, aplicant una selecció suau.

Finalment els candidats es filtren amb la selecció multivariada. Per a la seva implementació s'escull un algoritme Bonsai Boosted Decision Tree (BBDT) que es basa en la discretització de les variables d'entrada d'un Boosted Decision Tree (BDT) per a guanyar estavilitat davant les fluctuacions de les dades utilitzades en l'entrenament i possibles discrepàncies entre mostres de Monte-Carlo (MC) i dades. Presenta també l'avantatge que la seva resposta és constant a cadascun dels hypercubs de la xarxa n-dimensional de les variables d'entrada discretitzades i per tant no cal executar l'algoritme per a cada esdeveniment. Per contra, el nombre total de respostes possibles es pot guardar en una taula de consulta juntament amb la hyper-cel·la corresponent que només cal llegir al trigger, amb el corresponent guany en velocitat d'execució. Aquest algoritme s'entrena amb candidats creats com s'ha explicat anteriorment a partir de mostres de MC reproduïnt el fons i varis modes de desintegració radiatius, explotant les característiques comunes dels processos radiatius. El punt de treball triat ve limitat pel volum màxim de dades assignat al grup de radiatius i s'equilibra entre les dues configuracions.

Rendiment

Les eficiències obtingudes per les BBDTs per a les diferents mostres de senyal utilizades es poden trobar a la Taula 1 i representen un augment absolut mínim en la eficiència del 20%. Per a casos amb topologia especial, com $B^0 \to K^+\pi^-\gamma$ i $B^+ \to K^{*+}\gamma$ el guany arriba al 70% i 60%, respectivament. Com es mostra a la taula, les BBDTs van ser millorades per al 2016, gràcies a la disponibilitat d'una mostra de fons provinent de dades reals extreta de les col·lissions que van tenir lloc durant el 2015. A més de millorar l'eficiència en senyal, la nova selecció guarda un volum total de dades menor a la anterior amb el conseqüent aprofitament d'aquest remanent per a noves línies dedicades a modes amb topologia especial que no podien ser seleccionats al trigger anteriorment. És a dir, que el desenvolupament del nou HLT2 inclusiu de radiatius ha permés directament i indirecta l'increment del nombre d'esdeveniments de senyal d'aquests processos seleccionats a nivell de trigger, propiciant l'expansió del programa de física en la investigació d'aquests modes. El correcte funcionament de les noves línies al trigger de l'experiment va ser validat amb les dades presses durant el 2015.

---

[1] En el context d'LHCb s'anomena sovint línies a les seleccions incloses al trigger.

Table 1: Comparació de l'eficiència dels triggers inclusius radiatius entre les configuracions de 2015 i 2016 per a les diferents mostres MC de senyal emprades en l'optimització de les seleccions.

Decay	Hlt2RadiativeIncHHGamma		Hlt2RadiativeIncHHHGamma	
	2015	2016	2015	2016
$B^0 \to K^+\pi^-\gamma$	0.935±0.007	0.964±0.008		
$B^0 \to K^{*0}\gamma$	0.927±0.007	0.971±0.007		
$B^+ \to K^{*+}\gamma$	0.75±0.02	0.73±0.02		
$B_s^0 \to \phi\gamma$	0.941±0.07	0.972±0.07		
$\Lambda_b^0 \to \Lambda^*\gamma$	0.930±0.007	0.964±0.007		
$B^+ \to K_1(1270)\gamma$	0.838±0.007	0.908±0.007	0.695±0.0076	0.971±0.008
$B_s^0 \to \phi\phi\gamma$	0.279±0.004	0.298±0.004	0.449±0.006	0.938±0.009

Estudi de viabilitat del mode $K_s^0 \to \pi^+\pi^- e^+ e^-$ a LHCb

LHCb ha demostrat que tot i no estar dissenyat per a aquest tipus de física pot aportar resultats molt competitius en l'àrea d'estudi de modes rars i estranys. Entre els canals de decaïment d'interés destaquen els de $K_s^0 \to \ell^+\ell^-\ell^+\ell^-$ on ℓ pot ser tant un electró com un muó. Aquests modes no han estat observats mai abans i el MS prediu unes fraccions d'embrancament molt suprimides de l'ordre de 10^{-10}, 10^{-11} i 10^{-14} per $K_s^0 \to e^+e^-e^+e^-$, $K_s^0 \to \mu^+\mu^-e^+e^-$ i $K_s^0 \to \mu^+\mu^-\mu^+\mu^-$, respectivament. La introducció de termes de nova física en l'amplitud d'aquests processos podria representar contribucions dominants i per tant qualsevol desviació respecte aquestes prediccions seria una senyal de física més enllà del MS.

Pels modes amb electrons en l'estat final, la reconstrucció d'aquests és el punt més complicat degut al baix moment que tenen en aquests processos i a la seva pèrdua d'energia per la radiació de Bremsstrahlung. Estudis preliminars amb MC demostren que la resolució experimental permet distingir el pic de massa provinent d'aquests decaïments del format per l'abundant $K_s^0 \to \pi^+\pi^- e^+ e^-$, el fons més perillós, però el solapament entre les cues de les distribucions és alt i per tant cal tenir molt ben controlat aquest fons per poder estudiar les senyals. A més aquest mode és també un candidat ideal per utilitzar com a canal de normalització i control donada la semblant topologia. Per tant, en un primer pas cap a l'estudi dels modes de desintegració $K_s^0 \to \ell^+\ell^-\ell^+\ell^-$, s'ha evaluat la viabilitat d'observar el canal $K_s^0 \to \pi^+\pi^- e^+ e^-$ a LHCb. Aquest ha sigut ja observat i estudiat a altres experiments, amb una mesura de la seva raó d'embrancament de $\mathcal{B}(K_s^0 \to \pi^+\pi^- e^+ e^-) = (4.79 \pm 0.15) \times 10^{-5}$.

Possibilitat d'observació amb dades del Run 1

L'anàlisi se centra en l'estudi de les eficiències de reconstrucció i selecció d'aquest mode a LHCb a partir de mostres de MC de senyal i fons reproduint les condicions de la pressa de dades del 2012. Per a això es desenvolupa una selecció basada en requeriments lineals en variables cinemàtiques i topològiques que permet filtrar un 10% de la senyal rebutjant un 99.997% de l'abundant fons. A nivell de trigger, com durant el Run 1 no hi havia cap línia dedicada a seleccionar aquests esdeveniments, s'estudia l'eficiència de totes les disponibles contemplant tant la possibilitat que aquest es dispari degut a la presència de la senyal (Trigger On Signal o TOS) o independentment d'aquesta (Trigger Independent of Signal o TIS). Només un candidat del MC de $K_s^0 \to \pi^+\pi^- e^+ e^-$ és seleccionat i això s'aconsegueix amb la combinació L0 TOS, HLT1 TOS i HLT2 TOS. Les línies concretes que filtren aquest esdeveniment rebutjen tot el fons de la mostra de MC i per tant els estudis de la senyal esperada en dades es fan amb aquesta condició.

Utilitzant les eficiències obtingudes del MC, s'espera una senyal de $N_{sig}^{exp} = 120^{+280}_{-100}$ amb un fons $N_{bkg}^{exp} \leq 6.1 \times 10^5$ per fb^{-1} en condicions del Run 1. Les seleccions descrites s'apliquen a les dades enregistrades per LHCb durant el 2012 i, tal com es mostra a la Fig. 2 (esquerra), no s'observa cap pic en la distribució de massa invariant mentre que el fons observat, $N_{bkg}^{obs} \sim 6 \times 10^3$, és compatible amb el límit obtingut del MC. Per tal de quantificar la possibilitat d'observació d'aquest mode amb aquestes dades
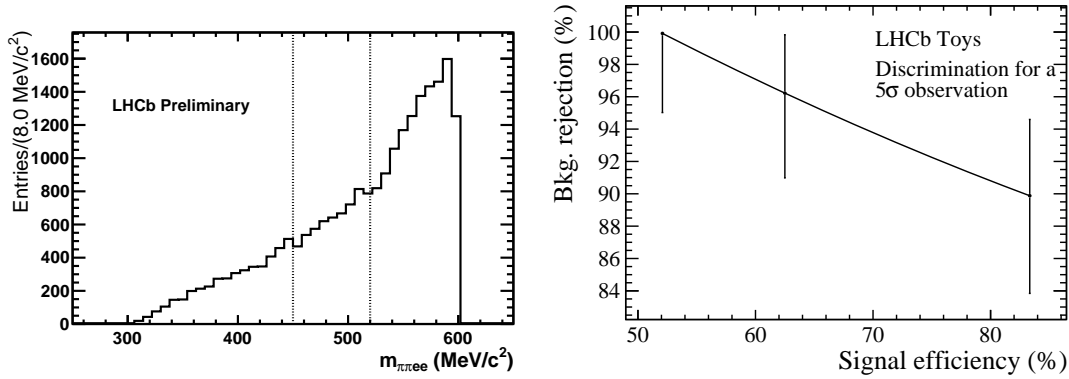
Figure 2: Distribució de la massa invariant $\pi^+\pi^-e^+e^-$ per candidats que satisfan la selecció i el trigger amb la zona de senyal, 450–520 MeV/c^2, delimitada per ratlles discontinues (esquerra) i corva de rebuig de fons respecte eficiència en senyal necessària per obtenir un significat estadísitic de la senyal de 5σ (dreta).

a través d'una selecció extra, es realitza un estudi basat en pseudoexperiments. La corva de rebuig de fons respecte l'eficiència en la selecció de senyal necessària per obtenir una significació estadísitica de la senyal de 5σ es mostra a la Fig. 2 (dreta) amb la conclusió que l'observasió és possible, doncs el poder de separació necessari està dins dels resultats obtinguts habitualment per mètodes de selecció multivariada.

Millores pel Run 2 i més enllà

Els estudis realitzats amb MC i dades del Run 1 demostren que una de les principals limitacions per observar el mode $K_{\mathrm{S}}^0 \to \pi^+\pi^-e^+e^-$ és la baixa eficiència del trigger en la seva selecció. Per aquest motiu, dues línies d'HLT2 van ser desenvolupades per al Run 2. La primera consisteix en una selecció inclusiva que permet filtrar també candidats $K_{\mathrm{S}}^0 \to \ell^+\ell^-\ell^+\ell^-$ amb requeriments molt suaus en el moment transvers de les partícules, explotant altres característiques d'aquests esdeveniments com la gran separació respecte el PV. Aquesta selecció és eficient per candidats que han passat el L0 i HLT1 com a TIS. La segona, selecciona aquells candidats d'alt moment que passen aquests nivells com a TOS i és per tant complementària. Amb aquestes millores la senyal esperada al Run 2 és de $N_{\mathrm{Run2}} = 620^{+290}_{-120}/\,\mathrm{fb}^{-1}$, garantint l'observació d'aquest mode i permetent acumular dades suficients per a fer els primers estudis dels canals $K_{\mathrm{S}}^0 \to \ell^+\ell^-\ell^+\ell^-$.

Millores adicionals significatives requereixen canvis en les configuracions del L0 i l'HLT1, fet que es produirà a partir del 2020, durant la fase Upgrade del detector, on el L0 serà eliminat i el trigger es basarà totalment en software, permetent seleccions molt més específiques. Idealment eficiències $\sim 100\%$ es poden aconseguir en aquestes condicions. Això permetria acumular una senyal de $N_{upgrade} = (5.0 \pm 0.3) \times 10^4/\,\mathrm{fb}^{-1}$ i posar límits restrictius en les fraccions d'embrancament dels decaïments $K_{\mathrm{S}}^0 \to \ell^+\ell^-\ell^+\ell^-$.

Cerca del procés $\Lambda_b^0 \to \Lambda\gamma$ a LHCb

El procés $\Lambda_b^0 \to \Lambda\gamma$ és un CNCS que té lloc a través de la transició a nivell quark $b \to s\gamma$. Com a tal, és molt sensible a efectes de nova física que poden contribuir al cercle de tipus pingüí modificant les propietats respecte les predites pel MS. Mentre els modes de desintegració radiatius de mesons b han sigut estudiats en detall a les fàbriques d'hadrons b i a LHCb, els modes bariònics han estat poc explorats i poden aportar informació complementària. En concret, el canal $\Lambda_b^0 \to \Lambda\gamma$ permet una mesura directa de la polarització del fotó, predit pel MS a ser quasi 100% levogir en aquesta transició, mentre que corrents dextrogirs podrien contribuir en models de nova física modificant aquest observable. Per tant la mesura

d'aquesta quantitat representa una prova molt restrictiva del MS.

Aquest mode de desintegració no s'ha observat encara experimentalment i només es coneix un límit superior en el valor de la seva fracció de ramificació $\mathcal{B}(\Lambda_b^0 \to \Lambda\gamma) < 1.3 \times 10^{-3}$ al 95% de nivell de confiança, mentres que el MS prediu per a aquesta quantitat un valor en el rang $(0.06\text{–}1) \times 10^{-6}$, on les diferències provenen de les varies aproximacions emprades en el càlcul del factor de forma $\Lambda_b^0 \to \Lambda$ que descriu el procés hadrònic. Per tant l'observació d'aquest mode permetria per una banda discernir entre les diferents aproximacions emprades en aquest càlcul i per l'altra obrir les portes a l'estudi de la polarització del fotó en aquest canal.

Reconstrucció i selecció dels candidats

La cerca d'aquest mode de desintegració es realitza utilitzant les dades enregistrades per LHCb en col·lisions pp durant el 2016. La seva particular topologia, marcada per la presència d'una partícula amb un temps mig de vida alt que decau la major part dels cops fóra del VELO, i un fotó, la direcció del qual no es pot mesurar amb els calorímetres d'LHCb, motiva el desenvolupament d'una reconstrucció especial tant a nivell d'anàlisi com al trigger. La topologia descrita impossibilita la reconstrucció del vèrtex de desintegració de la Λ_b^0 i en conseqüència el seu moment s'extreu de la suma directa dels moments mesurats per al fotó i la Λ, amb el conseqüent increment del fons format per combinacions aleatòries d'aquestes dues partícules. Per pal·liar aquest efecte, la selecció inclou requeriments més restrictius en altres variables.

La selecció dels candidats es fonamenta en un primer filtre suau amb requeriments topològics i cinètmàtics seguit d'una BDT. Aquesta s'entrena utilitzant MC per representar les propietats de la senyal i candidats reconstruits en dades amb una massa invariant per sobre dels 5100 MeV com a fons. El requeriment en la massa garanteix que cap possible esdeveniment de senyal present en les dades sigui utilitzat com a fons. Les variables utilitzades com a discriminants es basen també en propietats cinemàtiques del procés. El requeriment en la variable de sortida de la BDT es tria optimitzant la probabilitat d'obtenir una observació de la senyal amb una significació estadística de 5σ i aconsegueix una eficiència en la selecció de la senyal del 33% rebutjant al mateix temps un 99.8% del fons.

Extracció de la fracció de desintegració

Per a minimitzar les incerteses sistemàtiques en la mesura de la fracció d'embrancament, el mode $B^0 \to K^{*0}\gamma$, seleccionat de forma anàloga a la senyal, s'utilitza com a canal de normalització, de manera que la proporció d'esdeveniments observada per cadascuna de les desintegracions ve donada per:

$$\frac{N(\Lambda_b^0 \to \Lambda\gamma)}{N(B^0 \to K^{*0}\gamma)} = \frac{f_{\Lambda_b^0}}{f_{B^0}} \cdot \frac{\mathcal{B}(\Lambda_b^0 \to \Lambda\gamma)}{\mathcal{B}(B^0 \to K^{*0}\gamma)} \cdot \frac{\mathcal{B}(\Lambda \to p\pi^-)}{\mathcal{B}(K^{*0} \to K^+\pi^-)} \cdot \frac{\epsilon_{sel}(\Lambda_b^0 \to \Lambda\gamma)}{\epsilon_{sel}(B^0 \to K^{*0}\gamma)}$$

on $f_{\Lambda_b^0}/f_{B^0}$ és el quocient de les fraccions d'hadronització entre Λ_b^0 i B^0, extret de mesures anteriors d'LHCb; $\mathcal{B}(X)$ és la fracció de ramificació del procés X, ja coneguda per a tots els processos involucrats excepte el d'interés; i $\epsilon_{sel}(X)$ és l'eficiència en la selecció del mode X, extret del MC per a la majoria de requeriments i de dades pels casos en que es disposa de mostres de calibració.

La selecció descrita anteriorment permet separar els esdeveniments de senyal dels de fons però no és un discriminant perfecte i en la mostra filtrada hi ha present encara una part de fons. Per poder obtenir el número d'esdeveniments de senyal, les diferents components han de ser desentrellaçades. Això s'aconsegueix a través d'un ajust simultani de màxima versemblança de les distribucions de la massa invariant del mode de senyal i del de normalització. Per poder extreure el $\mathcal{B}(\Lambda_b^0 \to \Lambda\gamma)$ directament de l'ajust, el nombre d'esdeveniments es descriu com:

$$N(\Lambda_b^0 \to \Lambda\gamma) = \alpha \cdot \mathcal{B}(\Lambda_b^0 \to \Lambda\gamma) \cdot N(B^0 \to K^{*0}\gamma)$$

amb

$$\alpha = \frac{f_{\Lambda_b^0}}{f_{B^0}} \cdot \frac{1}{\mathcal{B}(B^0 \to K^{*0}\gamma)} \cdot \frac{\mathcal{B}(\Lambda \to p\pi^-)}{\mathcal{B}(K^{*0} \to K^+\pi^-)} \cdot \frac{\epsilon_{sel}(\Lambda_b^0 \to \Lambda\gamma)}{\epsilon_{sel}(B^0 \to K^{*0}\gamma)}$$
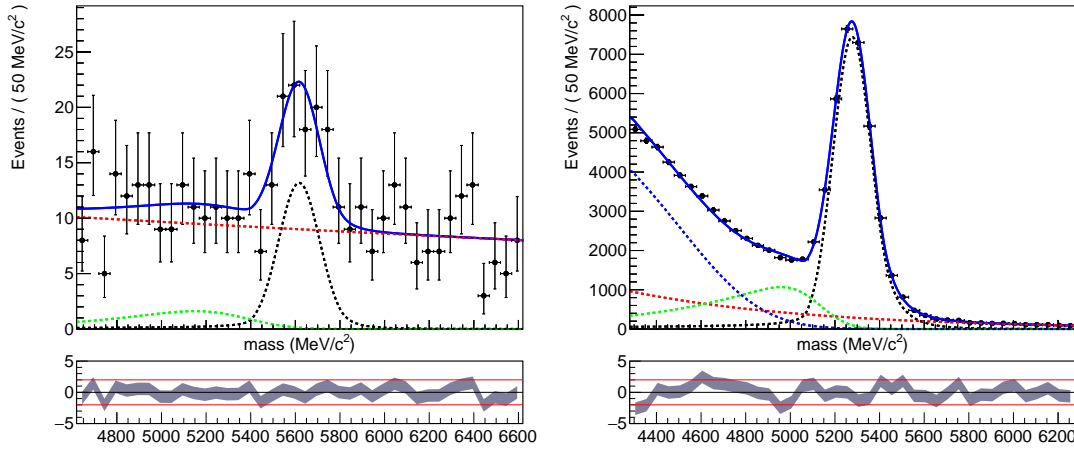
Figure 3: Resultats de l'ajust simultani a les distribucions de massa invariant $p\pi^-\gamma$ (esquerra) i $K^+\pi^-\gamma$ (dreta) dels candidats seleccionats. Les dades estan representades per punts negres i el resultat de l'ajust per una corva blava. La línia de punts negra descriu les contribucions de senyal, la vermella la dels fons combinatoris i la blava (blava i verda) la del $\Lambda_b^0 \to \Lambda\eta$ (dels $K^+\pi^-\pi^+$ i $K^+\pi^-\pi^0 X$) per candidats $p\pi^-\gamma$ ($K^+\pi^-\gamma$).

El valor d'aquest paràmetre s'obté a partir de l'evaluació dels diferents termes descrits anteriorment, $\alpha = 716 \pm 81 \pm 28$, i es fixa a l'hora de fer l'ajust.

Per a l'ajust, la contribució de les senyals es descriu mitjançant dues funcions Crystal Ball de doble cua, on els valors dels paràmetres de les cues es fixen als extrets del MC. La separació entre els pics es limita al valor mesurat per LHCb per a la diferència entre les masses de la Λ_b^0 i la B^0 a través d'una Gaussiana i la raó entre les amplades al valor obtingut de la simulació. El fons combinatori es descriu per mitjà d'una distribució exponencial amb el paràmetre de desintegració lliure i potencialment diferent per als dos modes. Les principals contribucions de fons d'origen físic que afecten el mode $B^0 \to K^{*0}\gamma$ s'extreuen d'anàlisis anteriors d'aquest canal. Concretament, les contaminacions provinents de desintegracions a l'estat final $K^+\pi^-\pi^+$ i $K^+\pi^-\pi^0 X$, on X pot ser qualsevol partícula, es modelen amb dues funcions Argus amb els paràmetres que en descriuen la forma fixats. Diferents fonts potencials de contaminació per al mode $\Lambda_b^0 \to \Lambda\gamma$ s'estudien utilitzant mostres de simulació i l'única contaminació significativa que es troba prové del mode $\Lambda_b^0 \to \Lambda\eta$. La forma d'aquesta contribució s'extreu del MC modelant-la també mitjanç una funció Argus amb els paràmetres de forma fixats. La seva amplitud es limita a través d'una Gaussiana al valor esperat, obtingut a partir de la seva fracció d'embrancament mesurada per LHCb i de les eficiències extretes del MC.

Els resultats de l'ajust, que es mostren a la Fig. 3, permeten veure una contribució clara de $\Lambda_b^0 \to \Lambda\gamma$ formada per (64 ± 13) esdeveniments i extreure una mesura de la fracció d'embrancament de $(2.59 \pm 0.52) \times 10^{-6}$. La significació estadística de la senyal s'avalua quantitativament per mitjà d'un escaneig de la versemblança de l'ajust, prenent la diferència entre el valor d'aquesta en el punt que representa la hipòtesi nul·la, que correpon a l'absència de senyal, i el millor punt, obtenint un resultat de 5.7σ.

Incerteses sistemàtiques

Diferents fonts d'incertesa sistemàtica que poden afectar les mesures són evaluades. Per una banda, la significació estadística de la senyal només està afectada per aquelles provinents de l'ajust de massa, que s'estimen en un 5.0%. Per altra, la determinació de la fracció d'embrancament també pot quedar afectada per incerteses provinents del càlcul del valor d'α. Aquestes estan dominades pel coneixement del quocient de les fraccions d'hadronització entre Λ_b^0 i B^0, que representa un 12.8%. La limitació en les mesures de les fraccions d'embrancament utilitzades en el càlcul contribueix amb un 3.5% i la incertesa sisetmàtica

deribada de l'obtenció de la fracció d'eficiències, dominada per diferències entre dades i MC, representa en total un 10.2%.

Resultats

La incertesa sistemàtica en la significació estadística de la senyal es considera una correcció al valor obtingut de l'ajust, doncs és molt menor a la incertesa estadística d'aquest. El valor corregit és de 5.5σ, fet que representa la primera observació del mode de desintegració $\Lambda_b^0 \to \Lambda\gamma$. Per a la fracció d'embrancament, s'obté un resultat final de $\mathcal{B}(\Lambda_b^0 \to \Lambda\gamma) = (2.59 \pm 0.52 \text{ (estad.)} \pm 0.28 \text{ (sist.)} \pm 0.33 \ (f_{\Lambda_b^0}/f_{B^0})) \times 10^{-6}$, que constitueix la primera mesura d'aquest observable.

Conclusions

Aquesta tesi representa una expansió del programa d'estudi de processos rars a l'experiment LHCb en les àrees de desintegracions radiatives d'hadrons b i de modes rars d'hadrons extranys. En primer lloc, s'ha desenvolupat una nova selecció de trigger que permet l'enregistrament de més esdeveniments de senyal tant per aquells modes ja estudiats com per altres de nous, permetent l'anàlisi de nous observables. A més a més, s'ha estudiat el canal $K_S^0 \to \pi^+\pi^- e^+ e^-$ amb la conclusió que la seva observació utilitzant les dades acumulades durant el Run 1 és possible i s'han aportat millores per aconseguir més senyal durant el Run 2. Finalment, s'ha fet una cerca del mode de desintegració $\Lambda_b^0 \to \Lambda\gamma$ que ha culminat amb la primera observació d'aquest procés i la primera mesura de la seva fracció d'embrancament, obrint les portes a futurs estudis de la polarització del fotó en aquest mode de desintegració.

Chapter 1

Introduction

The goal of this thesis is to test the current theoretical framework of particle physics, the Standard Model. This theory was developed throughout the second half of the 20th century and so far has been overwhelmingly successful in describing the results obtained by experiments and predicting with high accuracy previously unobserved phenomena. Some of its many achievements are the anticipation of the existence of the top quark and the tau neutrino and the precise forecast of various properties of weak neutral transitions and the W and Z bosons. The most outstanding and longstanding prediction of the Standard Model, the last missing piece of the puzzle, was confirmed by experiment on July 4th 2012: the existence of the Higgs boson.

With this accomplishment the theory was closed and completed. However, despite the great success in most of its predictions, there are phenomena that the Standard Model is not able to describe. To start with, this theory does not include the gravitational interaction, which is well understood in the context of General Relativity instead. Moreover it does not provide any viable dark matter candidate that fulfils the constraints from observational cosmology and does not explain the observed accelerated expansion of the Universe. It cannot account for the matter and anti-matter asymmetry of the Universe either. Finally, it predicts neutrinos to be massless although they have been observed to oscillate, an unambiguous evidence of their non-vanishing mass.

In order to account for all these shortcomings new theories are continuously developed, most built upon the Standard Model basis. But to date none has been able to explain all the data surpassing the accuracy of the current framework. Furthermore, it has not been possible to prove any of the SM prediction to be wrong, even though we know it is not the final theory. Consequently, the next milestone of the particle physics community is to find deviations in the behaviour of nature with respect to the predictions of the model. The current strategy consists on proving the particular features of the theory which provide enhanced sensitivity to the effects of potential extensions. The Standard Model phenomenology is briefly introduced in Chapter 2, where we further develop the concepts related to the cases studied in this work.

The results reported in this dissertation are based on data collected by the LHCb experiment, one of the four largest detectors at the European Organization for Nuclear Research (CERN). Its design, described in detail in Chapter 3, is optimised for the investigation of rare decays and charge-parity violation in beauty and charmed hadron decays. Moreover, as we will prove throughout this work, its characteristics allow it to perform state-of-the-art measurements in many other areas.

The physics cases explored in this thesis belong to the area of rare decays, term that encompasses all those processes that are strongly suppressed in the Standard Model framework, *i.e.* that are predicted to occur with a very low probability. This characteristic makes them extremely sensitive to additional contributions, which could be of a comparable size and cause perceptible deviations in several observables. Moreover, they exploit calorimeter objects, that is particles that are reconstructed in the electromagnetic calorimeter of the detector, to the design and construction of which the LHCb group at Universitat de Barcelona contributed significantly.

We want to stress that the physics analyses on which this work is based help to extend the reach of

the LHCb rare decays program to areas that had been accounted as impossible in the past or simply not considered. We believe this is a key point in the current context since these results provide complementary information to the originally foreseen measurements and can help to disentangle the origin of beyond the Standard Model physics. This has been possible thanks to the adaptability of the LHCb trigger, which allows to incorporate new selections in a flexible way.

We focus mainly on radiative decays of beauty hadrons, which are characterised by the presence of a high energetic photon in the final state. Due to this distinct topology dedicated selections are required to study these processes. Following this need, an inclusive selection has been developed and included in the trigger software. Based on multivariate techniques exploiting the common properties of these decays it allows to extend the LHCb radiative decays program, improving at the same time the efficiency on previously studied modes. The selection and its performance are reported in Chapter 4.

Radiative processes have been observed before at b-factories and LHCb and in most cases their branching ratios have been measured with precision. Therefore our interest lies on the polarisation of the emitted photon, which due to the peculiar structure of the electroweak interaction is predicted to be almost 100% polarised. Extensions of the Standard Model can a priori allow a different decay structure and thus change its value. The photon polarisation has been already explored in radiative beauty decays but the experimental precision is still limited. Moreover measuring this observable in various decay modes, would provide different ways to constrain the nature of beyond the Standard Model physics. Thus complementary measurements of this quantity are desirable.

The $\Lambda_b^0 \to \Lambda\gamma$ decay provides an interesting benchmark to study this property since its baryonic nature allows for a direct measurement. However this transition has never been observed at experiments. The Standard Model predicts a branching ratio of the same order of that of other radiative decays already studied in LHCb—between 10^{-5} and 10^{-6}— but the main challenge is its complicated experimental reconstruction, driven by its particular topology, which makes it more difficult to study than other radiative decays. The data collected during the years 2011 and 2012 was used to understand that the main bottleneck in the study of this decay was at the trigger level and therefore a dedicated selection was included starting from the 2015 data-taking period. In Chapter 6 we report a search for this decay based on the data recorded during 2016 thanks to the improved trigger.

As a complementary work we evaluate the possibility of studying rare decays of strange mesons at LHCb. These transitions are extremely suppressed in the Standard Model and provide enhanced sensitivity to new physics effects. Although they were not considered in the initial physics program and the detector is not optimised for this kind of physics, LHCb has proved to be very competitive in this area by improving by a factor 35 the upper limit on the decay probability of $K_S^0 \to \mu^+\mu^-$. It is thus worth it to expand this research field, specially for those cases that cannot be covered by other experiments in the near future.

We are interested in the decays of K_S^0 to four leptons since any deviation from the theoretical estimate of their branching fraction would be a clear sign of physics beyond the Standard Model. In order to understand the particular signature of these decays, the well-known $K_S^0 \to \pi^+\pi^- e^+ e^-$ mode is studied and the feasibility of observing this process at LHCb is assessed in Chapter 5.

Finally the conclusions of this work and their implications, together with future prospects and possible improvements of the measurements, are discussed in Chapter 7.

Chapter 2

Theoretical framework

This chapter presents the theoretical framework motivating the studies performed in this thesis. It is meant to be an introduction to the current understanding of particle physics with special focus on flavour. Exhaustive lectures on the topic can be found in Refs. [1, 2]. A description of the physics cases relevant for the thesis is given in the last sections while more detailed reviews are available in Refs. [3, 4].

2.1   The Standard Model of Particle Physics

The Standard Model (SM) of Particle Physics describes the elementary particles that build the universe and three fundamental interactions between them: the electromagnetic, nuclear strong and nuclear weak forces. The gravitational interaction is not included in the SM since it has not been possible to describe it as a quantum field theory, the formalism employed in the construction of the SM. This framework provides tools to predict the properties of particles and interactions and has been so far the most successful theory describing the phenomena observed at high energy experiments.

According to the SM, the building blocks of matter are fermions, which are characterised by a half-integer spin. Depending on whether they interact through the strong force or not, fermions are classified as quarks or leptons — both subject to the weak and electromagnetic interactions. Both classes are composed of three generations or flavours, with particles in one generation having a larger mass than those in the previous one. A pair of fermions of each type forms a generation. Thus there are six quarks (up, down, charm, strange, top and bottom) and six leptons (electron, electron neutrino, muon, muon neutrino, tau and tau neutrino). They are commonly grouped into up-type and down-type quarks with electrical charge $2/3$ and $-1/3$, respectively, and electron-type and neutrino-type leptons with electrical charge -1 and zero (electrically neutral), respectively. as summarised in Table 2.1. Each fermion has a corresponding antiparticle —a copy with the same mass but opposite quantum numbers.

Interactions are explained in the SM by the exchange of force carriers called gauge bosons, which have an integer spin. Each interaction has its own mediators: the photon (γ), gluon (g), and Z and $W^{\pm}$ bosons are the carriers of the electromagnetic, strong and weak interactions, respectively, as reported in Table 2.2. Each force is characterised by its particular properties: the strong interaction acts on particles

Table 2.1: Quarks and leptons in the SM classified by electrical charge and generation.

	1st generation	2nd generation	3rd generation	Electrical Charge
Quarks	Up	Charm	Top	$2/3$
	Down	Strange	Bottom	$-1/3$
Leptons	Electron	Muon	Tau	-1
	Electron neutrino	Muon neutrino	Tau neutrino	0

Table 2.2: SM Gauge bosons and associated interaction.

Interaction	Gauge boson
Strong	Gluon (g)
Electromagnetic	Photon (γ)
Weak	$W^{\pm}$
	Z

that have colour charge, *i.e.* quarks, and is the responsible for binding them together into hadrons such as protons and neutrons; the electromagnetic force applies to particles with electrical charge and the weak interaction acts on flavour, *i.e.* quarks and leptons. The electromagnetic and weak forces are unified at high energies, giving place to the electroweak interaction.

The formalism employed in the SM is Quantum Field Theory, where particles correspond to excitations of the fundamental underlying quantum fields and the forces of nature are described by interaction terms among the relevant fields. The dynamics of both the quantum state and the fields are governed by the Lagrangian density, or simply Lagrangian, which is given in Ref. [5].

Moreover, the SM is a local gauge theory, *i.e.* there are local transformations of the underlying fields that leave the physical observables of the system unchanged. In particular, the gauge symmetry of the SM is described by the group product

$$SU(3)_C \times SU(2)_L \times U(1)_Y \tag{2.1}$$

where $SU(3)_C$ applies to the strong interaction described by Quantum Chromodynamics (QCD) and $SU(2)_L \times U(1)_Y$ to the electroweak one. It should be noted that $SU(2)_L$ acts only on left-handed fermions, generating maximal parity violation [6]. Consequently simple mass terms of the type $m\bar{\psi}\psi = m(\bar{\psi}_L \psi_R + \bar{\psi}_R \psi_L)$, where ψ ($\bar{\psi}$) is the fermion (anti-fermion) field and R (L) the right- (left-)handed projector, are not invariant under the electroweak symmetry and are thus not present in the SM Lagrangian. Furthermore electroweak boson mass terms of the same type would break gauge symmetry, so are also forbidden. However non-vanishing fermion and weak boson masses have been measured and thus a term accounting for them is needed. The solution to both problems is solved by introducing a new scalar field that does not vanish in the vacuum, *i.e.* whose potential minimum is not at zero [7, 8, 9]. This scalar mixes with the electroweak bosons generating mass terms for $W^{\pm}$ and Z. Interaction terms with fermions can also be added to the model providing fermion mass. This mechanism is known as spontaneous symmetry breaking and the realisation of the scalar field is commonly referred to as the Higgs boson.

After the experimental confirmation of the existence of a scalar particle compatible with the properties of the Higgs boson [10, 11] the observation of particles predicted by the SM was completed. Remarkably, this model has provided the most precise predictions in physics with extreme success [12, 13, 14, 15]. However there are observed phenomena that can not be accommodated within the SM framework. Examples of this are the measured non-vanishing mass of neutrinos, the existence of dark matter and dark energy as needed to explain cosmological observations and the dominance of matter over anti-matter in the universe. Consequently several extensions of the model have been proposed. No sign of beyond the SM (BSM) effects has been observed to date but it is of utmost importance to keep testing the SM predictions in order to discover where BSM effects arise.

2.2 Flavour Physics and Charge-Parity violation

As explained above, fermions acquire mass after spontaneous symmetry breaking. In the particular case of quarks, the mass and electroweak interaction eigenstates are rotated. Thus mixing among the different mass eigenstates, referred to as flavours, arises through this interaction leading to quark flavour changes. The strength of the mixing is described by a unitary 3×3 matrix, known as the Cabibbo-Kobayashi-

Maskawa (CKM) matrix [16, 17]:

$$V_{CKM} = \begin{pmatrix} V_{ud} & V_{us} & V_{ub} \\ V_{cd} & V_{cs} & V_{cb} \\ V_{td} & V_{ts} & V_{tb} \end{pmatrix} = \begin{pmatrix} 1 - \frac{\lambda^2}{2} & \lambda & A\lambda^3(\rho - i\eta) \\ -\lambda & 1 - \frac{\lambda^2}{2} & A\lambda^2 \\ A\lambda^3(1 - \rho - i\eta) & A\lambda^2 & 1 \end{pmatrix} \tag{2.2}$$

where V_{ij} gives the mixing strength between quark i and j. The CKM unitary matrix can be parametrized by 4 independent parameters, 3 rotation angles and a complex phase, which are not given by the theory but should be measured experimentally. The Wolfenstein parametrization [18] is given in the right-hand-side term of Eq. 2.2 to show explicitly the hierarchy that the CKM matrix exhibits, with $\lambda = |V_{us}| \approx 0.22$ and A, ρ and η free parameters of order 1.

The unitarity of the CKM matrix imposes strong constraints on its elements. The diagonal terms should satisfy:

$$\sum_j |V_{ij}|^2 = \sum_i |V_{ij}|^2 = 1 \tag{2.3}$$

where i and j run over the up- and down-type quarks, respectively. This relation is known as weak universality and is a consequence of the fact that all the $SU(2)_L$ fermions couple with the same strength to the electroweak vector bosons. For the remaining elements, the unitarity condition implies:

$$\sum_j V_{ij}V_{kj}^* = 0 \tag{2.4}$$

for any different i and k, where k also runs over the up-type quarks. These relations are sums of three complex numbers that can be represented as triangles in the complex plane. The vanishing condition implies the figures should be closed. There are in total 6 different triangles which provide a strong test of the SM through the measurement of their sides and angles.

Moreover, the complex phase in the CKM matrix gives rise to Charge-Parity (CP) violation. This is the unique source of such asymmetry in the SM and thus the measurement of its magnitude is of great interest. Current experimental results show good consistency within the SM [19]. However the matter-antimatter asymmetry observed in the Universe cannot be explained to origin from this single source of CP violation, requiring the addition of BSM physics. More precision on experimental measurements is desirable as well as searches for CP violation in processes where the SM predicts small or negligible effects, as this would be a clear sign of New Physics (NP). Testing of the unitary triangles and searches for CP violating effects are two of the main goals of the LHCb experiment [20].

2.3 Rare decays of heavy hadrons

A particular feature of the SM reflected in the CKM matrix is that flavour changing processes are only mediated by the $W^\pm$ boson and thus they also carry a change of electrical charge. This means that flavour-changing neutral-currents (FCNC) are not allowed at first order (tree-level) in the SM. This kind of processes always occur through an intermediate additional change of flavour leading to loop mediated transitions, as generically shown in Figure 2.1. As discovered by Glashow, Iliopoulos and Maiani [21] the different loop contributions have a negative interference proportional to the difference of the squared masses of the virtual particles in each diagram relative to the squared $W^\pm$ mass. This effect is known as GIM mechanism and implies that contributions of light quarks to loop diagrams are suppressed. The combination of the GIM mechanism with the hierarchy of the CKM matrix leads to a very large suppression of beauty and strange FCNC decays in the SM, making them extremely sensitive to NP contributions. For instance new particles predicted in BSM theories could give rise to new loop contributions comparable to the suppressed SM ones, changing the observable properties of the decays. Consequently both the theoretical and experimental study of these transitions is of uttermost interest and is also a cornerstone of the LHCb physics program. This thesis is focused in particular on the study of rare strange and radiative beauty decays, discussed in the following sections.
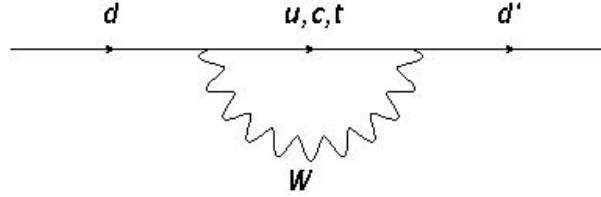
Figure 2.1: Example of a FCNC loop level diagram of a d-type quark (d) decaying into another d-type quark (d') within the SM.

From the theoretical point of view, two different effects are involved in the computation of FCNC decays, one governing the quark level transition mediated by the electroweak interaction, and the other related to the hadronisation process of the quarks due to the strong force. The mixture of these two effects makes it difficult to perform calculations of physical observables starting from the full SM Lagrangian. In order to simplify the problem low energy effective theories are built by integrating out the heavy fields in the model. Following the Operator Product Expansion (OPE) [22] an effective Hamiltonian is constructed from a set of local operators $\mathcal{O}_i$. For a given $i \to f$ decay:

$$\langle f|H_{eff}|i\rangle \propto \sum_i \mathcal{C}_i \langle f|\mathcal{O}_i|i\rangle \tag{2.5}$$

where $\mathcal{C}_i$ are the Wilson coefficients that account for short-distance (SD) effects, $\mathcal{O}_i$ are a complete set of local operators describing the full theory and the hadronic matrix elements include all the non-perturbative QCD effects. This method is further exploited in Section 2.3.2 for the particular case of $b \to s\gamma$ transitions.

2.3.1 Rare strange decays

Rare decays of strange hadrons are mediated by the FCNC $s \to d$ transition, which is suppressed in the SM both by the GIM mechanism and by the smallness of $|V_{ts}V_{td}| \sim \lambda^5 \sim 10^{-4}$. These decays are as a consequence extremely sensitive to BSM effects.

Due to the presence of very different mass scales (m_W, m_K, m_π), QCD corrections are amplified by large logarithms in these processes. In order to treat both effects separately, the heavy degrees of freedom can be integrated out leading to an effective three-flavour theory. Using the OPE, the dynamics of the theory can be described by [23]:

$$H_{eff} = -\frac{G_F}{\sqrt{2}} V_{ud} V_{us}^* \sum \mathcal{C}_i(\mu)\mathcal{O}_i(\mu) \tag{2.6}$$

where $\mathcal{O}_i$ are a set of local operators constructed with the light degrees of freedom, $\mathcal{C}_i$ are the Wilson coefficients, which are known to next-to-leading-order [24] and contain the QCD effects, and the relevant mass scale is $\mu = m_K$.

In order to calculate full amplitudes, the matrix elements between the initial and final states, which involve non-perturbative dynamics, are also needed. Several techniques are available and a usual choice is Chiral Perturbation Theory, which provides an expansion of the decay amplitudes in momenta and masses. It is characterised by the accumulation of all the hadronic uncertainties into low energy constants, which can be extracted from experimental results, if precise calculations are available, or from the lattice, though the latter has still some limitations [3]. In order to disentangle possible NP effects, it is necessary to have under control the long distance (LD) terms.

An interesting case is that of $K_S^0 \to \ell^+\ell^-\ell^+\ell^-$, and the related $K_L^0 \to \ell^+\ell^-\ell^+\ell^-$, both dominated by LD effects in the SM. As proven in [25] these effects can be estimated using experimental results from
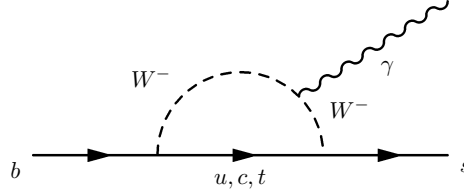
Figure 2.2: $b \to s\gamma$ penguin loop diagram within the SM.

the related $K_S^0 \to \gamma\gamma$ and $K_L^0 \to \gamma\gamma$ modes. Thus a measurement of the decay rate exceeding the SM prediction would be a clear signature of BSM effects. Moreover, the interference between the K_S^0 and K_L^0 modes can give information on the sign of $\mathcal{A}(K_L^0 \to \gamma\gamma)$, which is a necessary input for the calculation of the LD contribution to $K_L^0 \to \mu^+\mu^-$. The short distance component in this mode provides a stringent constraint of CKM elements and thus the full understanding of the LD one would allow a clean probe of the SM.

While the K_L^0 decays have been measured by KTeV and NA48 [26, 27, 28], no experimental study of the K_S^0 modes exists. The LHCb experiment was not designed to explore strange decays and these were not among the initial physics program of the collaboration [20]. However the copious production of s quarks at the LHC energies and the flexibility of the LHCb trigger —see the following chapter for a detailed description— allows the study of these modes with high precision, as proven by the largely improved limit on the branching fraction of the $K_S^0 \to \mu^+\mu^-$ decay [29] and the observed evidence for the $\Sigma \to p\mu^+\mu^-$ decay [30]. As a first step towards the search for $K_S^0 \to \ell^+\ell^-\ell^+\ell^-$ decays at LHCb the feasibility of observing the related and well-known $K_S^0 \to \pi^+\pi^- e^+e^-$ is addressed in Chapter 5.

2.3.2 Radiative beauty decays

Radiative b-decays are also FCNC, mediated by the $b \to q\gamma$ quark level transition, with $q = s, d$, as shown in Fig. 2.2. As such they are suppressed by $|V_{tb}V_{ts}|$ and $|V_{tb}V_{td}|$, respectively, and are thus very sensitive to NP effects. In this thesis we focus on the experimentally more accessible $b \to s\gamma$ process.

The effective Hamiltonian relevant for $b \to s\gamma$ decays can be obtained using the OPE introduced in Sec. 2.2. At leading order (LO) it reads [31]:

$$\mathcal{H}_{eff} = -\frac{G_F}{\sqrt{2}} V_{ts}^* V_{tb} \left[\mathcal{C}_7 \mathcal{O}_7 + \mathcal{C}_7^{'} \mathcal{O}_7^{'} \right] \tag{2.7}$$

where G_F is the Fermi constant and V_{ts}^* and V_{tb} the relevant CKM elements. The electromagnetic dipole operators $\mathcal{O}_7$ and $\mathcal{O}_7^{'}$ are defined as:

$$\mathcal{O}_7 = \frac{e}{8\pi^2} m_b \bar{s} \sigma_{\mu\nu} R b F^{\mu\nu} \tag{2.8}$$

$$\mathcal{O}_7^{'} = \frac{e}{8\pi^2} m_b \bar{s} \sigma_{\mu\nu} L b F^{\mu\nu} \tag{2.9}$$

with $R \equiv 1 + \gamma_5$ and $L \equiv 1 - \gamma_5$ proportional to the right- and left-handed projectors. The Wilson coefficients $\mathcal{C}_i$ account for the strength of each contribution. In the SM only left-handed quarks are subject to the electroweak interaction. Since chirality flips can only occur due to the non-vanishing mass of the quarks, the $\mathcal{O}_7^{'}$ contribution is suppressed by a factor $|r| = \mathcal{C}_{7SM}^{'}/\mathcal{C}_{7SM} = m_s/m_b$. Many extensions of the SM contain new contributions to $\mathcal{C}_7^{'}$ comparable to $\mathcal{C}_{7SM}$ which would lead to observable effects. Some examples of these theories are Left-Right symmetric models, supersymmetric models beyond minimal flavour violation and models containing vector-like quarks [32].

Branching fractions of exclusive $b \to s\gamma$ modes have been measured with precision at the b-factories [33, 34, 35] and also at LHCb [36]. It should be noted though that a measurement of the branching fraction

of any $b \to s\gamma$ transition can only provide a circular constraint in the $\mathcal{C}_7$-$\mathcal{C}_7'$ plane, since it is proportional to $|\mathcal{C}_7|^2 + |\mathcal{C}_7'|^2$ —see Eq. 2.11 for a particular example. In order to disentangle the true value of the two coefficients separately, complementary observables with different dependence on the Wilson coefficients are needed. One of such observables is the photon polarisation.

Photons emitted in a $b \to s\gamma$ transition are predicted to be left-handed in the SM since the quarks that couple to the W^- are left-chiral due to the V-A nature of the electroweak force. The photon polarisation is defined as the normalised asymmetry between the number of left-handed and right-handed polarised photons in a $b \to s\gamma$ decay:

$$\alpha_\gamma = \frac{P(\gamma_L) - P(\gamma_R)}{P(\gamma_L) + P(\gamma_R)} = \frac{1 - |r|^2}{1 + |r|^2} \tag{2.10}$$

with $|r| = C_7'/C_7$ at leading order (LO). In the SM $|r| \sim m_s/m_b$ and thus $\alpha_\gamma \sim 1$.

Different methods to access this observable in $b \to s\gamma$ decays have been proposed [32, 37, 38, 39]. LHCb reported the first observation of the photon polarisation in $B^+ \to K^+\pi^+\pi^-\gamma$ decays [40] and has measured for the first time observables sensitive to this parameter in the $B^0 \to K^{*0}e^+e^-$ [41] and $B_s^0 \to \phi\gamma$ [42] modes. The experimental sensitivity is still far from the precise value predicted by the SM and thus further measurements are desired.

Baryonic b-radiative decays, largely unexplored to date, can provide complementary constrains since the information on the chirality of the electroweak transition is retained in the baryon of the decay. A search for the yet unobserved $\Lambda_b^0 \to \Lambda\gamma$ decay is reported in Chapter 6 and we shall describe the phenomenology related to this mode in the following.

The case of $\Lambda_b^0 \to \Lambda\gamma$

The most stringent limit on the branching ratio ($\mathcal{B}$) of the unobserved $\Lambda_b^0 \to \Lambda\gamma$ decay was set by CDF at $\mathcal{B}(\Lambda_b^0 \to \Lambda\gamma) < 1.3 \times 10^{-3}$ at 95% confidence level [43]. No other experiment has reported any study of this mode. Thanks to the large production of Λ_b^0 at pp collisions, LHCb has the unique opportunity to explore this process.

In the SM the branching ratio of the $\Lambda_b^0 \to \Lambda\gamma$ decay can be derived [44] from the effective Hamiltonian presented in Eq. 2.14:

$$\mathcal{B}(\Lambda_b^0 \to \Lambda\gamma) \propto \tau(\Lambda_b^0)|V_{tb}V_{ts}^*|^2|F(0)|^2 \left(|\mathcal{C}_7|^2 + |\mathcal{C}_7'|^2\right) \tag{2.11}$$

where $\tau(\Lambda_b^0)$ is the Λ_b^0 lifetime, V_{ts}^* and V_{tb} are the relevant CKM elements and $F(0)$ is the $\Lambda_b^0 \to \Lambda$ form factor at $q^2 = 0$. A wide range of predictions for the value of $\mathcal{B}(\Lambda_b^0 \to \Lambda\gamma)$ in the SM is found in the literature, $\mathcal{B}(\Lambda_b^0 \to \Lambda\gamma) = (0.06 - 1) \times 10^{-5}$ [45, 46, 47, 48]. The discrepancies arise mainly from the different values used for $F(0)$.

On one hand, the $\Lambda_b^0 \to \Lambda$ form factor can be extracted from other measured $\Lambda_b^0 \to \Lambda$ processes such as semileptonic decays, but needs to be extrapolated to $q^2 = 0$ to obtain its value at the photon pole. Also lattice calculations, giving the most precise form factor predictions nowadays, compute values near $q^2 = q_{max}^2$ and are affected by theoretical uncertainties in the extrapolation to the full range. On the other hand, methods exist for the calculation of form factors in the low q^2 regions, such as Light Cone Sum Rules. Different interpolating currents have been used in this case in order to extract the form factors from the relevant matrix elements. A measurement of the $\mathcal{B}(\Lambda_b^0 \to \Lambda\gamma)$ would allow to discriminate between the different approaches.

It should be noted that LD contributions are expected to be small in general in $b \to s\gamma$ transitions [49] and in particular in the $\Lambda_b^0 \to \Lambda\gamma$ decay [44], providing a clean test of the electroweak predictions.

On top of the constraints that can be extracted from the branching ratio measurement, the $\Lambda_b^0 \to \Lambda\gamma$ decay gives access to the study of the photon polarisation defined in Eq. 2.10 through the angular
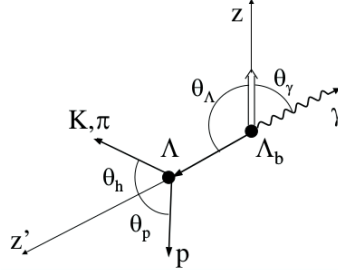
Figure 2.3: Angle definition for the decay $\Lambda_b^0 \to \Lambda\gamma$ from Ref. [50]. The angles θ_Λ and θ_γ are measured in the Λ_b^0 rest frame, while the angles θ_h and θ_p are measured in the Λ rest frame.

distribution of the final state particles [50]:

$$\frac{d\Gamma}{d\cos\theta_\gamma} \propto 1 - \alpha_\gamma P_{\Lambda_b^0} \cos\theta_\gamma \tag{2.12}$$

$$\frac{d\Gamma}{d\cos\theta_p} \propto 1 - \alpha_\gamma \alpha_{p,1/2} \cos\theta_p \tag{2.13}$$

where θ_γ is the angle between the photon momentum and the Λ_b^0 spin direction (Z) in the Λ_b^0 rest frame and θ_p is the angle between the proton and the Λ momenta in the rest frame of the Λ, as shown in Fig. 2.3. $P_{\Lambda_b^0}$ is the initial Λ_b^0 polarisation and $\alpha_{p,1/2} = 0.642 \pm 0.013$ [51] is the weak $\Lambda \to p\pi^-$ decay parameter.

Although the Λ_b^0 polarisation was first expected to be sizeable at the LHC, it has been measured by LHCb to be small, $P_{\Lambda_b^0} = 0.06 \pm 0.07 \pm 0.02$l [52]. The sensitivity of the photon distribution to the photon polarisation is thus suppressed by this factor. Still it can be extracted from the angular proton distribution and Eq. 2.12 can actually be used to obtain an independent measurement of the Λ_b^0 production polarisation.

It should be noted that the photon polarisation is form-factor independent so it is insensitive to the uncertainties affecting the branching fraction of the $\Lambda_b^0 \to \Lambda\gamma$ decay. LD effects from $c\bar{c}$ states can lead to helicity changing contributions but small corrections are expected as discussed above. Thus little hadronic uncertainties affect the SM prediction at LO, providing a very clean observable.

At next-to-leading-order (NLO), gluon loops contribute to the $b \to s\gamma$ transition and the effective Hamiltonian becomes [31]:

$$\mathcal{H}_{eff} = -\frac{G_F}{\sqrt{2}} V_{ts}^* V_{tb} \left[D\mathcal{O}_7 + D'\mathcal{O}_7' \right] \tag{2.14}$$

where the operators are now a linear combination of Wilson coefficients:

$$D = \mathcal{C}_7^{(0)} + \frac{\alpha_s}{4\pi} \left(\mathcal{C}_7^{(1)} + \mathcal{C}_2^{(0)} k_2 + \mathcal{C}_8^{(0)} k_8 \right) \tag{2.15}$$

$$D' = \mathcal{C}_7'^{(0)} + \frac{\alpha_s}{4\pi} \left(m_b \mathcal{C}_7'^{(1)} + \mathcal{C}_8'^{(0)} k_8 \right) \tag{2.16}$$

where the coefficients k_i account for the $\mathcal{O}(\alpha_s)$ elements of the operators $\mathcal{O}_i$ and include CP conserving strong phases. The current-current and chromomagnetic dipole operators are defined as:

$$\mathcal{O}_2 = (\bar{c}\gamma_\mu Lb)(\bar{s}\gamma^\mu Lc) \tag{2.17}$$

$$\mathcal{O}_8 = \frac{g}{8\pi^2} m_b \bar{s}\sigma_{\mu\nu} RT_a b G_a^{\mu\nu} \tag{2.18}$$

respectively and the flipped-chirality $\mathcal{O}_2'$ contribution has been neglected.

At this level CPV can arise from interference between weak and strong phases generating for example an asymmetry in the decay rates:

$$A_{CP} = \frac{\Gamma - \bar{\Gamma}}{\Gamma + \bar{\Gamma}} \tag{2.19}$$

where Γ and $\bar{\Gamma}$ are the decay rate of the $\Lambda_b^0 \to \Lambda\gamma$ and the CP conjugate mode, respectively. In the SM, CPV in $b \to s\gamma$ transitions is CKM suppressed and estimated to be $A_{CP} \leq \mathcal{O}(1\%)$ but it can be as large as $\mathcal{O}(10\%)$ in BSM. The strongest constrain on NP contributions to CPV effects in $b \to s\gamma$ is given by the measurement of $A_{CP}(B^0 \to K^{*0}\gamma)$ [36].

Higher order corrections affect also the angular asymmetries and CPV effects should be considered, *i.e.* at NLO $\alpha_\gamma \neq \bar{\alpha}_\gamma$ where α_γ is the photon polarisation in $\Lambda_b^0 \to \Lambda\gamma$ and $\bar{\alpha}_\gamma$ in the conjugate mode. These two parameters are related now to the ratio of the NLO operators defined as $r^{eff} = D'/D$ and $\bar{r}^{eff} = \bar{D}'/\bar{D}$ in an analogous manner to Eq. 2.10. It is shown in Ref. [31] that also the CP-averaged observable is sensitive to NLO effects. The corrections induced by $\mathcal{O}_2$ are estimated to be of $5 - 20\%$ while for $\mathcal{O}_8$ are of 1% if $\mathcal{C}_8 \sim \mathcal{C}_7$ and $\mathcal{C}_8' \sim \mathcal{C}_7'$, as in the SM. If the $\mathcal{C}_8$ operators are enhanced in BSM, corrections can be of order 10%. More precise computations of these NLO SM effects are needed to unambiguously test BSM physics in the measurement of the photon polarisation in $\Lambda_b^0 \to \Lambda\gamma$.

The first milestone towards the experimental determination of the photon polarisation in $\Lambda_b^0 \to \Lambda\gamma$ is the observation of this yet unobserved decay. A search for this mode at LHCb is reported in Chapter 6.

Chapter 3

The LHCb detector at the LHC

3.1   The LHC at CERN

The Large Hadron Collider (LHC) [53] is the largest and most powerful particle accelerator to date. It is located in the facilities of the European Organization for Nuclear Research (CERN), under the Franco-Swiss border close to Geneva. It consists of a 27 km ring at an average depth of 100 m.

Inside the accelerator, two particle beams travel in opposite directions in separate pipes. Superconducting magnets and radiofrequency cavities are used to guide and boost the particles at close to the speed of light until they are deflected to make them collide. Seven physics experiments are located around the four interaction points to study the collisions provided by the accelerator.

The main program of the LHC is based on proton-proton (pp) collisions. However other particles such as heavy ions are collided in dedicated runs. The data samples used throughout this thesis are based on pp collisions at different centre of mass energies.

After the full commissioning of the accelerator and the experiments, the first collisions meant for physics analyses occurred in 2010 at a centre of mass energy ($\sqrt{s}$) of 7 TeV. This energy remained the same in 2011 and in 2012 it was increased to 8 TeV. This concluded the data-taking period known as Run 1. After this, the accelerator was in shutdown mode for two years arranging for an increase in energy. The Run 2 data-taking started in 2015 with pp collisions at a centre of mass energy of 13 TeV and will last until the end of 2018.

3.2   The LHCb detector

The Large Hadron Collider beauty (LHCb) experiment [54, 55, 56] is one of the four main experiments at the LHC. It was designed to study CP violation and rare decays of beauty and charm hadrons but its physics program has been importantly expanded, surpassing by far the original goals of the collaboration. New areas of research include heavy ion collisions, exotica searches and strange physics, among others. The integrated luminosity recorded by the detector in pp collisions during the different data-taking periods described above is summarised in Fig. 3.1 (left).

At the LHC energies $b\bar{b}$ pairs are produced very boosted into the forward and backward directions as shown in Fig. 3.1 (right). To exploit this characteristic, LHCb was built as a single-arm spectrometer with a forward angular coverage from 15 to 300 mrad in the horizontal bending plane and from 15 to 250 mrad in the vertical non-bending one. A lateral layout of the detector is shown in Fig. 3.2.

The sub-detectors that comprise the experiment can be grouped into two main systems: the tracking system and the particle identification system. On top of these, the trigger system takes the input of few sub-detectors to decide in real time which events to store and the offline system is in charge of the data processing and storage.
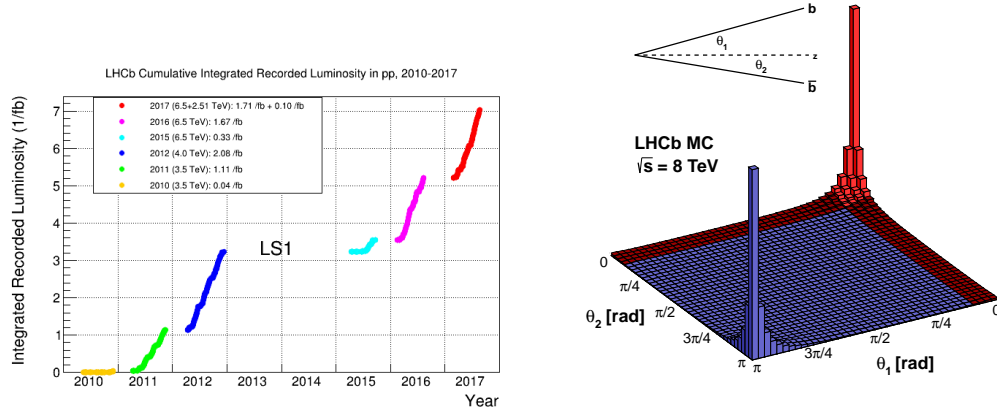
Figure 3.1: Cumulative integrated luminosity recorded by LHCb in pp collisions in the period 2010–2017 (left) and angular distribution of $b\bar{b}$ production in pp interactions at a centre of mass energy of 8 TeV (right).

3.2.1 Tracking sub-detectors

The tracking system is meant to detect and reconstruct tracks from charged particles, measure their momentum and determine the position of the collision point or primary vertex (PV) and the subsequent decay vertex or secondary vertex (SV). It includes several sub-detectors situated along the full geometry.

The **Vertex Locator** (VELO) [57] is the most upstream detector and its main purpose is the identification and separation of the PV and SV. It is composed by a series of silicon-strip discs placed along the beam pipe surrounding the interaction region, which provide a measure of the r and ϕ coordinates. The discs are divided in halves and a unique system allows to close them around and retract back from the beam line. This feature permits the VELO to stay at a distance of about 8 mm from the particle beam during physics collisions, making it the LHC detector acting closest to the beam pipe, while keeping it safe from dangerous radiation during instable running of the LHC.

The **Tracking Turicensis** (TT) [55] station is located right upstream the magnet providing track measurements before the particle trajectory bends. It is a planar station perpendicular to the beam line that covers the full detector acceptance. It is formed by four layers, made of silicon micro-strips, arranged in a stereo configuration, with the two inner layers rotated by -5 and $5°$ in the $x-y$ plane. The same arrangement is used by all the tracking stations to provide 3D track reconstruction.

The **dipole magnet** [58] provides a vertical field that causes charged particles to bend along the horizontal plane, allowing a measurement of their momentum. The integrated magnetic field applied to tracks originating from close to the interaction region is around 4 Tm. The magnet polarity can be reversed in order to minimise as much as possible systematic effects from detector asymmetries. About half of the data is recorded with the magnet polarity up and the other half with the magnet polarity down.

The **T-stations** (T1, T2, T3) are placed downstream the magnet and are divided into two regions: the **Inner Tracker** (IT) [59], which covers the innermost part of the stations, and the **Outer Tracker** (OT) [60], which expands into the surrounding area covering the full detector acceptance. The IT uses the same technology as the TT and is formed by four detector boxes in each station, arranged around the beam pipe in a cross-shaped form. The OT is formed by drift tubes filled with Argon and CO_2 to guarantee a drift time below 50 ns.

In the track reconstruction software the hits in the VELO, the TT, the IT and the OT detectors are combined to form particle trajectories. The reconstruction algorithms aim to find all tracks in the event
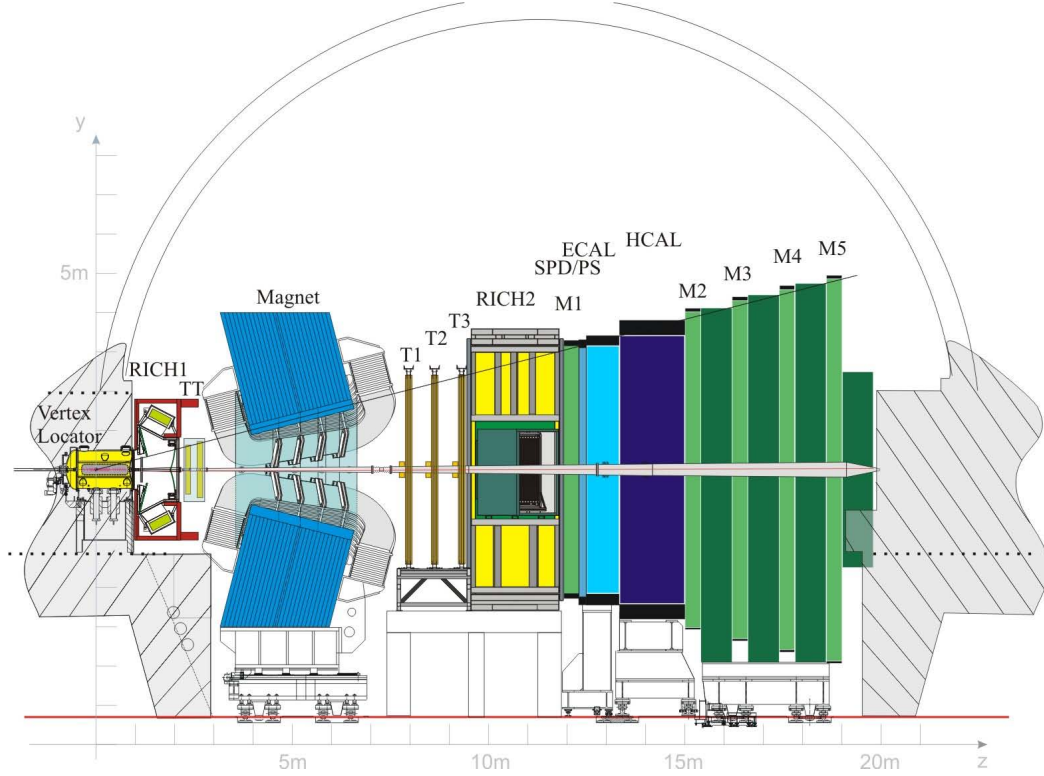
Figure 3.2: Lateral view of the LHCb detector. Collisions take place inside the Vertex Locator (on the left side of the picture) and the different detectors instrument the forward region.

which leave sufficient detector hits. Depending on their trajectories inside the spectrometer the following classes of tracks, illustrated in Figure 3.3 are defined:

- **Long tracks** traverse all the tracking sub-detectors. They have the most precise momentum resolution and are therefore the most used in physics analysis.

- **Downstream tracks** traverse only the TT and T stations, resulting in a loss in momentum resolution. Their main use cases are K_S^0 and Λ that decay outside the VELO.

- **Upstream tracks** traverse only the VELO and the TT. They are mainly low momentum particles that are bent out of the detector acceptance by the magnetic field. Their momentum resolution is poor and they are therefore not used for physics analysis but are useful for background studies in RICH1.

- **Velo tracks** are detected only in the VELO. They are large angle or backward particles used for the PV reconstruction.

- **T-tracks** are detected only in the T-stations. They typically originate in secondary interactions and are used for the RICH2 pattern recognition.

The excellent performance of the tracking system provides high precision particle momentum and vertex position resolutions. For long tracks the momentum resolution varies from 0.5% at low momentum to 1.0% at $200\,\mathrm{MeV}$. The resolution on the impact parameter (IP) of a track with respect to the PV scales inversely with its transverse momentum as $(15 + 29/p_\mathrm{T}\,[\,\mathrm{GeV}\,])\,\mathrm{\mu m}$ [56].
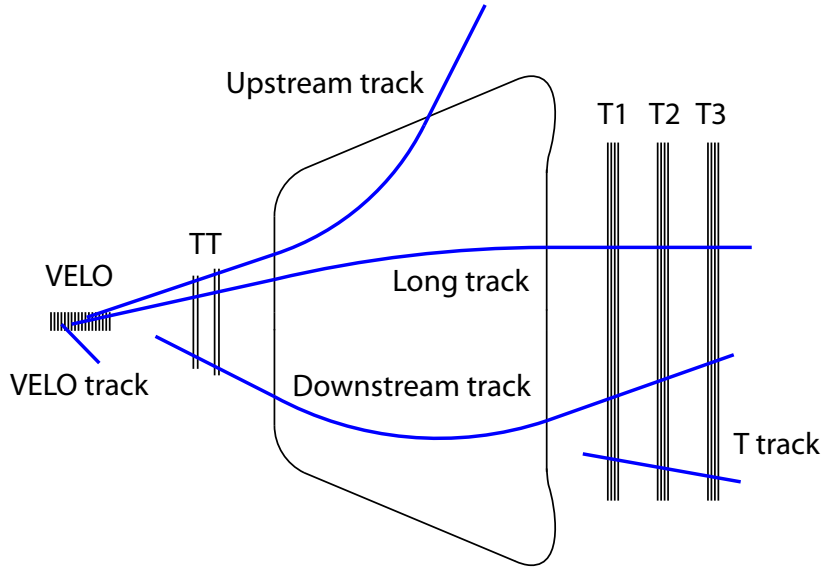
Figure 3.3: Sketch of the different track types defined at LHCb.

3.2.2 Particle Identification sub-detectors

The core physics program of the LHCb experiment involves the study of the decays of heavy flavour particles into exclusive final states. This requires precise identification and separation of the different particle species that result from these decays. This is achieved through the particle identification system, composed by the RICH detectors, the calorimeters and the muon stations.

The **Ring Imaging Cherenkov** (RICH) detectors [61] exploit the Cherenkov effect [62] to identify different particle species. Fast particles traversing a material at a higher velocity than the speed of light in that media emit light in a cone whose aperture is proportional to the speed of the particle. Combining this measurement with information from the tracking system and taking into account the magnetic field, the mass and charge of the particle are inferred achieving a complete identification. For a given mass the cone angle depends on the momentum of the particle, as shown in Figure 3.4. A likelihood probability is then built for each particle to belong to a certain species. Two RICH detectors are installed at LHCb. **RICH1** is situated upstream of the magnet, right after the VELO, and provides identification for low momentum particles $(1-60\,\text{GeV})$ using aerogel (in Run 1 only) and C_4F_{10} as radiators. **RICH2** is placed downstream the magnet, after the T-stations, and provides identification for high momentum particles $(15-100\,\text{GeV})$ using CF_4. Both detectors use a combination of spherical and flat mirrors to reflect the Cherenkov light outside the LHCb acceptance, where it is detected by Hybrid Photon Detectors with 1024 pixels, Light cones are then reconstructed from the images obtained from these detectors and used for particle identification.

The **Calorimeters** [63] aim at the detection, energy measurement and identification of neutral particles and help in the separation of charged species. Four different sub-detectors, located downstream the magnet, form the calorimeter system: the Scintillating Pad Detector (SPD), the Pre-Shower (PS) detector, the Electromagnetic Calorimeter (ECAL) and the Hadronic Calorimeter (HCAL). All of them are composed by cells distributed in regions of different granularity, to account for the variation of the detector occupancy at different angles, with approximately projective segmentation in the direction of the PV.

The SPD, PS and ECAL deal with electromagnetic particles and are each divided in three regions

14

Figure 3.4: Reconstructed Cherenkov angle for isolated tracks, as a function of track momentum in the C_4F_{10} radiator.

of increasing cell sizes with matching granularity. The SPD is a binary detector that measures charged particle hits in a fast turnaround. This allows its usage in the first level of the trigger to account for the detector multiplicity, which is directly related to the SPD occupancy. Its other purpose is the separation of electrons and photons detected in the PS and the ECAL. The energy deposits reconstructed in these de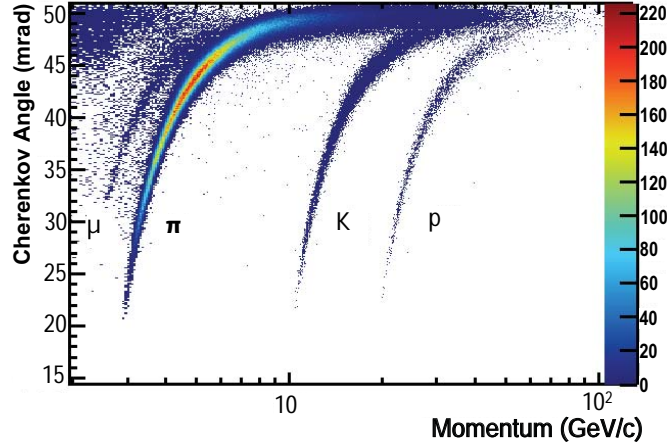tectors are extrapolated to the SPD and if the energy in the matching cell is above a certain threshold the particle is identified as an electron. The mis-identification rate of this detector for photons is around 0.8%. A layer of lead is placed downstream the SPD causing the start of an electromagnetic shower when a particle interacts with it. The dispersion of this shower is then measured by the PS in order to separate charged pions from electrons, achieving a 90% rejection of pions while selecting 90% of the electrons. The ECAL, situated right after the PS, at 12.5 m from the interaction region, aims at the measurement of the energy of the electromagnetic particles that are stopped in its material thanks to its 25 radiation length (X_0) thickness. It is composed of scintillator and lead layers read by perpendicular fibres that result in a fast response and high resistance to the intense radiation. Its design resolution is $\sigma(E)/E = 1\% + 10\%/\sqrt{E\,[\,\mathrm{GeV}\,]}$, in good agreement with the results of the test beam [64]. The Hadronic Calorimeter HCAL provides fast energy measurements for the trigger and input for the identification of hadron species. Due to restrictions of space in the LHCb cavern its length does not contain the full particle shower and thus the measured energy is just an estimate. It is formed by scintillating tiles separated by iron and its cells are distributed in two regions of increasing granularity.

Five stations (M1-M5) form the **Muon chambers** [65]. The first one is situated in front on the calorimeter system and provides input for the p_T measurement at trigger level. The other four stations are placed at the outermost part of the detector, since muons have a low interaction probability with matter and transverse the other sub-detectors without interacting, and are used for muon identification in the trigger and offline analysis and fast muon track reconstruction and p_T measurement in the trigger. They are based on Multi-Wired-Proportional-Chambers alternated with iron layers. Each station is segmented into four concentric regions with the cell size doubling that of the previous region.

The information from these sub-detectors is combined into charged particle identification variables. Two different types are widely used in physics analyses. The first is a combined logarithmic likelihood difference ($\mathrm{DLL}_{X\pi}$), which compares the probability of the particle being of type X to the probability of being a pion, the most abundant specie in the LHCb environment. The second type are a set of Neural Networks trained using information from all the sub-detectors, which give the probability of the particle

15

LHCb 2011 Trigger Diagram	LHCb 2012 Trigger Diagram	LHCb 2015 Trigger Diagram
40 MHz bunch crossing rate	**40 MHz bunch crossing rate**	**40 MHz bunch crossing rate**

L0 Hardware Trigger : 1 MHz readout, high E_T/P_T signatures

450 kHz $h^{\pm}$	400 kHz $\mu/\mu\mu$	150 kHz e/γ

Software High Level Trigger

26000 Logical CPU cores

Offline reconstruction tuned to trigger time constraints

Mixture of exclusive and inclusive selection algorithms

3.5 kHz (0.2 GB/s) to storage

1.5 kHz Inclusive Topological	1 kHz Inclusive/ Exclusive Charm	1 kHz Muon and DiMuon

L0 Hardware Trigger : 1 MHz readout, high E_T/P_T signatures

450 kHz $h^{\pm}$	400 kHz $\mu/\mu\mu$	150 kHz e/γ

Defer 20% to disk

Software High Level Trigger

29000 Logical CPU cores

Offline reconstruction tuned to trigger time constraints

Mixture of exclusive and inclusive selection algorithms

5 kHz (0.3 GB/s) to storage

L0 Hardware Trigger : 1 MHz readout, high E_T/P_T signatures

450 kHz $h^{\pm}$	400 kHz $\mu/\mu\mu$	150 kHz e/γ

Software High Level Trigger

Partial event reconstruction, select displaced tracks/vertices and dimuons

Buffer events to disk, perform online detector calibration and alignment

Full offline-like event selection, mixture of inclusive and exclusive triggers

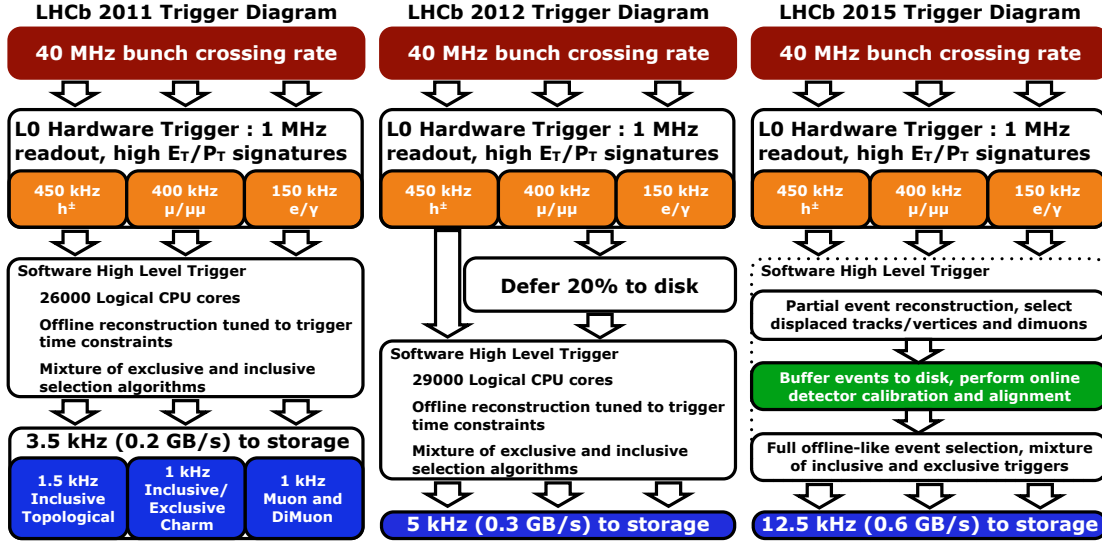**12.5 kHz (0.6 GB/s) to storage**

Figure 3.5: Diagrams of the LHCb trigger in 2011, 2012 and from 2015 onwards.

Table 3.1: L0 thresholds for the various signatures used during the different data-taking periods.

	Units	2011	2012	2015	2016
Single muon p_T	GeV	1.48	1.76	2.8	1.8
Di-muon $p_{T_1} \times p_{T_2}$	GeV^2	1.30^2	1.60^2	1.3^2	1.5^2
Hadron p_T	GeV	3.50	3.70	3.6	3.7
Electron p_T	GeV	2.50	3.00	2.7	2.4
Photon E_T	GeV	2.50	3.00	3.7	2.8

being of type X (ProbNNX). As an example of the performance, typically a kaon identification of $\sim 95\%$ is achieved with a $\sim 5\%$ $\pi \to K$ mis-identification probability.

Neutral particles such as photons and π^0 are identified by the calorimeter system. Dedicated variables combining information from the different sub-detectors are defined to separate them. Of special interest for radiative decays is the `IsPhoton` variable, based on a Neural Network, which is designed to discern between π^0 and photons at high energies. In Run 1 a photon efficiency around 98% was obtained with a π^0 rejection of 45% [66].

3.2.3 Trigger and offline systems

The LHC provides particle collisions at a rate of 40 MHz. The LHCb trigger is designed to select events that are interesting for b and c physics while reducing the rate to a manageable level. The trigger is divided in two major levels: the Level zero (L0) and the High Level Trigger (HLT), as shown in the diagrams on Figure 3.5.

The **L0** is implemented in hardware and selects high momentum signatures based on information from the calorimeters and the muon chambers. Additionally, very complex events are removed based on the SPD multiplicity. The L0 trigger has an output rate below 1 MHz at which the full detector can be read out. The transverse momentum and energy thresholds at which the different species are selected has evolved during the different data-taking periods to adapt to the LHC running conditions. A summary is presented in Table 3.1.

The **HLT** is a software application that runs on the Event Filter Farm and is in turn divided in two

sub-levels. In the **HLT1** a partial event reconstruction is performed. Displaced tracks and vertexes, which are a typical signature of beauty and charm decays, together with dimuons are selected at this stage. At **HLT2** a full reconstruction is performed and events are selected by a mixture of inclusive and exclusive criteria. During the first long shutdown of the LHC (2013-2014, LS1) the HLT underwent a major revision. The main features of the Run 1 and Run 2 triggers are detailed below:

- Run 1 HLT: some reconstruction algorithms in HLT2 were simplified with respect the offline version due to time constraints. Alignment and calibration of the detectors was later performed and the full dataset was then reprocessed to achieve high quality reconstruction. In 2012 a deferral strategy was adopted to optimise the use of resources. As illustrated in Fig. 3.5 (middle), 20 % of the events selected by the L0 were deferred to disk for processing by HLT during the interfill intervals. This allowed to relax some thresholds and increase the physics output.

- Run 2 HLT: upgrades in the computing resources and optimisations in the software allow to perform offline-level quality reconstruction in the trigger. In order to make the most out of the available resources, the HLT1 and HLT2 levels have been completely separated, as shown in Fig. 3.5 (right). This has caused major changes to the data flow: in collision mode, priority is given to HLT1 while its output is buffered to disk; during the interfill periods HLT2 takes all the resources. Both processes can run in parallel on the same nodes if needed. The asynchronous run of HLT1 and HLT2 allows to perform a full alignment and calibration of the detector in between the two steps, achieving offline quality reconstruction in HLT2 and opening the doors to real time analysis.

The properties of the HLT in Run 1 and Run 2 motivate different options for offline processing of the data. Two separate data streams are used for analysis:

- Full stream: the full raw event information is saved for events selected in this stream. This allows for later re-processing of the data if improved reconstruction algorithms or detector calibrations become available, as well as the possibility to build new candidates from the stored events for decays selected by a partial reconstruction at the trigger level and for cases not foreseen before the data-taking. After the offline reconstruction, the data is split in streams, defined as a sum of inclusive and exclusive selections expected to share part of the output, in order to optimise the resources. This step is referred to as stripping. This was the configuration used for physics analysis during Run 1 and the one used for the study of rare decays, among others, in Run 2.

- Turbo stream: it was introduced in Run 2 to exploit the offline quality reconstruction achieved in HLT2. It allows to perform analyses directly from the trigger candidates in a fast turnaround of few hours, since the offline re-processing of the data is not needed anymore. As an example, the J/ψ production cross-section measurement at 13 TeV [67] was first presented just one week after the data was recorded. The event size of this stream is one order of magnitude less than that in the full stream, since the raw information of the detector is not saved, allowing for high rate samples to be stored. The Turbo model is the benchmark trigger strategy at LHCb for the LHC runs from 2021 onwards (upgrade phase and beyond). In Run 2, it is under validation and only part of the data goes through this stream.

The studies reported in this thesis exploit the full stream data flow and its flexibility. The particular HLT and stripping selections used in each analysis are detailed in the relevant chapters.

Chapter 4

The inclusive radiative trigger in Run 2

Radiative decays of b hadrons are an excellent benchmark to search for BSM effects, as explained in Chapter 2. Exploiting the data sample collected during Run 1, LHCb has measured the branching ratio of the $B_s^0 \to \phi\gamma$ decay [68], the direct CP asymmetry ($\mathcal{A}^{CP}$) in the $B^0 \to K^{*0}\gamma$ transition [36] and has achieved the first observation and measurement of the photon polarisation in b-radiative decays exploiting the $B^+ \to K^+\pi^+\pi^-\gamma$ and $B_s^0 \to \phi\gamma$ modes [40, 42]. Other radiative channels provide complementary information to the ones already studied. In particular, $b \to d\gamma$ and radiative baryon decays are of special interest. An example of the later is presented in Chapter 6.

The HLT2 strategy to select samples for radiative analysis in Run 2 is presented in this chapter. First of all, the radiative trigger in Run 1 is shortly reviewed and then the development on an inclusive selection for Run 2 is detailed. Finally a comparison between the two in presented.

4.1 HLT2 for Radiative decays in Run 1

The samples collected in Run 1 for radiative analyses were triggered in a first stage by dedicated exclusive selections [69] based on the particular properties of the decays of interest, namely $B^0 \to K^{*0}\gamma$ and $B_s^0 \to \phi\gamma$. In 2011, following the strategy of the topological trigger [70], which selects generic b-hadron decays exploiting their common characteristics, cut-based inclusive lines[1] were included in order to exploit the distinctive features of radiative decays to select different modes in a single selection. Finally upgraded versions based on multivariate techniques were added in 2012 [71].

The main shortcomings of these configurations arose from the usage of a selection optimised for the more general topological trigger, which does not exploit the presence of a high energetic photon in the final state in the case of radiative decays. Moreover the selections were not very efficient for modes involving three or more hadrons plus the photon in the final state, since only the two track plus photon case was included. This motivated the development of dedicated two- and three-body plus photon configurations for Run 2.

4.2 The inclusive trigger for Radiative b-decays in Run 2

The radiative triggers in Run 2 are part of the full stream. This choice is motivated by the strong dependence of the selections on the ECAL reconstruction, which during 2015 was not fully aligned in its offline and online versions. In addition, improved calibrations of the calorimeters are normally available after the data-taking and the raw information of the detector is needed to benefit from them.

---

[1]HLT trigger selections are often referred to as trigger lines at LHCb. We shall use this concept throughout the thesis.

Table 4.1: Simulated signal samples used to optimise the radiative inclusive triggers.

2-Body selection	3-Body selection
$B^0 \to K^{*0}\gamma$	$B^+ \to K_1(1270)\gamma$
$B^0_s \to \phi\gamma$	$B^0_s \to \phi\phi\gamma$
$B^0 \to K^+\pi^-\gamma$	
$B^+ \to K^{*+}\gamma$	
$\Lambda^0_b \to \Lambda^*\gamma$	

Table 4.2: L0 and HLT1 filters included in the radiative inclusive triggers.

Trigger level	Requirement
L0	`L0Electron` or `L0Photon`
HLT1	`Hlt1TrackMVA` or `Hlt1TwoTrackMVA`

The HLT2 strategy for the selection of radiative decays in Run 2 follows a multivariate-based approach with improvements with respect to the Run 1 model. Two configurations, named `Hlt2RadiativeIncHHGamma` and `Hlt2RadiativeIncHHHGamma`, select combinations of two- and three-body candidates plus a high energetic photon, respectively. In addition to this, the exclusive selections of the main radiative channels, $B^0 \to K^{*0}\gamma$ and $B^0_s \to \phi\gamma$, are kept, together with dedicated configurations for decays of special topology, such as $\Lambda^0_b \to \Lambda\gamma$ and $B^0_s \to \gamma\gamma$.

The selection strategy for the inclusive lines follows that of the topological trigger [72], sharing with it the initial stages for timing optimisation. To start with, two- and three-particle combinations, including both charged hadrons and K^0_S and Λ, with a loose preselection are built. While the standard topological trigger applies afterwards a tighter selection on these combinations to build its candidates, the radiative lines combine them first with a high energetic photon, allowing the requirements on the hadrons to be looser. Finally, dedicated selections are applied to the photon plus hadrons combination exploiting the common decay topology of b-radiative decays.

Samples of various radiative decays simulated in 2015 conditions were used to optimise the selections. The candidates were filtered by matching the reconstructed particles to the generated ones and a photon with E_T above 1.5 GeV was required. For each decay mode 10^5 candidates were generated satisfying these conditions. Modes with two particles plus a photon in the final state were used to optimise the two-body selection while the three-body configuration was optimised with both decays with three and four particles apart from the photon in the final state. The signal samples are summarised in Table 4.1. A minimum bias sample simulated in the same conditions was used as background. The L0 and HLT1 trigger levels were emulated on all the samples and a filter, reported in Table 4.2, was applied on them. The HLT2 software was then used to save the candidates from the two- and three-body preselection for the optimisation of the final selection. The final configuration was retrained using the first data recorded by LHCb in 2015 as background to achieve a better performance.

In these lines, a preselection based on linear requirements is first applied to reduce the rate to a manageable level. Then a multivariate selection is used to remove the combinatorial background while selecting as much signal as possible. Both selections are based on common topological properties of b-radiative decays.

In the preselection, detailed in Table 4.3, requirements are imposed on the transverse momentum of the candidate, the quality of the vertex, the separation to the interaction point (FD), the pseudorapidity, defined as $-\log(\tan(\theta/2))$, where θ is the angle between the particle momentum and the beam axis, and the direction angle (DIRA) of the candidate, defined as the angle between the reconstructed momentum direction and the one defined by the interaction and decay vertices. To maintain the inclusiveness, no requirement on the invariant mass of the candidate is applied. Instead, the corrected mass defined as

$$m_{corr} = \sqrt{m^2 + |p_{T\,miss}|^2} + |p_{T\,miss}| \qquad (4.1)$$

Table 4.3: Soft selection applied on two- and three-body plus photon candidates.

Requirement	Units	Cut
p_{T} sum	GeV	> 2
Vertex $\chi^2/$dof		< 1000
Flight distance χ^2		> 0
Pseudorapidity		$\in (2,5)$
m_{corr}	GeV	$\in (1,10)$
Direction angle cos		> 0

Table 4.4: BBDT input variables for the `Hlt2RadiativeIncHHGamma` trigger in the 2015 and 2016 configurations.

2015 configuration	2016 configuration
IP χ^2	IP χ^2
IP χ^2 sum	-
-	IP χ^2 min
p_{T} min	-
max track χ^2	-
$\gamma\ p_{\mathrm{T}}$	$\gamma\ p_{\mathrm{T}}$
$m_{corr}(\mathrm{hh}\gamma)$	$m_{corr}(\mathrm{hh}\gamma)$
$m_{corr}(\mathrm{hh})$	$m_{corr}(\mathrm{hh})$
Flight distance χ^2	Flight distance χ^2
Vertex $\chi^2/$dof	Vertex $\chi^2/$dof
-	DOCA

where m is the reconstructed invariant mass and $|p_{\mathrm{T}miss}|$ is the missing transverse momentum with respect the candidate flight direction, is exploited. The corrected mass is meant to recover as much as possible the momentum lost by unreconstructed particles in partially reconstructed decays. For a single missing massless particle it recovers the mass of the head of the decay while its performance degrades with the number of missing particles. This allows to efficiently select decays involving three and four hadrons plus the photon in the final state.

A Bonsai Boosted Decision Tree (BBDT) [73] is chosen for the multivariate selection. The main characteristic of this classifier is that the input variables are discretised in a finite number of bins before using them in a standard Boosted Decision Tree (BDT) [74]. This provides stability to the response since on one hand fluctuations of the training data are not learnt and on the other small effects from data/MC discrepancies are smoothed. Moreover it presents a key advantage for its usage in the online software: since the input data is discretised, only a finite number of hypercuts can be applied to the n-dimensional variable space giving place to a finite number of hypercubes. Events in the same hypercube will be always classified in the same way, *i.e.*, the BDT response for all of them will be same, making it possible to build a look-up table identifying each hyperbin with a classifier response. At run time, this table is read by the HLT instead of running the multivariate selection for each candidate, speeding up a lot the response time. The only disadvantage is that having to load the lookup table into memory entails a limitation on the amount of variables and bins that can be used.

The input variables and their binning are chosen as a compromise between performance and complexity. On top of the variables used in the preselection, the impact parameter χ^2 (IP χ^2), defined as the variation in the χ^2 of the fit to the primary vertex with and without the track, and the distance of closest approach (DOCA) between the hadrons are used in the training. The complete list is reported in Tables 4.4 and 4.5 for the two- and three-body triggers, respectively.

Receiver Operator Characteristic (ROC) curves, shown in Figs. 4.1 and 4.2, are built for each signal

Table 4.5: BBDT input variables for the `Hlt2RadiativeIncHHHGamma` trigger in the 2015 and 2016 configurations.

2015 configuration	2016 configuration
IP χ^2	IP χ^2
IP χ^2 sum	-
-	IP χ^2 min
min p_{T}	-
-	max track χ^2
$\gamma\, p_{\mathrm{T}}$	$\gamma\, p_{\mathrm{T}}$
$\gamma\, p$	$\gamma\, p$
$m_{corr}(\mathrm{hhh}\gamma)$	$m_{corr}(\mathrm{hhh}\gamma)$
Flight distance χ^2	Flight distance χ^2
Vertex χ^2/dof	Vertex χ^2/dof

Table 4.6: Rate comparison of the radiative inclusive triggers in the 2015 and 2016 configurations.

	2015 rate (Hz)	2016 rate (Hz)
`Hlt2RadiativeIncHHGamma`	236 ± 7	203 ± 7
`Hlt2RadiativeIncHHHGamma`	63 ± 4	96 ± 5

mode as the trigger rate versus signal efficiency for varying BDT output cuts. The signal efficiency is computed with respect to the topological candidates. The estimated background rate assumes 1 MHz of L0 rate. The optimal requirement on the BBDT output is chosen taking into account the rate budget assigned to radiative triggers, 250 Hz and 50 Hz for the two- and three-body inclusive selections, respectively.

For the 2016 run the selections were re-optimised exploiting a much larger minimum bias sample recorded during 2015 and emulating the new L0 thresholds re-optimised for 2016 on the simulation samples. The new configurations are also presented in Tables 4.4 and 4.5. They represent an improvement, specially for the three body plus photon configuration, achieved thanks to the better performance of the classifiers and a slight redistribution of the rate budget. A comparison of the rates and selection efficiencies for the various signal samples are given in Table 4.6 and 4.7. The 2016 configuration was kept for the 2017 run and at the moment of writing there are no plans to update it for 2018.

Table 4.7: Comparison of the efficiency with respect to the topological preselection of the radiative inclusive triggers in the 2015 and 2016 configurations.

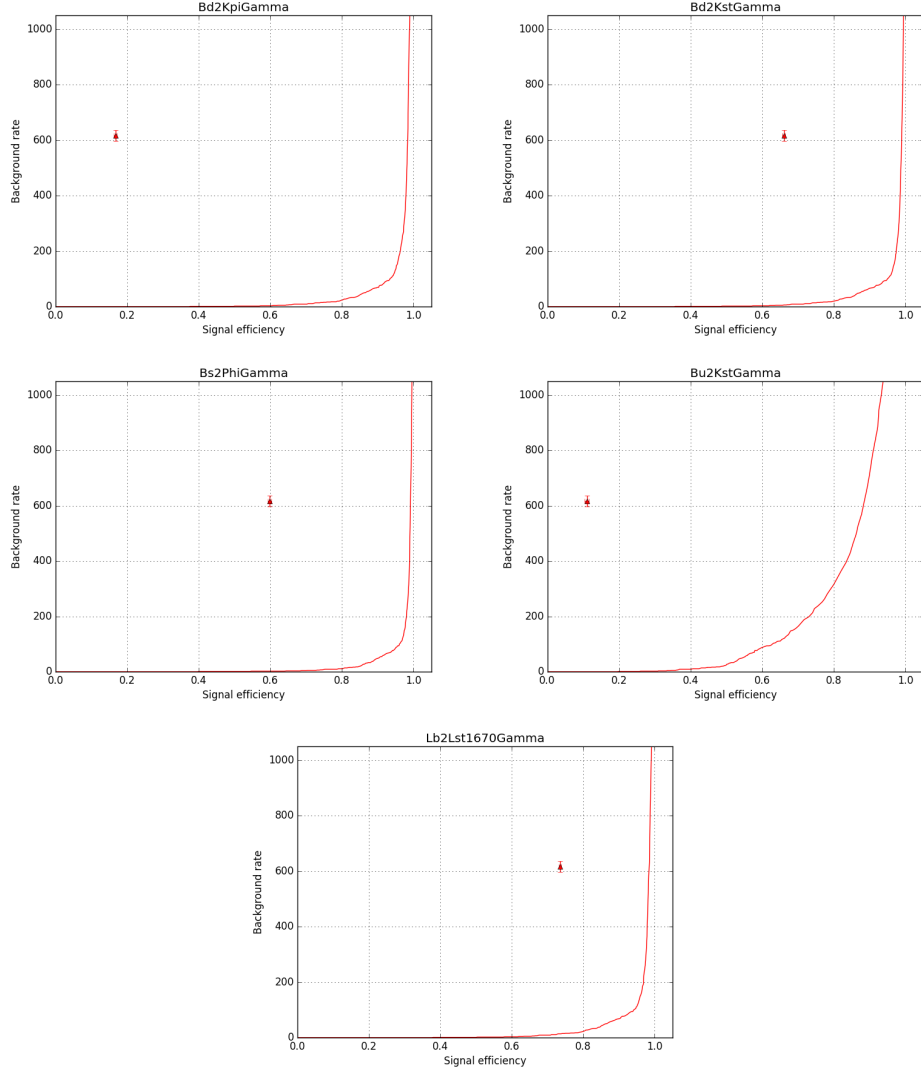| | `Hlt2RadiativeIncHHGamma` | | `Hlt2RadiativeIncHHHGamma` | |
Decay	2015	2016	2015	2016
$B^0 \to K^+\pi^-\gamma$	0.935±0.007	0.964±0.008		
$B^0 \to K^{*0}\gamma$	0.927±0.007	0.971±0.007		
$B^+ \to K^{*+}\gamma$	0.75±0.02	0.73±0.02		
$B_s^0 \to \phi\gamma$	0.941±0.07	0.972±0.07		
$\Lambda_b^0 \to \Lambda^*\gamma$	0.930±0.007	0.964±0.007		
$B^+ \to K_1(1270)\gamma$	0.838±0.007	0.908±0.007	0.695±0.0076	0.971±0.008
$B_s^0 \to \phi\phi\gamma$	0.279±0.004	0.298±0.004	0.449±0.006	0.938±0.009

Figure 4.1: ROC curves (solid line) showing the background rate as a function of the signal efficiency for the different simulation samples used in the optimisation of the two-body selection. The dot shows the efficiency and rate of the Run 1 selection for comparison.

4.3 Validation and performance

The performance of the new selections is evaluated by comparing the signal efficiency and background rate to those of the Run 1 triggers. For this, the Run 1 configuration is run on the same signal and background samples and the result is superimposed on the ROC curves on Figs. 4.1 and 4.2. For all the signal modes the efficiency is improved by an absolute 20% or more. This is particularly significant for the $B^0 \to K^+\pi^-\gamma$ and the $B^+ \to K^{*+}\gamma$ signal channels, for which an absolute 70% and 60% improvement is achieved, respectively. The first mode benefits from the usage of the missing mass instead of a direct requirement on the invariant mass of the two hadrons and proves the power of the new trigger in the selection of non-resonant modes, which were suppressed by the Run 1 trigger. The second mode is special in that it includes a K^0_S and a track, instead of two tracks, in the final state. The dedicated treatment of K^0_S in the construction on the two-body candidates in the topological trigger, considering them as final
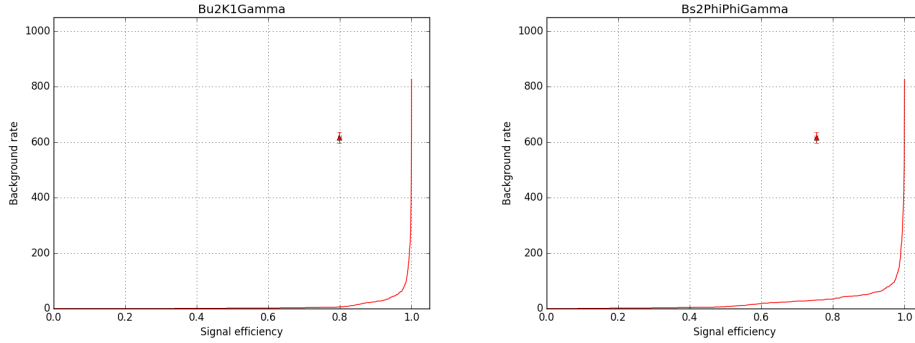
Figure 4.2: ROC curves (solid line) showing the background rate as a function of the signal efficiency for the different simulation samples used in the optimisation of the three-body selection. The dot shows the efficiency and rate of the Run 1 selection for comparison.

state particles instead of using the softer tracks of their decay, is in this case the main gain with respect the Run 1 approach.

Moreover, the rate of the inclusive trigger is reduced to a half with respect to the Run 1 configuration, which allows to dedicate the remaining budget to exclusive selections for decays with special topologies, expanding even more the reach of the radiative decays physics program. As an example, an exclusive selection for the $\Lambda_b^0 \to \Lambda\gamma$ mode could be included in the Run 2 trigger and is exploited in the analysis reported in Chapter 6.

The inclusive radiative selections were validated on data with the first $300\,\mathrm{pb}^{-1}$ recorded in 2015. $B^0 \to K^{*0}\gamma$ and $B_s^0 \to \phi\gamma$ candidates were built following the selections developed in [42]. The efficiency of the Hlt2RadiativeIncHHGamma trigger on these candidates is compared to that of the exclusive lines. The invariant mass distributions are fitted with a simple model consisting on a Gaussian for the signal and an exponential for the background, shown in Figs. 4.3 and 4.4, where the signal and background yields obtained from the fit are presented in a results box. It can be seen that the inclusive lines select as much signal as the exclusive ones or more while reducing the combinatorial background yield. These results confirm that these selections are properly implemented in the trigger software and selecting radiative candidates as expected. Moreover the performance of the new selections from this simple test is found to be slightly better than that of the exclusive triggers, which are designed with particular analysis needs in mind, such as a reasonable lifetime acceptance.
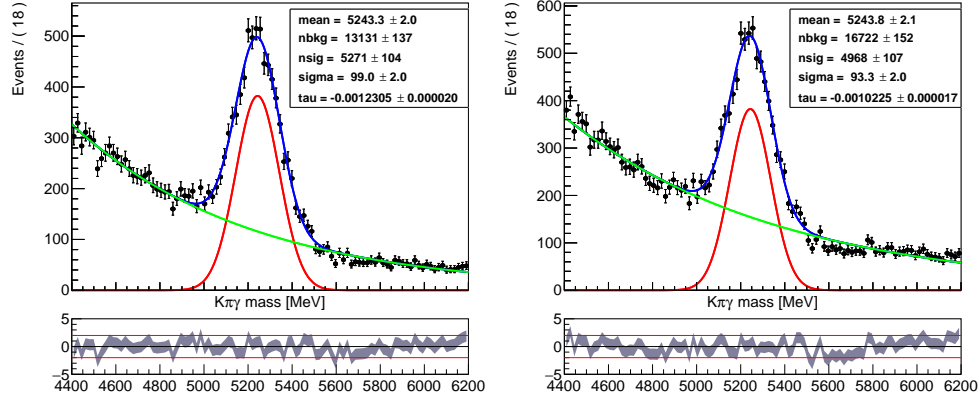
Figure 4.3: Invariant mass distributions of $B^0 \rightarrow K^{*0}\gamma$ candidates selected by `Hlt2RadiativeIncHHGamma` (left) and by the exclusive trigger (right). The results of a simple fit model are superimposed. 5271 ± 104 signal events are observed in the first case with a combinatorial background of 13131 ± 137, to be compared with 4968 ± 107 signal and 16722 ± 152 combinatorial candidates in the latter.

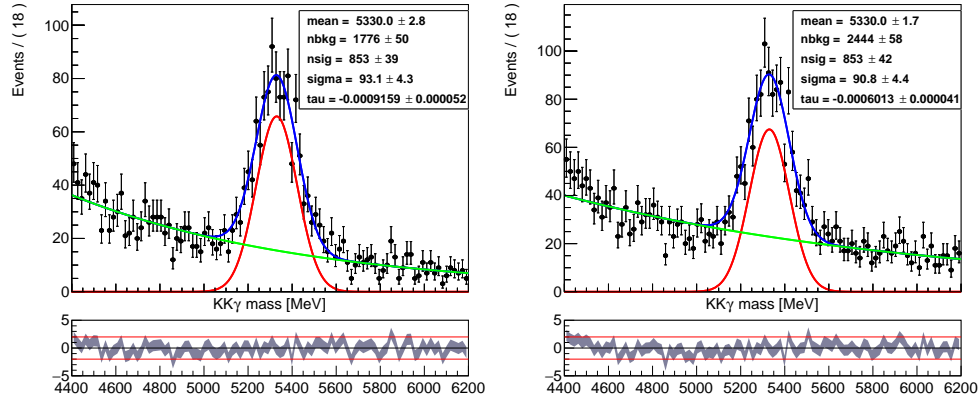Figure 4.4: Invariant mass distributions of $B_s^0 \rightarrow \phi\gamma$ candidates selected by `Hlt2RadiativeIncHHGamma` (left) and by the exclusive trigger (right). The results of a simple fit model are superimposed. 853 ± 39 signal events are observed in the first case with a combinatorial background of 1776 ± 50, to be compared with 853 ± 42 signal and 2444 ± 58 combinatorial candidates in the latter.

Chapter 5

Feasibility study of $K^0_S \to \pi^+\pi^- e^+ e^-$ at LHCb

5.1 Introduction

LHCb has proved to be very competitive in the search for rare strange decays with the improvement by a factor 35 of the world best upper limit on the branching fraction of the decay $K^0_S \to \mu^+\mu^-$ [75, 29] and the evidence for the baryonic $\Sigma \to p\mu^+\mu^-$ [30]. After these achievements, the interest in K^0_S decays at LHCb has grown considerably. Some other decays have been proposed to be searched for at LHCb, with special interest in $K^0_S \to \ell^+\ell^-\ell^+\ell^-$, where ℓ can be either an electron or a muon.

These decays have never been observed and no experimental limits are available in the literature [76]. The predicted branching fractions in the Standard Model (SM) are of the order [25]:

$$
\begin{aligned}
\mathcal{B}(K^0_S \to e^+e^-e^+e^-) &\sim 10^{-10} \\
\mathcal{B}(K^0_S \to \mu^+\mu^-e^+e^-) &\sim 10^{-11} \\
\mathcal{B}(K^0_S \to \mu^+\mu^-\mu^+\mu^-) &\sim 10^{-14}
\end{aligned}
\tag{5.1}
$$

The introduction of possible New Physics (NP) terms in the amplitude calculation could lead to dominant contributions, so any experimental deviation from the SM predicted values would be a hint to contributions from NP. Moreover, the measurement of the time interference of $\mathcal{A}(K^0_L \to \ell^+\ell^-\ell^+\ell^-)$ with $\mathcal{A}(K^0_S \to \ell^+\ell^-\ell^+\ell^-)$ would allow to extract the sign of $\mathcal{A}(K^0_L \to \gamma\gamma)$ needed for a precise determination of the short distance contribution to $K^0_L \to \mu^+\mu^-$ [25].

For those decays containing electrons in the final state the reconstruction of the electrons is the most challenging issue at LHCb, due to the low momentum they have in this decay and the large energy loss they suffer by Bremsstrahlung. Preliminary studies on simulated data allow to extract an expected mass resolution of 38 ± 8 MeV/c^2 for $K^0_S \to e^+e^-e^+e^-$, as shown in Fig. 5.1. These studies also show a clear displacement of the mass peak due to the energy loss of the electrons, with the peak of the distribution at 445 ± 6 MeV/c^2, to be compared to the K^0 mass of 497.611 ± 0.013 MeV/c^2 [76]. Similar studies could be performed for $K^0_S \to \mu^+\mu^-e^+e^-$ but no MC data is available at the moment of writing. Thus, $K^0_S \to \pi^+\pi^-e^+e^-$ events are used as a proxy given the similar topologies. An expected mass resolution of 6.4 ± 0.6 MeV/c^2 and a peak position at 492.9 ± 0.7 MeV/c^2 are obtained (see Fig. 5.1).

In addition to the mass resolution, the expected separation of the signal modes $K^0_S \to e^+e^-e^+e^-$ and $K^0_S \to \mu^+\mu^-e^+e^-$ to the copious background $K^0_S \to \pi^+\pi^-e^+e^-$, with the two pions misidentified as electrons or muons, is also checked. For this, $K^0_S \to \pi^+\pi^-e^+e^-$ simulated events are reconstructed changing the mass hypothesis of the two pions to two electrons and two muons, respectively. Figure 5.2 shows these distributions overlaid with the $K^0_S \to e^+e^-e^+e^-$ and $K^0_S \to \pi^+\pi^-e^+e^-$ reconstructed mass. The signal peaks can be discriminated from the $K^0_S \to \pi^+\pi^-e^+e^-$ one thanks to the good mass resolution.
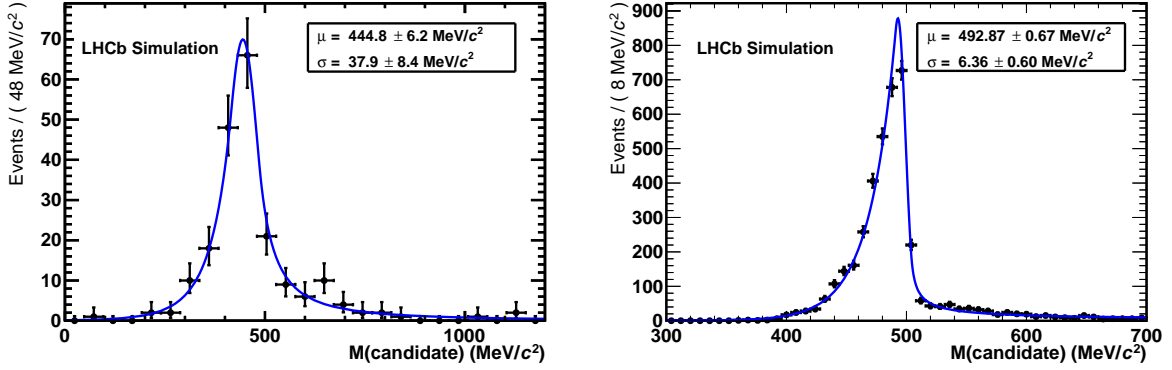
Figure 5.1: Invariant mass distributions of reconstructed MC $K_S^0 \to e^+e^-e^+e^-$ (left) and $K_S^0 \to \pi^+\pi^-e^+e^-$ (right) events. The continuous line shows the results of a fit with a double-tail Crystal Ball function [77].
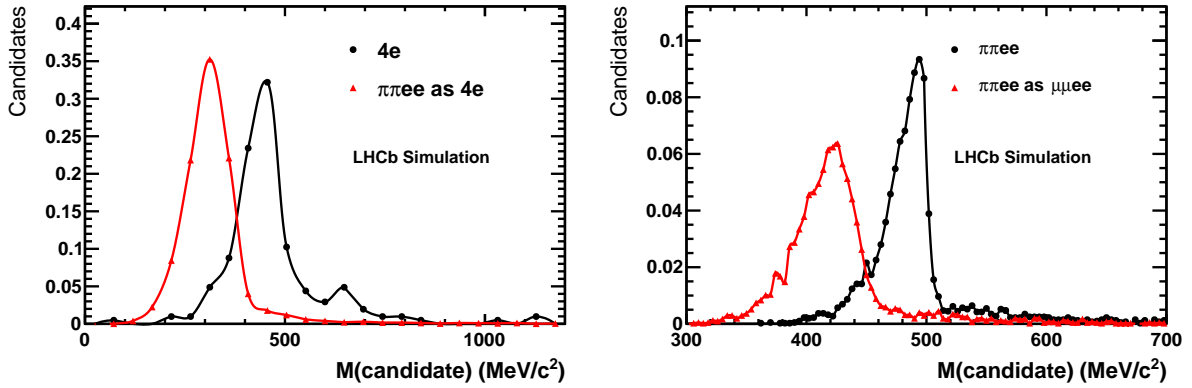

Figure 5.2: Mass distributions for reconstructed MC $K_S^0 \to e^+e^-e^+e^-$ and $K_S^0 \to \pi^+\pi^-e^+e^-$ events under the $e^+e^-e^+e^-$ mass hypothesis (left). And MC $K_S^0 \to \pi^+\pi^-e^+e^-$ events under the $\pi^+\pi^-e^+e^-$ and $\mu^+\mu^-e^+e^-$ mass hypotheses (right).

Nevertheless, the tails of the distributions overlap and therefore it becomes necessary to have this decay under complete control before being able to set a limit on the signal channels.

In addition, the $K_S^0 \to \pi^+\pi^-e^+e^-$ decay is the most obvious candidate as normalisation channel, given the similar topology to the signal channels, with four tracks including a di-electron in the final state. This channel is also interesting by itself as a place to look for new light dark matter states decaying dominantly to a pair of leptons that would peak in the di-electron invariant mass [78]. An example could be the search for dark photons using a strategy similar to the one proposed in Ref. [79]. The purpose of this study is to assess the feasibility of observing the $K_S^0 \to \pi^+\pi^-e^+e^-$ decay at LHCb.

The first observation of the $K_S^0 \to \pi^+\pi^-e^+e^-$ decay mode was obtained by NA48 using data collected in 1998. Based on a sample of 56 events, the branching ratio was measured to be $\mathcal{B}(K_S^0 \to \pi^+\pi^-e^+e^-) = (4.7 \pm 0.7 \pm 0.4) \times 10^{-5}$ [80]. This result was improved later on and the current world average is found to be $\mathcal{B}(K_S^0 \to \pi^+\pi^-e^+e^-) = (4.79 \pm 0.15) \times 10^{-5}$ [51], dominated by the most recent measurement of NA48 [81].

In this study, an offline selection is presented, different trigger configurations are considered and their efficiency to select $K_S^0 \to \pi^+\pi^-e^+e^-$ decays is extracted from simulated events. This allows to obtain the expected signal yield in pp collisions collected by LHCb during Run 1, which is afterwards checked

Table 5.1: Generator level requirements applied on the K_S^0 decay vertex.

Variable	Units	Cut value
(Vertex X + Vertex Y)^2	mm^2	$< 30^2$
Vertex Z	m	$\in (-1,1)$

by applying the same selection to the data. Finally, improvements for the trigger in Run 2 are presented and the expectations updated accordingly.

This chapter is organised as follows: the datasets are introduced in Sec. 5.2; then the selection and its efficiency are presented in Sec. 5.3 and the estimated signal and background yields in Run 1 are obtained in Sec. 5.4; these are then compared to the yields obtained in data in Sec. 5.5 and the improvements and expected yield in Run 2 are discussed in Sec. 5.6. Finally, conclusions and further improvements are proposed in Sec. 5.7.

5.2 Datasets

This study relies on MC samples reproducing the conditions of the 2012 LHCb data-taking. The *pp* collisions are generated using Pythia 8 [82] with a specific LHCb configuration [83]. The interaction of generated particles with the detector and its response are implemented using the Geant4 toolkit [84]. $K_S^0 \to \pi^+\pi^- e^+e^-$ events are generated with a tight selection applied at generator level to ensure the K_S^0 decays inside the sensitive region of the LHCb VELO, as detailed in Table 5.1. Its efficiency is 0.14479 ± 0.00036 (0.14487 ± 0.00036) for magnet up (down) conditions. More than 3×10^6 events are generated satisfying these requirements. To ensure that only signal decays are included in this sample, the reconstructed particles are matched to the MC generated ones and only those candidates coming from a real $K_S^0 \to \pi^+\pi^- e^+e^-$ decay are kept. A pure signal sample consisting of 4037 decays is obtained due to a reconstruction efficiency of $(0.134 \pm 0.002)\%$. For the background studies a minimum bias MC sample of 2×10^7 events with no requirements applied at generator level is used.

Moreover, *pp* collisions at $\sqrt{s} = 8$ TeV, recorded during the 2012 data-taking and corresponding to an integrated luminosity of $2\,\text{fb}^{-1}$ are used to check the estimations from the MC studies.

Finally, a larger MC signal sample, with more than 10^5 reconstructed and matched events, fulfilling the requirements in Table 5.1 and simulating the 2016 running conditions, is used for the development of a trigger selection included in the 2017 data-taking.

5.3 Offline and online selections

In order to assess the feasibility of observing the $K_S^0 \to \pi^+\pi^- e^+e^-$ decay at LHCb, the offline and online selection efficiencies are evaluated using the MC samples described in the previous section. The distribution of the $\pi^+\pi^- e^+e^-$ invariant mass for both the signal and the minimum bias samples[1] is shown in Fig. 5.3 (left). No events are reconstructed below ~ 300 MeV/c^2 due to the phase space left by the four final state particles. Signal decays present a clear radiative tail that is cut at low mass while the background distribution increases with mass due to the available phase space.

5.3.1 Offline selection

The selection of $K_S^0 \to \pi^+\pi^- e^+e^-$ candidates requires four tracks with good track fit quality, low probability of being a pseudorandom combination of hits (a ghost) and large IP χ^2 with respect to the primary vertex. Two of the tracks, with opposite sign, should have a large DLL$_{e\pi}$ and a minimum transverse

---

[1]The reconstruction of $K_S^0 \to \pi^+\pi^- e^+e^-$ candidates is detailed in Sec. 5.3.1. For this plot the selection requirements are not included.
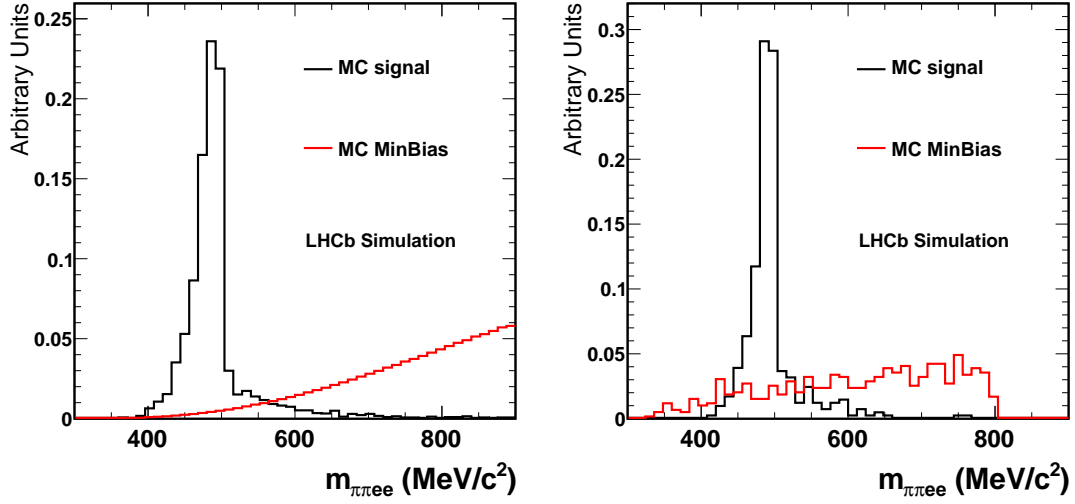
Figure 5.3: Normalised invariant $\pi^+\pi^- e^+ e^-$ mass distribution for $K_s^0 \to \pi^+\pi^- e^+ e^-$ (grey) and minimum bias (red) reconstructed MC candidates before (left) and after (right) the offline selection.

Table 5.2: Requirements applied on the offline selection of $K_s^0 \to \pi^+\pi^- e^+ e^-$ candidates in 2012 and 2015.

Selection	Units	2012	2015
track $\chi^2/ndof$		< 3	< 3
track ghost probability		< 0.5	< 0.5
track IP χ^2		> 16	> 16
e DLL$_{e\pi}$		> -4	> -4
e p_T	MeV/c	> 100	> 100
π DLL$_{K\pi}$		< 5	< 5
π p_T	MeV/c	> 250	> 100
e^+e^- DOCA	mm	> 10	> 100
e^+e^- invariant mass	MeV/c^2	> 250	> 100
e^+e^- p_T	MeV/c	> 250	> 100
$\pi^+\pi^- e^+ e^-$ max DOCA	mm	< 1.0	< 1.0
$\pi^+\pi^- e^+ e^-$ invariant mass	MeV/c^2	< 800	< 800
K_s^0 IP	mm	< 1	< 1
K_s^0 τ	ns	> 0.08953	> 0.08953
K_s^0 Vertex χ^2		$-$	< 50

momentum of 100 MeV/c. These tacks are combined requiring that the distance of closest approach and the invariant mass of the pair are small while the combined transverse momentum should be larger than 200 MeV/c. The two other tracks should have a small DLL$_{K\pi}$. Then the four tracks are combined to form a K_s^0 candidate by requiring that the maximum DOCA of each possible pair is small to ensure they come from the same decay vertex. In addition, the invariant mass should be smaller than 800 MeV. Finally, the K_s^0 direction is expected to point to the primary vertex, so its IP is required to be small while its decay time should be large. The selection is detailed in Table 5.2.

The efficiency of the selection on signal and background is $(10.1 \pm 0.5) \times 10^{-2}$ and $(2.95 \pm 0.12) \times 10^{-5}$, respectively, providing a large reduction of the huge combinatorial background. In the first case this

Table 5.3: Total trigger efficiency selecting $K_{\mathrm{S}}^0 \to \pi^+\pi^- e^+e^-$ and minimum bias events that satisfy the offline selection.

Trigger Selection	$K_{\mathrm{S}}^0 \to \pi^+\pi^- e^+e^-$ MC Efficiency (%)	MinBias MC Efficiency (%)
L0 & Hlt1 & Hlt2		
TIS TIS TIS	< 0.73	$0.85^{+0.38}_{-0.38}$
TIS TIS TOS	< 0.73	$0.51^{+0.49}_{-0.28}$
TOS TOS TOS	$0.24^{+0.56}_{-0.20}$	< 0.51

is evaluated with respect to reconstructed candidates matched to generated ones; in the second, the reconstruction efficiency is included here. The $\pi^+\pi^- e^+e^-$ invariant mass distribution for signal and minimum bias candidates fulfilling these requirements is shown in Fig. 5.3 (right).

This selection was updated to adapt it to the conditions of the 2015 data-taking. The main change was the loosening of the pion p_{T} requirement. Moreover, a new requirement on the K_{S}^0 vertex fit χ^2 was introduced in order to reduce the large multiplicity of candidates per event observed when testing the selection in Run 2 conditions. Detailed requirements can be found in Table 5.2.

5.3.2 Trigger selection in Run 1

In the offline selection, trigger signals are associated with reconstructed particles. Selection requirements can therefore be made on the trigger selection itself and on whether the decision was due to the signal candidate (TOS), to other particles produced in the pp collision (TIS), or a combination of both.

No specific trigger to select $K_{\mathrm{S}}^0 \to \pi^+\pi^- e^+e^-$ candidates was included during the Run 1 data-taking. However, this decay can be selected from the underlying event or as misidentified signal. Thus, the trigger strategy to select the decay consists of an OR of all the physics selections that were present in the trigger in Run 1, which are detailed elsewhere [85]. Both the TOS and TIS decisions are used for this purpose in order to select as much signal as possible.

The trigger efficiency is evaluated on signal and minimum bias simulated events that satisfy the offline selection. The total trigger efficiency, defined as

$$\epsilon^{trig} = \epsilon^{L0} \cdot \epsilon^{Hlt1} \cdot \epsilon^{Hlt2} = \frac{N^{trig}}{N^{sel}} \tag{5.2}$$

is reported in Table 5.3 for different combinations of TIS and TOS requirements at L0, HLT1 and HLT2. When no events are selected in the MC sample, a limit is set on the efficiency assuming a Poisson distribution, *i.e.*, that the number of selected events is ≤ 3 at 95 % CL.

The TIS TIS TIS condition is normally employed for decay modes without dedicated trigger selection, since one does not expect the signal candidate to fire a specific trigger line but other particles in the same event could. In this case, no signal events from the MC sample are selected by this requirement. This result can be compared to other similar channels involving decays of K_{S}^0, for which the trigger TIS efficiency is expected to be compatible since the underlying event in both cases is the result of a pp collision where an $s\bar{s}$ pair has been produced. In Ref. [86] the trigger TIS efficiency for $K_{\mathrm{S}}^0 \to \pi^+\pi^-$ was found to be $\epsilon^{TIS}_{K_{\mathrm{S}}^0 \to \pi^+\pi^-} = 0.1\%$, which is compatible with our result.

Only a TOS requirement at HLT2 is found to select signal candidates and therefore it is combined with both TIS and TOS conditions at L0 and HLT1. A single signal event satisfies the full trigger, corresponding to the TOS TOS TOS case. It is selected by the hadronic hardware requirement, which asks for a deposit in the hadronic calorimeter with a E_{T} larger than 3.74 GeV. At the software level, the HLT1 satisfied selection requires one track responsible for firing the hardware trigger with momentum greater than 3 GeV, transverse momentum larger than 1.6 GeV and impact parameter χ^2 with respect to the interaction vertex larger than 16. Finally, the signal candidate satisfies an HLT2 selection dedicated to charm hadron decays to three hadrons where three tracks, with no particle identification requirement,

coming from the same displaced vertex and compatible with the D^+ mass are required. No event from the MC minimum bias sample is selected by this same trigger combination. Signal yield studies are performed applying this particular trigger requirement.

The trigger is one of the main bottlenecks for the observation of this decay at LHCb. Dedicated HLT2 selections have been added for the Run 2 data-taking, as detailed in Sec. 5.6. However most of the signal is already lost in the previous trigger levels. This has been cross-checked with generated events with no reconstruction or detector effect on them. The tight requirements applied on the p and p_T of the tracks at L0 and HLT1 reject most of the signal and only 0.003% of the total generated events satisfies them. Thus this analysis would benefit a lot from the development of an HLT1 line dedicated to the selection of soft di-electrons.

5.4   Expected yields in Run 1

Expected signal and background yields are obtained in a tight mass window, 450–520 MeV, which selects $(76.9 \pm 1.8)\%$ of the signal. The expected number of $K^0_S \to \pi^+\pi^- e^+ e^-$ decays inside the LHCb detector fulfilling the offline selection and trigger requirements can be computed from the following expression:

$$N^{exp}_{sig} = N(K^0_S / \text{fb}^{-1}) \cdot \mathcal{B}(K^0_S \to \pi^+\pi^- e^+ e^-) \cdot \epsilon^{sig} \tag{5.3}$$

where $N(K^0_S / \text{fb}^{-1}) \sim 10^{13}$ is the number of K^0_S mesons decaying inside the LHCb acceptance [75],[2] $\mathcal{B}(K^0_S \to \pi^+\pi^- e^+ e^-) = (4.79 \pm 0.15) \times 10^{-5}$ [76] is the world average branching ratio for this decay and $\epsilon^{sig} = \epsilon^{sig}_{reco} \cdot \epsilon^{sig}_{sel} \cdot \epsilon^{sig}_{trig} \cdot \epsilon^{sig}_{mass}$. The efficiencies of reconstructing and selecting the signal decay have been obtained in Sec. 5.2 and 5.3, respectively, and the signal efficiency of the tight mass window requirement has been quoted above. The expected signal yield per fb^{-1} of LHCb data at 8 TeV is found to be:

$$N^{exp}_{sig} = 120^{+280}_{-100}$$

where the uncertainty is dominated by the MC statistics.

A similar technique can be used to estimate the expected background yield from MC:

$$N^{exp}_{bkg} = \sigma_{tot} \cdot \epsilon^{bkg} \tag{5.4}$$

where $\sigma_{tot} = (94.6 \pm 0.3)\,\text{mb}$ is the total cross-section simulated in the MC minimum bias sample and $\epsilon^{bkg} = \epsilon^{bkg}_{reco} \cdot \epsilon^{bkg}_{sel} \cdot \epsilon^{bkg}_{trig} \cdot \epsilon^{bkg}_{mass}$. The reconstruction and selection efficiencies have been obtained in Sec. 5.3 and the tight mass cut efficiency is found to be $(4.33 \pm 0.02)\%$. With these numbers, the expected background yield after the full selection is:

$$N^{exp}_{bkg} \leq 6.1 \times 10^5 / \text{fb}^{-1} \text{ at 95\% CL}$$

5.5   Studies on Run 1 data

Looking at the data sample described in Sec. 5.2 after the full selection, no peak is observed in the $\pi^+\pi^- e^+ e^-$ invariant mass distribution as shown in Fig. 5.4. The number of background events present in the signal region in $2\,\text{fb}^{-1}$ of data is found to be:

$$N^{obs}_{bkg} \sim 6 \times 10^3 \tag{5.5}$$

which is compatible with the expectation obtained from the minimum bias MC sample in the previous section.

Taking into account the expected signal yield corresponding to 2 fb^{-1} of LHCb data, $N^{exp}_{sig} \sim 240$, it could be possible to observe this decay already with the Run 1 dataset by further applying a high-efficiency

[2]This number has been cross checked using $K^0_S \to \pi^+\pi^-$ candidates from the 8 TeV dataset.
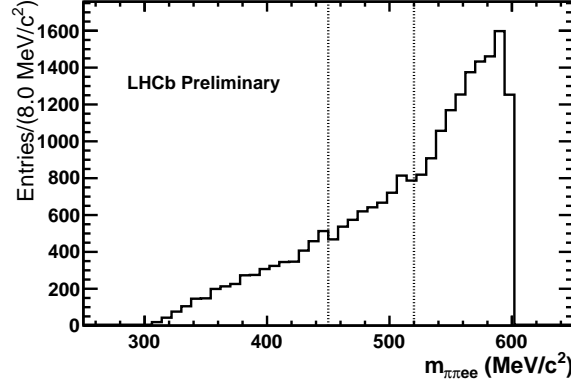
Figure 5.4: Invariant $\pi^+\pi^- e^+ e^-$ mass distribution for candidates satisfying the offline selection and trigger requirements. The signal region, 450–$520\,\mathrm{MeV}/c^2$, is delimited by dashed lines.
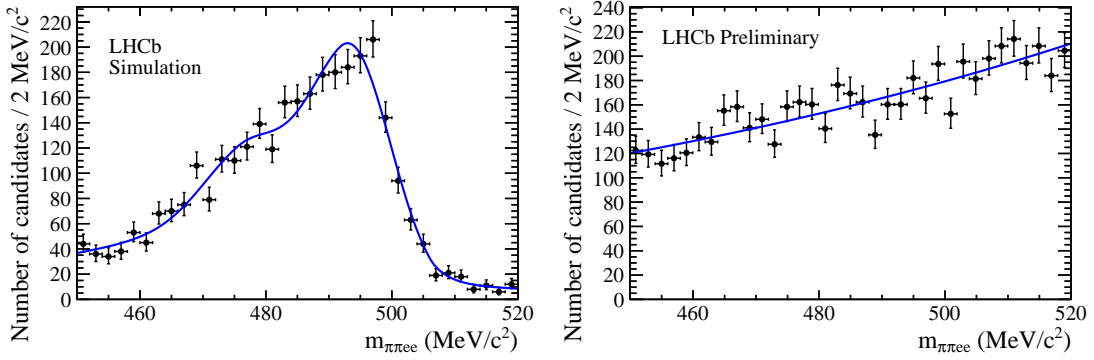

Figure 5.5: Fit to extract the signal (left) and background (right) PDFs. The left fit has been performed with $K_S^0 \to \pi^+\pi^- e^+ e^-$ MC matched candidates, while the right one uses the selected Run 1 dataset. The fitted PDFs are two double Crystal Balls (left) and an exponential (right).

large-rejection selection. A multivariate (MVA) selection would be appropriate in this case. Additionally, dedicated tools for the selection of low momentum electrons could help to further discriminate signal from background. The development of such selection would require a larger MC signal sample.

In order to study the possibility of an observation or evidence in a more quantitative way, a toy study has been performed, based on the expected signal and observed background yields, together with the corresponding mass Probability Density Functions (PDFs). For this, the signal mass window is first chosen, 450–520 MeV/c^2, in which ~ 240 signal and ~ 5600 background candidates are expected in $2\,\mathrm{fb}^{-1}$ (with the signal component present in data neglected in this case).

As a first step, an unbinned maximum likelihood fit using $K_S^0 \to \pi^+\pi^- e^+ e^-$ MC matched candidates (assuming the selection and trigger do not bias the mass distribution of the signal) and the selected Run 1 dataset is performed. Two double Crystal Ball [77] and an exponential PDF are fitted to the signal and background datasets, respectively. The PDF mass model for the signal is selected empirically, and not optimised. For an actual search in data, a more detailed study shall be performed to choose this model. The result of these fits can be found in Fig. 5.5. Once these PDFs are obtained, they are frozen for the rest of the study.

Using the PDFs obtained for signal and background, pseudoexperiments are performed to evaluate a
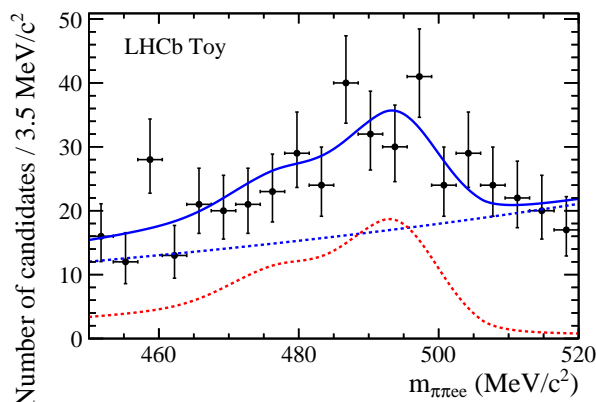
Figure 5.6: Example of a fit, which would provide a 5σ observation, using Wilks' theorem. In this case, the pseudodata contains 136 signal and 350 background candidates. This would correspond to a signal efficiency on the signal mass window (450–520 MeV/c^2) of $\sim 55\%$ and a background rejection of $\sim 95\%$.

possible observation or evidence. For each point out of a list of signal yields (corresponding to different signal efficiencies), different background yields are tested. Then, for each pair of signal and background yields, 10000 pseudodatasets are generated and a fit is performed for each of them. In each of the pseudoexperiments, the actual distributions are floated according to the errors of the PDFs obtained above. After this, Wilks' theorem [87] is used to extract the significance of the signal in each case. Figure 5.6 shows an example of one of these toys, which would provide a 5σ observation.

The procedure just described allows obtaining, for each signal yield, curves of significance vs. background yield. These curves can be obtained for the central value of each background yield and also to constrain 68% C.L. regions. In order to obtain the exact background corresponding to significances of 3 and 5σ, a simple exponential fit is performed to interpolate the correct values. Figure 5.7 shows one of these fits. From this, the curves in Fig. 5.8, showing the background rejection vs. signal efficiency required to obtain 3 and 5σ signal significance, can be finally obtained. Both curves are well within the usual discrimination achieved by standard MVA selections, which reinforces the conclusion that an evidence or observation is possible using only Run 1 data.

5.6 Expected yields in Run 2 and beyond

The expected $K_S^0 \to \pi^+\pi^- e^+ e^-$ yield per fb^{-1} of LHCb data at 8 TeV has been obtained in the previous sections with the conclusion that one of the main bottlenecks in the search for this decay is at the trigger level. Therefore dedicated HLT2 selections have been developed for the Run 2 data-taking exploiting the flexibility of the LHCb trigger. They are detailed in the following.

5.6.1 New inclusive HLT2 selection in 2016

A new HLT2 line, named `Hlt2DiElectronElSoft`, was developed (by the Santiago group) and included in the trigger starting in 2016 in order to inclusively select K_S^0 decays into a di-electron pair, allowing the selection of both $K_S^0 \to \pi^+\pi^- e^+ e^-$ and $K_S^0 \to \ell^+\ell^-\ell^+\ell^-$ events. The selection was optimised using the same MC signal sample as in our studies (since no sample in Run 2 conditions was available at that time), after requiring the matching of the reconstructed particles to the MC signal. Details can be found in Ref. [88]. We evaluate the total trigger efficiency when combining the new HLT2 line with the different L0 and HLT1 requirements presented in Sec. 5.3.2, showing the results in Table 5.4. Other combinations give no efficiency on the signal. It can be observed that only $K_S^0 \to \pi^+\pi^- e^+ e^-$ candidates passing the
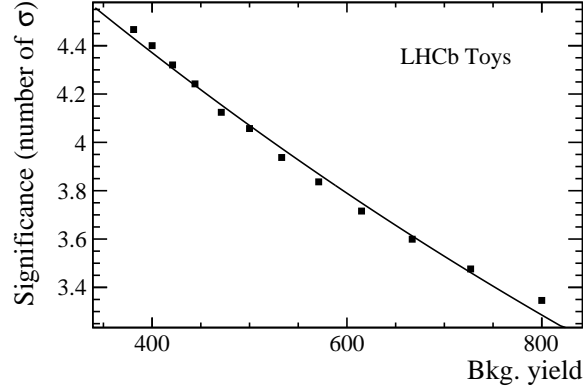
Figure 5.7: Example of a curve of significance vs. background yield, corresponding to a signal efficiency of ∼55%. For each x axis point, 10000 toys were generated and significances calculated with the Wilks' theorem, with the y axis representing the median of all the significances obtained. An exponential fit is also showed, used to obtain the background yields corresponding exactly to 3 and 5σ. Similar fits were performed to obtain the background yields to constrain 68% C.L. regions.
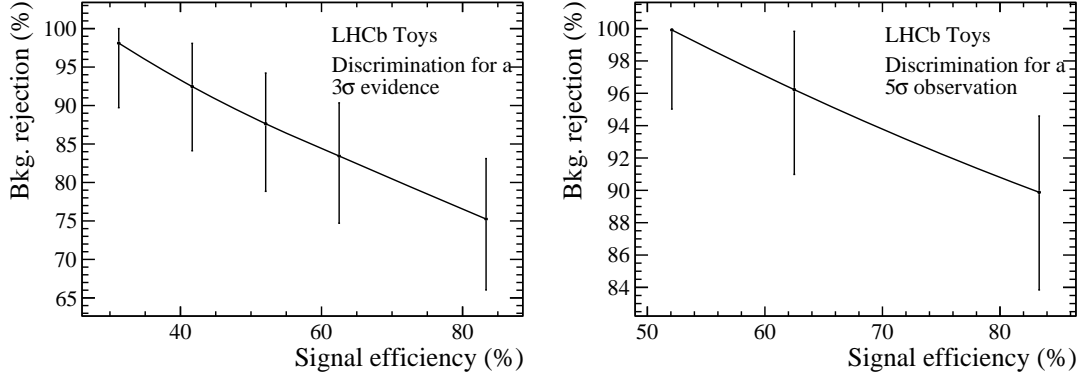
Figure 5.8: Signal efficiency vs. background rejection curves needed to obtain a 3σ evidence (left) or 5σ observation (right) of $K_{\mathrm{s}}^0 \to \pi^+\pi^- e^+e^-$ using the LHCb Run 1 dataset. The error bars correspond to 68% C.L. variation in the toys for each expected signal yield. .

L0 and HLT1 levels as TIS are selected by this line. This is expected since only very soft requirements on the p_{T} of the tracks are included in the selection.

Table 5.4: Total trigger efficiency selecting $K_{\mathrm{s}}^0 \to \pi^+\pi^- e^+e^-$ events when applying `Hlt2DiElectronElSoft` on top of different HLT1 and L0 requirements.

L0 & HLT1 & HLT2	Efficiency (%)
TIS TIS TOS	$0.24^{+0.56}_{-0.20}$
TOS TOS TOS	< 0.73

Figure 5.9: Invariant $\pi^+\pi^- e^+ e^-$ mass distribution for signal MC candidates reconstructed with (blue) and without (red) the Bremsstrahlung correction.

5.6.2 New exclusive HLT2 selection in 2017

In order to exploit also the high momentum signal candidates that can satisfy the tight requirements of these levels, as it was the case for the signal event selected as TOS TOS TOS by the Run 1 trigger, a second dedicated HLT2 selection, `Hlt2RareStrangeKsPiPiEETOS`, was developed and included in the trigger in 2017.
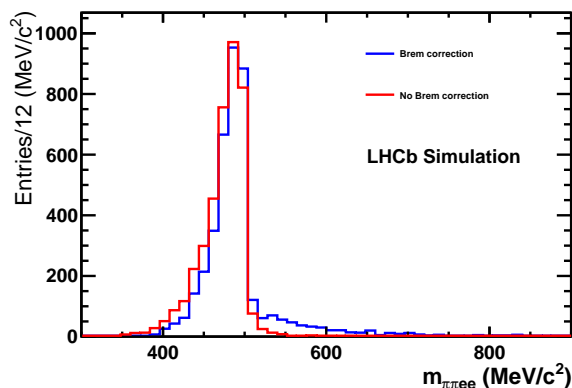
It consists of an exclusive selection based on the requirement that the candidate is responsible for firing the trigger both at L0 and HLT1. Since the pions in the decay are harder in average than the electrons, they have a higher probability of satisfying the L0 and HLT1 requirements. Further cuts exploit this property by selecting harder pions while avoiding strong constraints on the electrons: a minimum p_T of 500 and 80 MeV is required on the pions and the electrons, respectively.

Another key point of this selection is that it reconstructs the signal without correcting the electron momenta for possible Bremsstrahlung losses. This allows to set a stringent requirement on the maximum invariant mass of the candidates since the signal tail at high mass is largely reduced, as shown in Fig. 5.9. At the same time, the tail at low mass is enlarged so no constraint on the minimum mass of the candidate is applied. Therefore this selection is expected to be also efficient selecting $K_S^0 \to \pi^+\pi^-\gamma$ decays where the γ decays to an electron pair. The complete study on the effect of the Bremsstrahlung correction on the invariant mass shape of $K_S^0 \to \pi^+\pi^- e^+ e^-$ candidates can be found in Appendix B.

On top of this, the line follows the offline selection developed for Run 1 with tighter requirements to reduce the rate to a suitable level for the trigger. Additionally, the K_S^0 candidate should have a minimum p_T of 1500 MeV/c and the cosinus of the angle between its reconstructed momenta and the direction defined by the PV and its decay vertex, referred to as Direction Angle (DIRA), is required to be larger than 0.9999. The exact requirements included in this selection, summarised in Table 5.5, have been optimised exploiting the new MC sample generated in Run 2 conditions described in Sec. 5.2.

The efficiency of this trigger line, reported in Table 5.6, is directly evaluated on reconstructed and MC matched signal candidates from this sample. It can be seen that the L0 requirement is the most stringent one, rejecting the largest proportion of signal candidates. An offline selection aligned with the trigger has been defined providing a $\sim 100\%$ efficiency on top of this.

5.6.3 Expected yields

Assuming no other improvements have been achieved in Run 2 and also neglecting the increase in the K_S^0 production cross section and flight distance from 8 to 13 TeV, the expected yield per fb^{-1} in Run 2

Table 5.5: Requirements of the `Hlt2RareStrangeKsPiPiEETOS` exclusive selection included in the trigger in 2017.

Selection	Units	Requirement
L0 TOS		Hadron or Electron or Muon
HLT1 TOS		TrackMVA or TwoTrackMVA or TrackMuon or
		SingleMuonNoIP or DiMuonLowMass
track $\chi^2/ndof$		< 3
track ghost probability		< 0.3
e p_T	MeV/c	> 80
e DLL$_{e\pi}$		> -2
π p_T	MeV/c	> 500
π IP χ^2		> 9
$\pi^+\pi^- e^+e^-$ max DOCA	mm	< 0.5
$\pi^+\pi^- e^+e^-$ invariant mass	MeV/c^2	< 825
K_S^0 IP	mm	< 0.3
K_S^0 IP χ^2		< 150
K_S^0 Flight Distance χ^2		> 150
K_S^0 Vertex χ^2		< 16
K_S^0 p_T	MeV/c	> 1500
K_S^0 M	MeV/c^2	< 550
K_S^0 DIRA		> 0.9999

Table 5.6: Trigger efficiency of `Hlt2RareStrangeKsPiPiEETOS` on $K_\mathrm{S}^0 \to \pi^+\pi^- e^+e^-$ events. The effect of the L0 and HLT1 requirements included in the selection is given explicitly.

Requirement	Efficiency (%)
L0 TOS	$1.17 +/- 0.04$
HLT1 TOS	$10.9 +/- 1.2$
Linear cuts	$67 +/- 11$
Total	$0.085 +/- 0.011$

conditions is:

$$
\begin{aligned}
N_{TISTISTOS}^{exp} &= 120^{+280}_{-100} \\
N_{TOS}^{exp} &= 500 \pm 70 \\
N_{Total}^{exp} &= 620^{+290}_{-120}
\end{aligned}
$$

s The L0 and HLT1 requirements ensure that the candidates selected by the TIS TIS TOS chain in Table 5.4 and those selected by the exclusive `Hlt2RareStrangeKsPiPiEETOS` line, simply referred to as TOS, are completely disjoint, i.e. fully complementary. Thus the total yield expected in Run 2 is the direct sum of these.

Beyond the LHC Run 2, during its upgrade phase, the LHCb trigger will be fully based on software [89]. This will allow to have many dedicated selections exploiting the full event reconstruction at trigger level. In the ideal scenario a signal efficiency of $\sim 100\%$ can be achieved. With this assumption, the expected yield of $K_\mathrm{S}^0 \to \pi^+\pi^- e^+e^-$ per fb^{-1} in the upgrade phase is expected to be:

$$
N_{sig}^{upgrade} = (5.0 \pm 0.3) \times 10^4
$$

Assuming the background can be kept under control, this yield would allow not only a clear observation of this mode but also to set stringent limits on the $K^0_{\mathrm{S}} \to \ell^+\ell^- e^+ e^-$ decays and to search for peaks in the di-electron invariant mass distribution.

5.7 Results and conclusions

The feasibility of observing the $K^0_{\mathrm{S}} \to \pi^+\pi^- e^+ e^-$ decay with the Run 1 LHCb dataset has been studied using MC samples. The expected signal yield corresponding to $1\,\mathrm{fb}^{-1}$ of data at $8\,\mathrm{TeV}$ is found to be:

$$N^{exp}_{\mathrm{Run1}}(K^0_{\mathrm{S}} \to \pi^+\pi^- e^+ e^-) = 120^{+280}_{-100}$$

where the uncertainty is dominated by the MC statistics.

No hint of signal is observed in the 2012 dataset corresponding to an integrated luminosity of $2\,\mathrm{fb}^{-1}$ while the total background amounts to:

$$N^{obs}_{\mathrm{Run1}}(bkg) \sim 6 \times 10^3$$

The two bottlenecks for the observation of this decay are the reconstruction efficiency, which is found to be very low due to the presence of low momentum electrons in the decay, and the trigger efficiency, in particular the tight p and p_{T} requirements present in the L0 and HLT1 trigger levels. Two dedicated HLT2 lines have been developed and included in the trigger at the beginning of the 2016 and 2017 data-taking, which allow to select those events passing these two levels independently and due to the signal, respectively. With both improvements, the total expected yield corresponding to $1\,\mathrm{fb}^{-1}$ of Run 2 data is found to be:

$$N^{exp}_{\mathrm{Run2}}(K^0_{\mathrm{S}} \to \pi^+\pi^- e^+ e^-) = 620^{+290}_{-120}$$

In the LHC upgrade phase with a full software trigger at LHCb, a signal efficiency of $\sim 100\%$ can be achieved. Under this assumption the signal yield per fb^{-1} is expected to be:

$$N_{\mathrm{Upgrade}}(K^0_{\mathrm{S}} \to \pi^+\pi^- e^+ e^-) = (5.0 \pm 0.3) \times 10^4$$

These results also show that the observation of this decay with the Run 1 dataset would require the development of a further high-efficiency large-rejection selection. Pseudoexperiments have been generated, based on the expected signal and observed background yields, to assess the background discrimination needed to obtain an evidence or observation of this decay. Both are well within the usual discrimination achieved by standard MVA selections, which reinforces the conclusion that such outcome could be possible using only Run 1 data. Moreover, other tools dedicated to the selection of decays with electrons could help to further discriminate signal from background.

In Run 2, the improved trigger efficiency guarantees an observation of this mode. During the upgrade phase, the large expected signal yield would allow to set stringent constrains in the $K^0_{\mathrm{S}} \to \ell^+\ell^- \ell^+\ell^-$ decays and search for new resonances in the di-electron invariant mass distribution of the signal.

While more data is collected, other decays such as $K^0_{\mathrm{S}} \to \pi^+\pi^-$ or $K^0_{\mathrm{S}} \to \pi^+\pi^-\gamma$ could be used as normalisation channel in the search for $K^0_{\mathrm{S}} \to \ell^+\ell^- \ell^+\ell^-$, although the possible contamination from $K^0_{\mathrm{S}} \to \pi^+\pi^- e^+ e^-$ would need to be carefully assessed.

Chapter 6

Search for $\Lambda_b^0 \to \Lambda \gamma$ at LHCb

6.1 Introduction

The $\Lambda_b^0 \to \Lambda\gamma$ decay is a flavour-changing neutral-current mediated by the $b \to s\gamma$ quark level transition, a diagram of which can be found in Fig. 2.2. As such it is very sensitive to New Physics (NP) effects that can contribute to the penguin loop modifying the decay properties from those predicted by the Standard Model (SM). While mesonic $b \to s\gamma$ decays have been studied in detail before at b-factories [33, 34, 35] and also at LHCb [36, 40, 90], baryonic b-radiative processes are still largely unexplored and can provide new insights into the structure of the SM Lagrangian. In particular, as discussed in Sec. 2.3.2, the $\Lambda_b^0 \to \Lambda\gamma$ mode allows a direct measurement of the photon polarisation, predicted to be almost 100% left-handed in the SM but to which right-handed currents can contribute in NP models. Thus a measurement of this quantity would provide a stringent test of the SM.

The $\Lambda_b^0 \to \Lambda\gamma$ decay has never been observed and an upper limit on its branching fraction was set by CDF at $\mathcal{B}(\Lambda_b^0 \to \Lambda\gamma) < 1.3 \times 10^{-3}$ at 95% C.L. [43]. The SM prediction is at the level of $(0.06 - 1) \times 10^{-6}$ [45, 46, 47, 48], with the short-distance contribution well under control from the measurement of other $b \to s\gamma$ transitions and the long-distance one expected to be very small [49, 44]. The main source of discrepancy between different predictions comes from the $\Lambda_b^0 \to \Lambda$ form factor at $q^2 = 0$, $F(0)$, entering in Eq. 2.11. A precise measurement of the branching ratio of this decay would allow to discriminate between different approaches to the form factor computation. Moreover the observation of the $\Lambda_b^0 \to \Lambda\gamma$ transition is the first milestone towards the measurement of the photon polarisation in this decay.

LHCb has the unique opportunity to search for this decay thanks to the large production of Λ_b^0 baryons in the proton-proton collisions at the LHC. However its special topology makes its experimental reconstruction challenging. First investigations based on simulation were fulfilled before LHCb started taking data, providing an experimental method to extract the value of the photon polarisation [91]. The data collected during the years 2011 and 2012 was later analysed and no hint of this decay was found [92]. It was noticed at that time that the main bottleneck in the selection of this decay was at the trigger level. Thanks to the flexibility of the LHCb trigger system a dedicated selection was included starting from the 2015 data-taking period.

A search for the $\Lambda_b^0 \to \Lambda\gamma$ decay is performed here using the pp dataset recorded by the LHCb detector during the 2016 run, corresponding to an integrated luminosity of $1.7\,\text{fb}^{-1}$. Only a small improvement is expected from the addition of the data collected during 2015, corresponding to an integrated luminosity of $0.3\,\text{fb}^{-1}$, which would require a special treatment due to a worse calorimeter calibration during this period. Therefore this dataset is not included in this analysis.

The aim of the study presented in this chapter is the search for this decay and the measurement of its branching fraction. Its special topology, including a long-lived particle and a photon, motivates the development of a dedicated selection both in the trigger and in the offline analysis, which is explained in detail in Sec. 6.3. Simulated Monte-Carlo (MC) samples are used to optimise the selection and obtain

Table 6.1: MC samples used for this analysis, generated statistics split in simulated magnet polarity, topological and generator level requirements. The abbreviation tr refers to any charged particle in the decay chain, i.e. a track.

Decay	Statistics		Topological cuts	Generator level cuts
	Magnet Up	Magnet Down		
$\Lambda_b^0 \to \Lambda\gamma$	18602252	18398527	$p_z(\Lambda_b^0) > 0$	-
$B^0 \to K^{*0}\gamma$	1913632	1768861	$10 < \theta(\mathrm{tr}) < 400\,\mathrm{mrad}$	$p_\mathrm{T}(\gamma) > 1500\,\mathrm{MeV}$
$\Lambda_b^0 \to \Lambda J/\psi$	12804499	12738932	$10 < \theta(\mu^\pm) < 400\,\mathrm{mrad}$	-
$\Lambda_b^0 \to pK^- J/\psi$	5111059	5192309	$10 < \theta(\mathrm{tr}) < 400\,\mathrm{mrad}$	-

its efficiency. Consequently it is important to ensure MC reproduces the detector effects accurately. To achieve this goal, high rate modes with similar topology to the signal are exploited. The agreement between simulation and background-subtracted data is checked for all the variables included in the selection and corrections are obtained when needed, as detailed in Sec. 6.3.4.

The branching fraction is then measured with respect to the well-known $B^0 \to K^{*0}\gamma$ decay. This allows to avoid systematic uncertainties from the knowledge of the exact recorded luminosity and the $b\bar{b}$ cross-section and to cancel other systematic effects coming from the reconstruction and selection of the photon in the final state. Section 6.4 explains in detail the normalisation strategy. The yields in data of the signal and normalisation modes are obtained from an unbinned maximum likelihood fit to the selected candidates following a blind approach in order to avoid any possible experimental bias. The data side-bands are first fit with the background model to ensure the different contributions are understood and under control. Only after testing that the fit is stable under different assumptions for the signal yield in the expected range of theory predictions, the fit to the full invariant mass distribution is performed. A measurement of the branching fraction is extracted directly from the fit. The fit strategy, signal and background model definition and the final fit to data are reported in Sec. 6.5. Sources of systematic uncertainty are considered and evaluated in Sec. 6.6. The final results are presented in Sec. 6.7 and their interpretation, possible improvements and future measurements are discussed in Sec. 6.8.

6.2 Data samples

The results described in this chapter are obtained using the data collected by the LHCb experiment during the 2016 LHC run corresponding to an integrated luminosity of ~ 1.7 fb^{-1} at a center of mass energy of $\sqrt{s} = 13$ TeV.

Simulated samples reproducing the 2016 data-taking conditions are also used in order to develop the selection, obtain efficiencies and model the invariant mass distributions. In the simulation, pp collisions are generated using PYTHIA [82, 93] with a specific LHCb configuration [83]. Decays of hadronic particles are described by EVTGEN [94], in which final-state radiation is generated using PHOTOS [95]. The interaction of the generated particles with the detector, and its response, are implemented using the GEANT4 toolkit [84, 96] as described in Ref. [97].

In the interest of resource optimisation simulated candidates are generated only in a given geometrical region and can include generator level cuts—events are rejected at generator level, saving the detector response emulation and the rest of the processing chain. Different topological requirements and generator level cuts are included in the samples used for this analysis. Moreover, in order to minimize the effect of possible detector asymmetries the samples contain equal proportions of events for which the detector response was emulated in the positive (Magnet Up) and negative (Magnet Down) magnetic field configurations. Table 6.1 gathers all the simulation samples employed for this analysis and their properties.
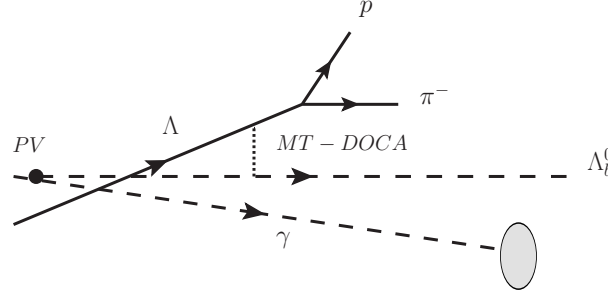
Figure 6.1: Sketch of the $\Lambda_b^0 \to \Lambda\gamma$ decay topology with graphical representation of the MT-DOCA variable. See text for its definition.

6.3 Candidate reconstruction and selection

6.3.1 Candidate reconstruction

The reconstruction of $\Lambda_b^0 \to \Lambda\gamma$ is very challenging at LHCb due to the combination of a long lived particle, which mostly decays outside the VELO, and a photon, for which the direction can not be measured. The absence of a reconstructed secondary vertex (SV), used in most LHCb analysis, requires a dedicated strategy, which is common between the High Level Trigger (HLT) and the offline reconstruction. Λ candidates are built from the combination of two long tracks that are compatible with the p and π hypotheses and originate from a common vertex. The γ is reconstructed as a calorimeter cluster with no track pointing to it. The direction of the photon can not be directly measured with the LHCb calorimeters and thus it is assumed to come from the origin of the LHCb reference frame—close to the interaction point. As a consequence it is not possible to reconstruct the decay vertex of the Λ_b^0. Instead its momentum is obtained as the direct sum of the Λ and γ momenta.

The particular topology of this mode and the missing information on the Λ_b^0 decay vertex make its study a demanding task. Still, LHCb is the only ongoing experiment that has access to this mode and its proven physics interest motivates the development of special techniques to study it. In this analysis the distance of closest approach between the reconstructed Λ direction and its mother trajectory (MT-DOCA) is exploited in order to reject combinatorial background, where the mother trajectory is defined by the Λ_b^0 momentum and the PV position. This technique was previously introduced in Ref. [98]. A sketch of the decay topology including a graphical representation of this variable is shown in Fig. 6.1.

The same reconstruction strategy, that is, the construction of the candidate as a sum of 4-momenta, is applied to the normalisation and control modes in the offline processing, although the SV could be reconstructed in this case. This is done in order to reduce the differences between the modes in the interest of systematic uncertainty minimisation. Some inevitable differences arise at trigger level, as detailed in the following section.

6.3.2 Trigger selection

For this analysis a common trigger strategy is used for the signal and normalisation modes at the L0 and HLT1 stages. A dedicated HLT2 reconstruction and selection is used for $\Lambda_b^0 \to \Lambda\gamma$ while $B^0 \to K^{*0}\gamma$ candidates are selected through the inclusive radiative trigger presented in Chapter 4.

At L0 radiative decays are selected exploiting the particular signature of a high energy cluster in the electromagnetic calorimeter. Clusters with no hit in the associated SPD cell are selected by the L0Photon

Table 6.2: Requirements included in the `Hlt2RadiativeLb2L0GammaLL` selection.

Variable	Units	Requirement
Track p	MeV	> 2000
Track p_T	MeV	> 250
Track IP χ^2		> 36
Track χ^2		< 3
p DLLp		> 0
Tracks DOCA	mm	< 0.2
γ p	MeV	> 5000
γ p_T	MeV	> 2000
Λ p_T	MeV	> 1500
Λ IP	mm	> 0.1
Λ Vertex χ^2		< 15
Λ FD χ^2		> 0
Λ τ	ps	> 2
Λ ΔM	MeV	< 20
γ p_T + Λ p_T	MeV	> 5000
Λ^0_b MTDOCA χ^2		< 9
Λ^0_b p_T	MeV	> 1000
Λ^0_b ΔM	MeV	< 1000

requirement while those with hits are selected by `L0Electron`. Due to the significant conversion of photons into electrons in the SPD detector, events selected by any of these two conditions are used. Moreover the candidate photon is required to be the one responsible for firing the L0, *i.e.*, the TOS condition is applied on either `L0Photon` or `L0Electron`.

The HLT1 selection relies on the large transverse momentum of the final state tracks and their displacement with respect to the collision point, the typical signature of b-hadron decays. The `Hlt1TrackMVA` trigger combines these two properties of a single track in a multi-variate selection that is able to provide a large signal efficiency to background rejection ratio. Also at this level the TOS condition is employed to ensure the tracks forming the Λ candidate are the ones satisfying the HLT1 requirements.

At HLT2 a dedicated selection named `Hlt2RadiativeLb2L0GammaLL` is employed for the signal. The candidate is reconstructed following the strategy presented in the previous section and the simple selection presented in Table 6.2 is applied in order to keep the rate under control.

No HLT2 line building the candidate as a sum of momenta, as is done for the signal, is available for $B^0 \to K^{*0}\gamma$. Instead the inclusive selection described in detail in Sec. 4.2, which exploits the common properties of radiative b-decays is used. In order to minimise systematic uncertainties that can arise from the utilisation of different selections for the signal and control modes at trigger level, equivalent requirements to the ones of the $\Lambda^0_b \to \Lambda\gamma$ dedicated trigger are applied offline to $B^0 \to K^{*0}\gamma$. In this way most systematic effects on the trigger selection are expected to cancel in the ratio of both modes. The efficiency of the inclusive trigger used only for $B^0 \to K^{*0}\gamma$ can be studied on data thanks to the large yield of this mode and should not represent a large source of systematic uncertainty either.

6.3.3 Offline selection

The offline reconstruction of the candidates follows the strategy used in the trigger. The events are first filtered by the stripping configuration presented in Table 6.3, which retains more than $25 \cdot 10^6$ candidates. The offline selection relies on a preselection based on linear cuts followed by a multivariate (MVA) selection trained to reject the overwhelming combinatorial background.

Table 6.3: Stripping requirements applied on $\Lambda_b^0 \to \Lambda\gamma$ candidates.

Variable	Units	Requirement
Track IP χ^2		> 9
Max track χ^2		< 3
Min track χ^2		< 2
Track Ghost Prob		< 0.4
p p	MeV	> 7000
p p_{T}	MeV	> 800
π p	MeV	> 2000
π p_{T}	MeV	> 300
Tracks DOCA χ^2		< 30
γ CL	MeV	> 0.2
γ p_{T}	MeV	> 2500
Λ p_{T}	MeV	> 1000
Λ IP	mm	> 0.05
Λ IP χ^2		> 16
Λ Vertex χ^2		< 9
Λ ΔM	MeV	< 20
γ p_{T} + Λ p_{T}	MeV	>5000
Λ_b^0 MTDOCA χ^2		< 7
Λ_b^0 p_{T}	MeV	>1000
Λ_b^0 ΔM	MeV	< 1100

The preselection, designed to reduce the data sample size while retaining as much signal as possible, is defined by directly comparing the signal and background distributions of relevant variables. For this, the simulated sample described in Sec. 6.2 is used with the reconstructed candidates matched to the generated ones and filtered by the trigger and stripping requirements. The background sample is formed by data candidates selected by the stripping and trigger whose invariant mass lies below 5100 MeV or above 6100 MeV. These regions are referred to as low- and high-mass side-bands in the following, while the central interval is defined as the signal region.

The comparison of the signal and background distributions from the samples described above is shown in Figs. 6.2 and 6.3 and the full preselection is listed in Table 6.4. Kinematic and track quality requirements are applied in order to reduce the large amount of background without a significant lost of signal. Moreover only Λ that decay in the dense part of the VELO are selected by requiring the Z coordinate or the first hit associated to the pion track to be detected before 270 mm. Furthermore, one can notice from the $p\pi^-$ invariant mass distribution in the background sample that almost all the background comes from true Λ. As a consequence only soft particle identification requirements are imposed. The corresponding selection is applied on the normalisation mode.

6.3.4   Data and simulation agreement

The optimisation of the selection described in the this section fully relies on simulation. In particular, the BDT is trained using MC as proxy for the signal. Moreover, the efficiency of the selection is also obtained mostly from simulated samples, as detailed in Sec 6.4.3. Thus the accuracy of the results depends on the proper description of the signal properties in the MC. Three high rate modes for which the yield in data is abundant are used to cross-check the simulation distributions for different parts of the decay chain: Λ_b^0 properties are validated in $\Lambda_b^0 \to pK^-J/\psi$ decays since they should not depend on the particular decay mode; Λ, p and $\pi^\pm$ distributions in MC are compared to data using $\Lambda_b^0 \to \Lambda J/\psi$ candidates and γ

Table 6.4: Preselection requirements applied on $\Lambda_b^0 \to \Lambda\gamma$ candidates.

Variable	Units	Requirement
Max track Ghost Prob		< 0.2
Track p	GeV	$\in (3, 100)$
$\pi^\pm$ first hit Z	mm	< 270
p ProbNNp		> 0.2
π ProbNNpi		> 0.2
γ p_T	MeV	> 3000
Λ IP	mm	> 0.15
Λ IP χ^2		> 16
Λ FD χ^2		> 225
Λ M	MeV	$\in (1110, 1122)$
Λ_b^0 MTDOCA	mm	< 0.05
Λ_b^0 MTDOCA χ^2		< 5
Λ_b^0 p_T	MeV	> 4000
Λ_b^0 ΔM	MeV	< 1000

Figure 6.2: MC (black) and data side-band (red) track distributions for candidates satisfying the trigger and stripping requirements.

properties are studied in $B^0 \to K^{*0}\gamma$ events. These decays are referred to as control modes.

In order to obtain pure samples of these decays, selections are applied to the full 2016 dataset following previous studies of these modes at LHCb. In particular, $\Lambda_b^0 \to pK^-J/\psi$, $\Lambda_b^0 \to \Lambda J/\psi$ and $B^0 \to K^{*0}\gamma$ candidates are filtered following the selections developed in Refs. [99], [52] and [42], respectively. The same criteria are applied to the simulation samples in 2016 conditions described in Sec. 6.2. The *sPlot*
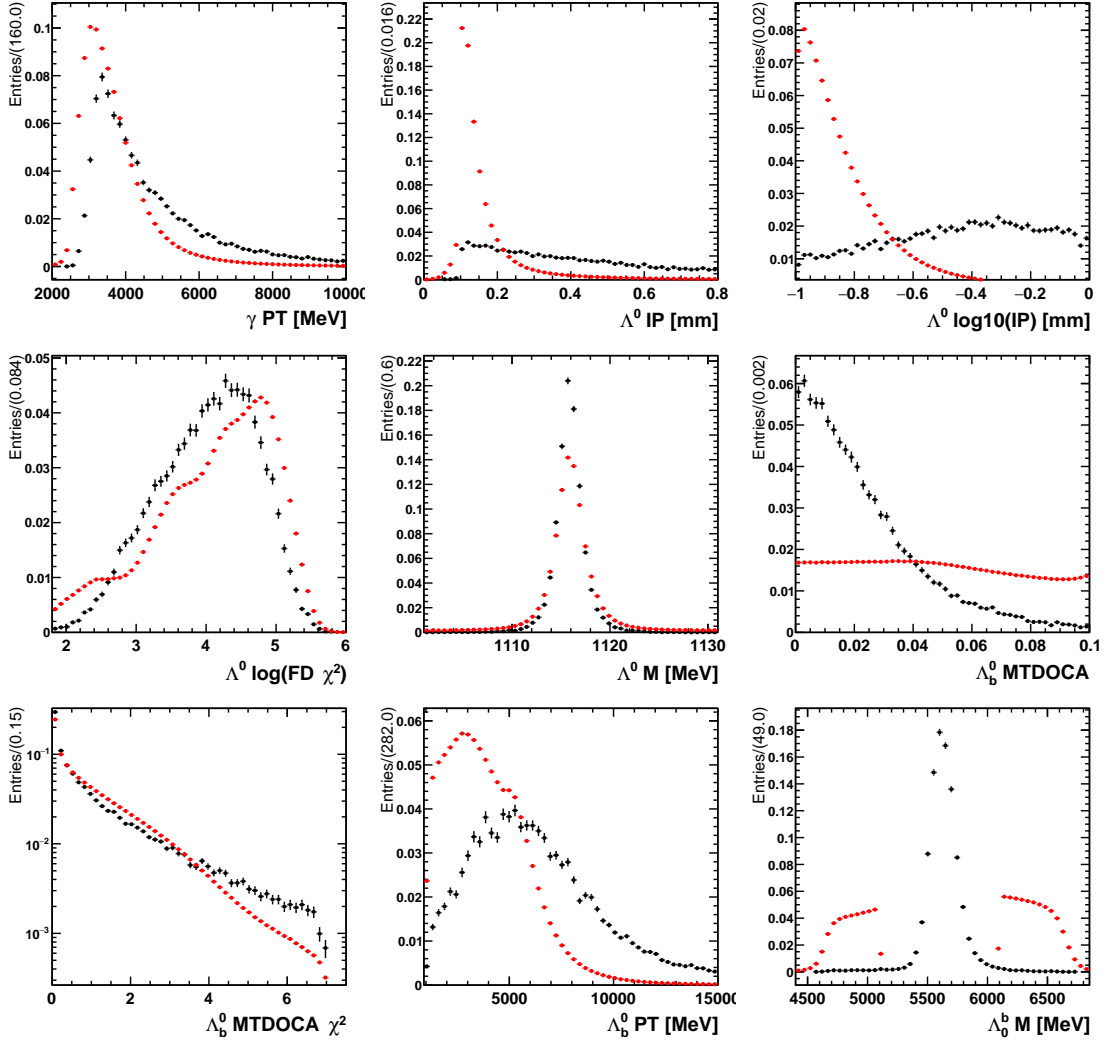
Figure 6.3: MC (black) and data side-band (red) photon, Λ and Λ^0_b distributions for candidates satisfying the trigger and stripping requirements.

technique [100] is employed to unfold the signal distributions of the variables of interest in data. All modes are fitted with a double-tail Crystal-Ball, defined in Eq. 6.17, accounting for the signal contribution and an exponential function describing the combinatorial background. The results of the fits are shown in Fig. 6.4. The signal distributions in data compared to the simulated ones are presented in Fig. 6.5, 6.6 and 6.7 for the Λ^0_b from $\Lambda^0_b \to pK^-J/\psi$, the Λ, p and $\pi^\pm$ from and $\Lambda^0_b \to \Lambda J/\psi$ and the γ from $B^0 \to K^{*0}\gamma$, respectively.

Large discrepancies are observed in the description of Λ^0_b $p_{\rm T}$, so they should be corrected in the simulation. Smaller deviations are present also for all the baryonic (Λ and p) $p_{\rm T}$ distributions. The latter probably arise from the inaccurate reproduction of the properties of the parent particle, so as a first step corrections are obtained as the binned ratio between the MC and the s-weighted $\Lambda^0_b \to pK^-J/\psi$ distributions. Since the Λ^0_b $p_{\rm T}$ is correlated with the Λ^0_b p, for which small discrepancies are also present, the corrections are obtained as the ratio of the 2-dimensional p-$p_{\rm T}$ distributions, as shown in Fig. 6.8. The corrections are applied to simulation as a per-event weight extracted from the (Λ^0_b p, Λ^0_b $p_{\rm T}$) bin corresponding to the candidate. The MC-corrected distributions are shown as green triangles in Fig 6.5
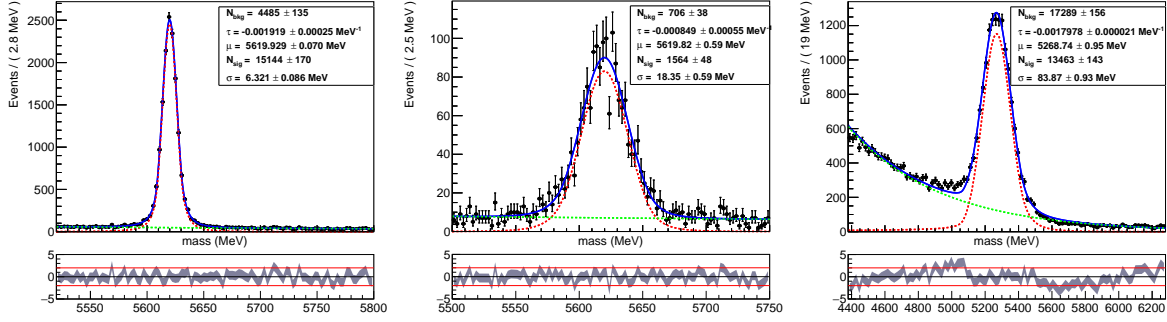
Figure 6.4: $\Lambda_b^0 \to pK^- J/\psi$ (left), $\Lambda_b^0 \to \Lambda J/\psi$ (middle) and $B^0 \to K^{*0}\gamma$ (right) candidates in the 2016 data sample (black dots). The result of an unbinned maximum likelihood fit is overlaid (blue solid curve) with the signal (red dashed line) and combinatorial background (green dashed line) contributions. The values of the fit parameters as obtained from the fit are presented in the box.
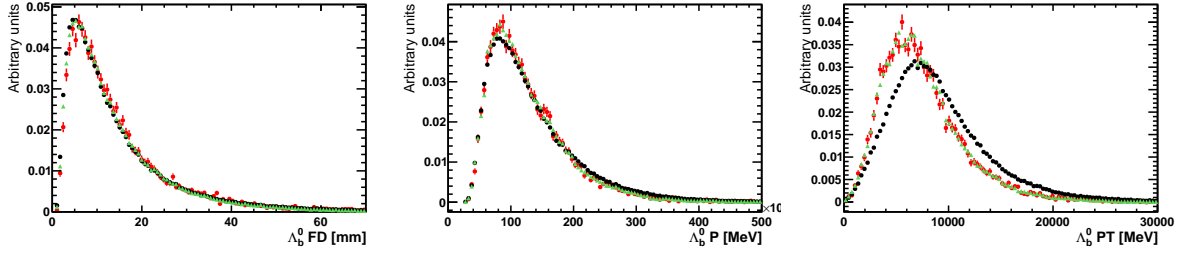

Figure 6.5: Λ_b^0 distributions from $\Lambda_b^0 \to pK^- J/\psi$ s-weighted data candidates (red dots), MC (black dots) and MC corrected candidates (green triangles).

and 6.6 for the Λ_b^0 from $\Lambda_b^0 \to pK^- J/\psi$ and the Λ, p and $\pi^{\pm}$ properties from $\Lambda_b^0 \to \Lambda J/\psi$, respectively. All the MC p and p_{T} distributions are in much better agreement with the background subtracted data after the correction. Other variables are well reproduced by the simulation, taking into account the statistical uncertainties. Thus no other corrections are applied.

The (Λ_b^0 p, Λ_b^0 p_{T}) corrections are applied to the $\Lambda_b^0 \to \Lambda\gamma$ MC sample used in the training of the BDT described in the following and we shall also take them into account in the calculation of selection efficiencies.

6.3.5 Multivariate selection

After the preselection, a Boosted Decision Tree (BDT) [74] is exploited to further separate signal from combinatorial background. The `scikit-learn` [101] library is used to implement this discriminant and the XGBoost algorithm [102, 103] is chosen for the boosting. The BDT is trained on reweighted simulated data as proxy for the signal and the data in the high side-band region as background.

The BDT input variables and algorithm parameters are chosen as a compromise between performance and complexity. Table 6.5 lists the fifteen variables used as input and their distributions in the signal and background samples are shown in Figs. 6.9 and 6.10. The variables providing largest discrimination power are the transverse momentum of the pion, the photon, the Λ and the Λ_b^0 and the sum of the transverse momenta of the tracks and the photon, the impact parameter of the pion and the Λ with respect to the PV, the IP χ^2 —defined as the difference in the vertex fit χ^2 when including or not the particle in the fit— of the p and the Λ, the distance of closest approach between the two tracks, the flight distance of the Λ, the MT-DOCA defined in Sec. 6.3.1 and asymmetry measures in a cone of 1 cm around the Λ
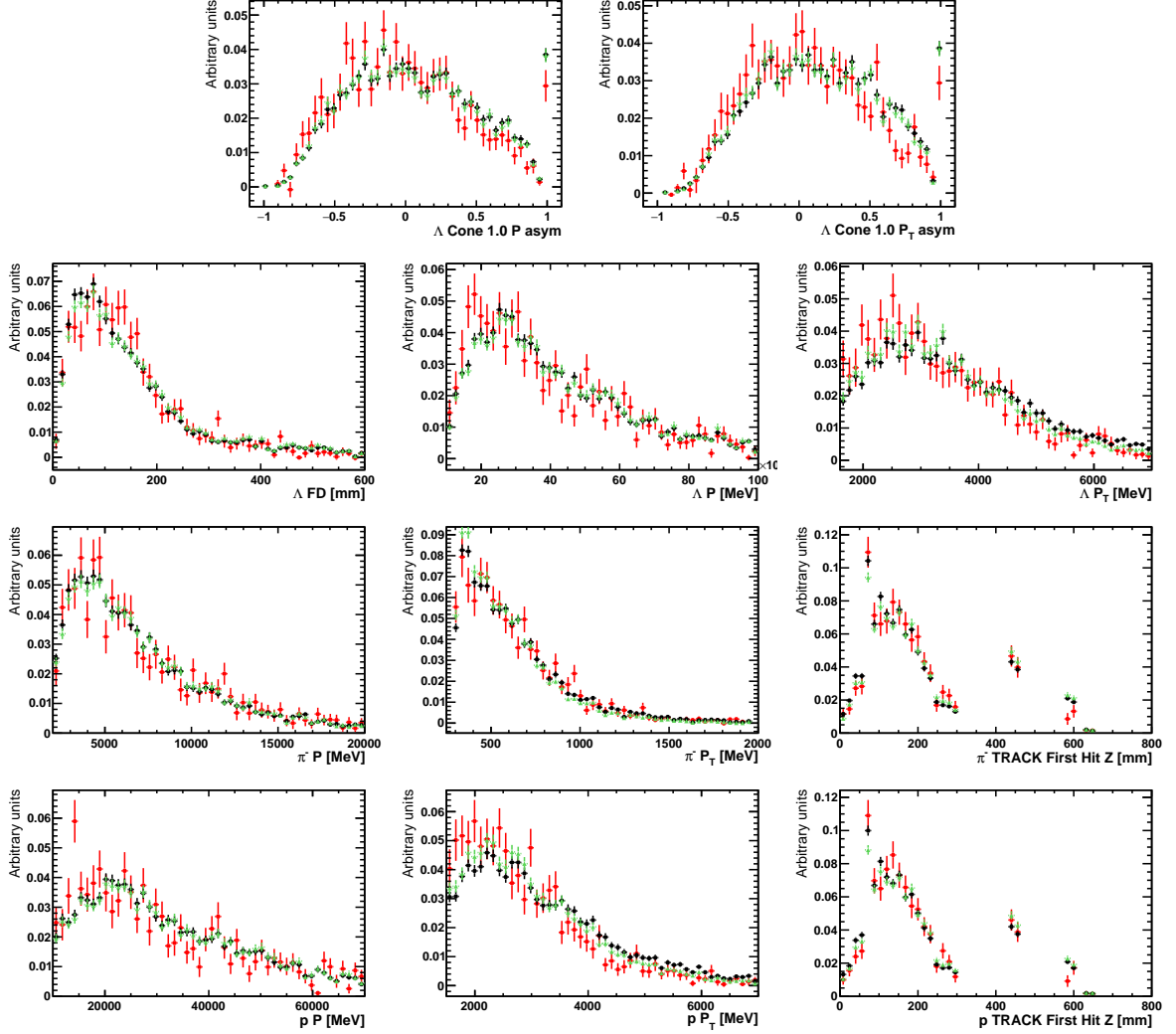
Figure 6.6: Λ, p and $\pi^{\pm}$ distributions from $\Lambda_b^0 \to \Lambda J/\psi$ s-weighted data candidates (red dots), MC (black dots) and MC corrected candidates (green triangles).

and the photon. In particular the momentum and transverse momentum asymmetry in the cone around the Λ and the transverse momentum asymmetry in the one around the photon are included, where the transverse momentum asymmetry in the cone around the Λ is defined as:

$$\mathcal{A}(p_{\mathrm{T}}) = \frac{p_{\mathrm{T}\Lambda} - p_{\mathrm{T}cone}}{p_{\mathrm{T}\Lambda} + p_{\mathrm{T}cone}} \tag{6.1}$$

and respectively for the other variables. The best algorithm configuration uses 200 trees with a maximum depth of 3 layers and a learning rate[1] of 0.3.

The BDT is trained and applied using a two-fold technique: the full sample is divided in two halves, A and B, which are split in 3 parts each; two of them are used to train a BDT and the remaining one to test its performance; finally, the BDT trained on half A is applied to B and vice-versa. This is done

---

[1]The depth of the tree controls the number of subsequent separation cuts than can be applied in a single boost while the learning rate controls how fast the per-event weight can change in consecutive tree trainings.
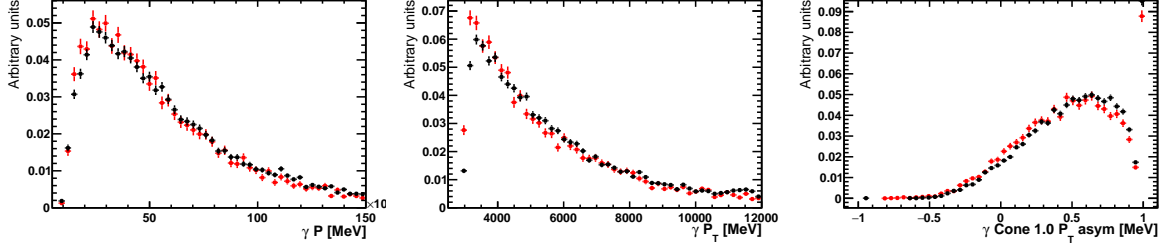
Figure 6.7: γ distributions from $B^0 \to K^{*0}\gamma$ s-weighted data candidates (red dots) and MC (black dots).
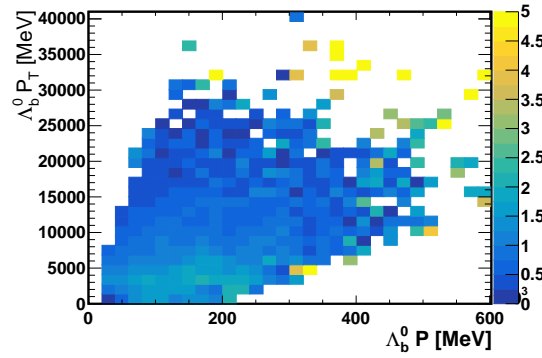

Figure 6.8: MC corrections in 2-dimensional bins of p and p_T obtained from the ratio of MC and s-weighted $\Lambda_b^0 \to pK^- J/\psi$ data.

in order to avoid overtraining, which occurs when a BDT learns the particular fluctuations of the data used for training instead of the global patterns. The overtraining is checked by comparing the output

Table 6.5: Input variables to the BDT separating $\Lambda_b^0 \to \Lambda\gamma$ candidates from combinatorial background.

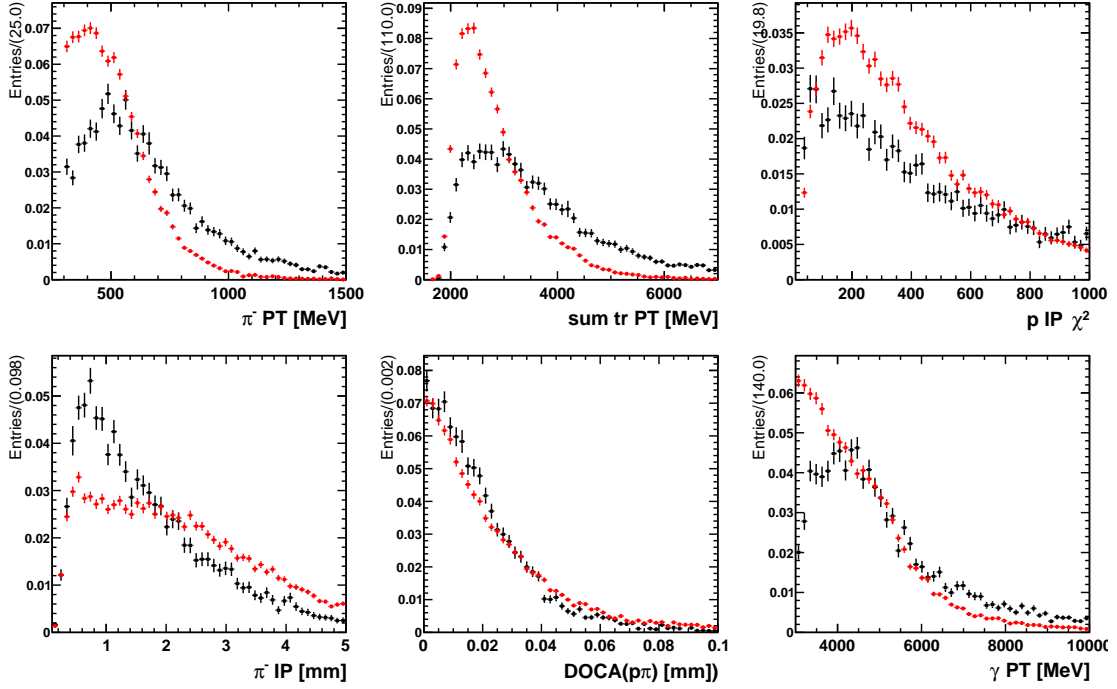| Variables |
| :---: |
| $\pi^\pm \ p_\mathrm{T}$ |
| $p \ p_\mathrm{T} + \pi^\pm \ p_\mathrm{T} + \gamma \ p_\mathrm{T}$ |
| $p \ \mathrm{IP} \ \chi^2$ |
| $\pi^\pm \ \mathrm{IP}$ |
| Tracks DOCA |
| $\gamma \ p_\mathrm{T}$ |
| $\Lambda \ p_\mathrm{T}$ |
| $\Lambda \ \mathrm{IP}$ |
| $\Lambda \ \mathrm{IP} \ \chi^2$ |
| $\Lambda \ \mathrm{FD}$ |
| $\Lambda_b^0 \ p_\mathrm{T}$ |
| $\Lambda_b^0 \ \mathrm{MTDOCA}$ |
| $\Lambda \ \mathrm{Cone}(1.0) \ \mathcal{A}_p$ |
| $\Lambda \ \mathrm{Cone}(1.0) \ \mathcal{A}_{p_\mathrm{T}}$ |
| $\gamma \ \mathrm{Cone}(1.0) \ \mathcal{A}_{p_\mathrm{T}}$ |

Figure 6.9: MC (black) and high-mass data side-band (red) track and photon distributions used as input for the BDT.

distribution of the BDT in the training and the test samples, as shown in Fig. 6.11. Although it is found to be small, applying each BDT to the other half of the data, which has not been used neither for training nor for testing, ensures no bias will be introduced when computing the efficiency of a particular condition on the output distribution.

As a cross-check, the average BDT output value in bins of invariant mass is shown in Fig. 6.12 for the signal and background samples in half A. The distributions are perfectly flat ensuring the BDT cannot cause artificial peaks in the signal region.

The requirement on the output BDT distribution is optimised by maximising the Punzi figure of merit (FoM) [104], defined as:

$$FoM = \frac{\epsilon_S}{\sqrt{\sigma + N_B}} \tag{6.2}$$

where ϵ_S is the efficiency of the selection on the signal sample, N_B the expected background yield in the signal region and $\sigma = 5$ the target statistical significance. N_B is obtained from the extrapolation of the observed background yield in the high-mass side-band at each point to the signal region. An exponential probability density function (PDF) obtained from a fit to the initial high-mass side-band distribution is used for the extrapolation. Since the BDT is not correlated with the mass this shape is constant for different requirements on the BDT output distribution. Figure 6.13 shows the evolution of the Punzi FoM with the minimum value required on the BDT output for half A (left) and B (right). A working point of 0.985 is chosen, which provides a signal efficiency of 33% with a 99.8% background rejection.

A separate BDT with the same configuration and input variables is used to select $B^0 \to K^{*0}\gamma$ events. It is trained using $B^0 \to K^{*0}\gamma$ MC as signal and events on the high side-band of the B^0 invariant mass distribution as background. The same two fold technique is followed. In this case the requirement on the BDT output is optimised using the signal significance as FoM:
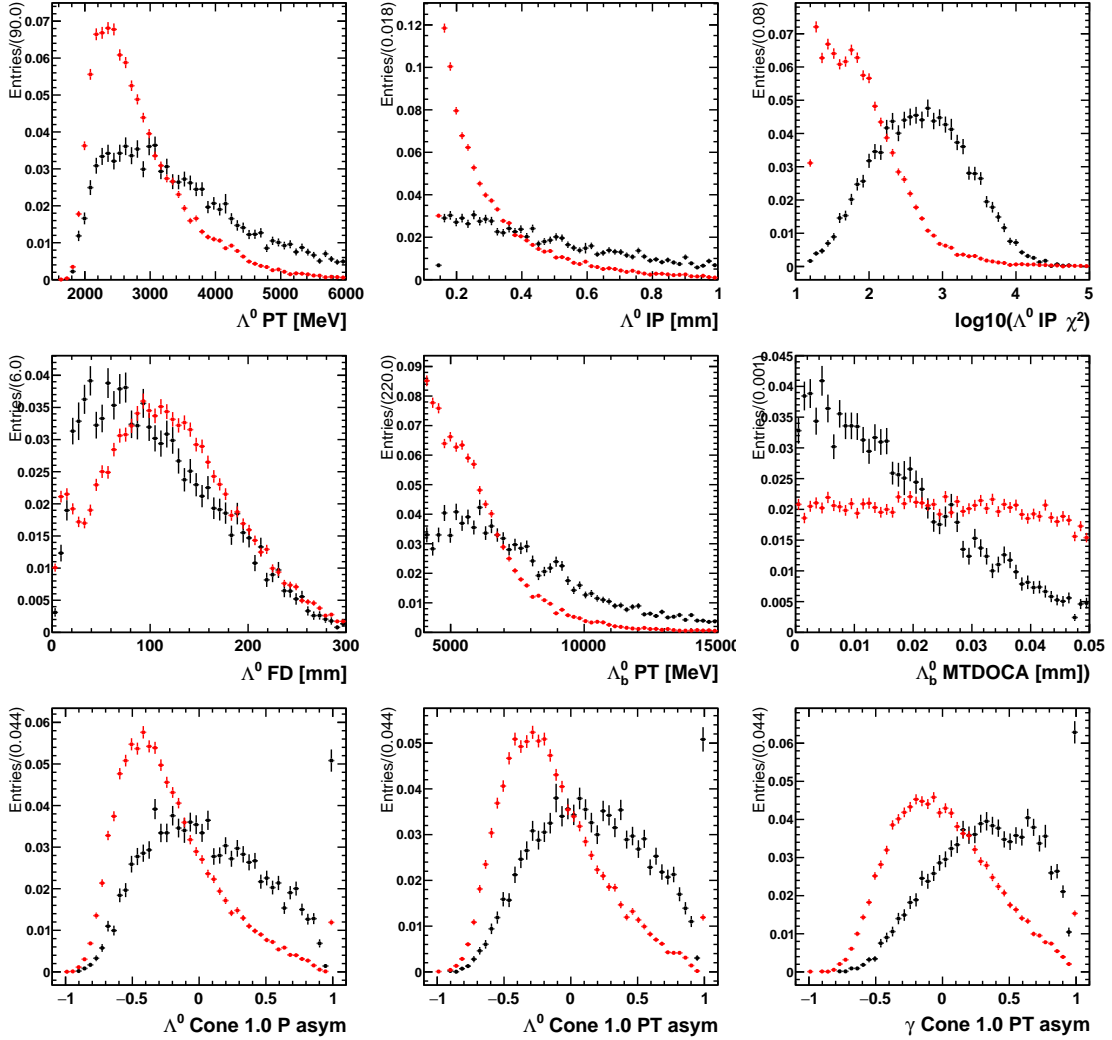
$$FoM = \frac{N_S}{\sqrt{N_S + N_B}} \tag{6.3}$$

Figure 6.10: MC (black) and high-mass data side-band (red) Λ and Λ_b^0 and cone asymmetry distributions used as input for the BDT.

where N_S is the expected signal yield obtained from the signal efficiency and the known $B^0 \to K^{*0}\gamma$ branching fraction, $\mathcal{B}(B^0 \to K^{*0}\gamma) = (4.33 \pm 0.15) \cdot 10^{-5}$ [51].

A final requirement is applied after the BDT selection. A source of possible physical background for both $\Lambda_b^0 \to \Lambda\gamma$ and $B^0 \to K^{*0}\gamma$ is that coming from the misidentification of the photon for a π^0. To reject this contribution the neutral particle identification variables are exploited. These use information from the calorimeter cluster shape and energy to build a discriminant between different types of neutral objects. In particular the variable `IsPhoton` is the output of an MVA trained to separate π^0 and γ [66]. For this analysis a requirement on `IsPhoton` > 0.6 is applied to both the signal and the normalisation modes, which rejects around 35% of the background while keeping 98% of the signal.
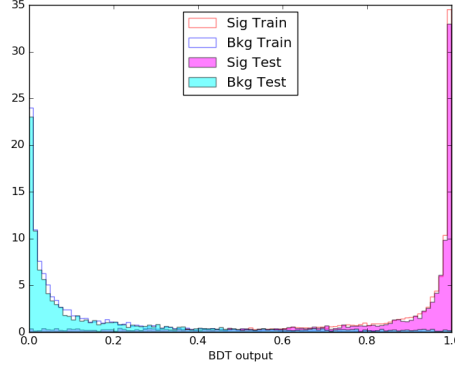
Figure 6.11: BDT output distribution for signal (pink) and background (blue) in the training (empty) and test (full histogram) samples of half A.
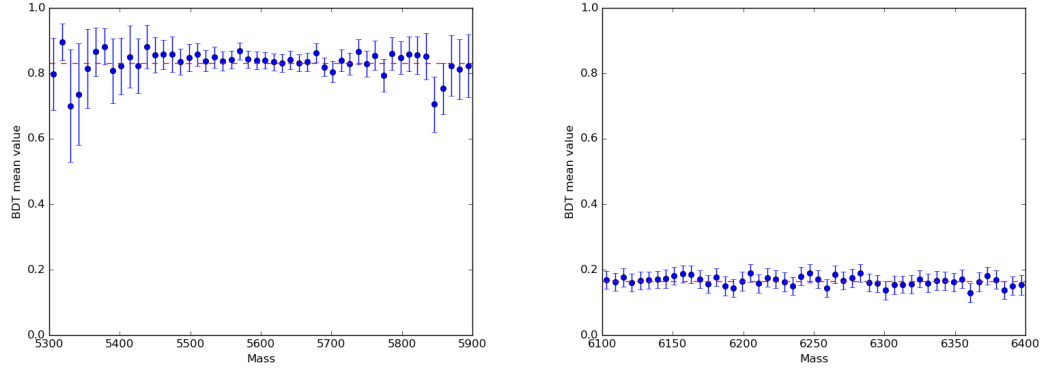

Figure 6.12: Mean BDT output value in bins of invariant mass for signal (left) and background (right) candidates of half A.

6.4 Extraction of the branching ratio

The branching ratio of the $\Lambda_b^0 \to \Lambda\gamma$ decay is directly proportional to the signal yield observed in data:

$$N(\Lambda_b^0 \to \Lambda\gamma) = \mathcal{L} \cdot 2\sigma_{b\bar{b}} \cdot f_{\Lambda_b^0} \cdot \mathcal{B}(\Lambda_b^0 \to \Lambda\gamma) \cdot \mathcal{B}(\Lambda \to p\pi^-) \cdot \epsilon_{sel}(\Lambda_b^0 \to \Lambda\gamma) \tag{6.4}$$

where $\mathcal{L}$ is the integrated luminosity corresponding to the analysed dataset, $\sigma_{b\bar{b}}$ is the $b\bar{b}$ production cross-section, $f_{\Lambda_b^0}$ is the probability that a b hadronizes into a Λ_b^0, known as hadronization fraction, and $\epsilon_{sel}(\Lambda_b^0 \to \Lambda\gamma)$ is the efficiency selecting the decay mode. In order to avoid uncertainties coming from the measurement of $\mathcal{L}$ and $\sigma_{b\bar{b}}$ the well-known $B^0 \to K^{*0}\gamma$ decay is used as normalisation mode. An equivalent expression to that of Eq. 6.4 can be written for this decay and taking the ratio one obtains:

$$\frac{N(\Lambda_b^0 \to \Lambda\gamma)}{N(B^0 \to K^{*0}\gamma)} = \frac{f_{\Lambda_b^0}}{f_{B^0}} \cdot \frac{\mathcal{B}(\Lambda_b^0 \to \Lambda\gamma)}{\mathcal{B}(B^0 \to K^{*0}\gamma)} \cdot \frac{\mathcal{B}(\Lambda \to p\pi^-)}{\mathcal{B}(K^{*0} \to K^+\pi^-)} \cdot \frac{\epsilon_{sel}(\Lambda_b^0 \to \Lambda\gamma)}{\epsilon_{sel}(B^0 \to K^{*0}\gamma)} \tag{6.5}$$

which does not depend on $\mathcal{L}$ and $\sigma_{b\bar{b}}$ anymore. The particular normalisation mode is chosen in order to cancel as much as possible systematic uncertainties related to the photon selection, which cannot be controlled by means of other control channels. A more advantageous normalisation mode for $\Lambda_b^0 \to \Lambda\gamma$
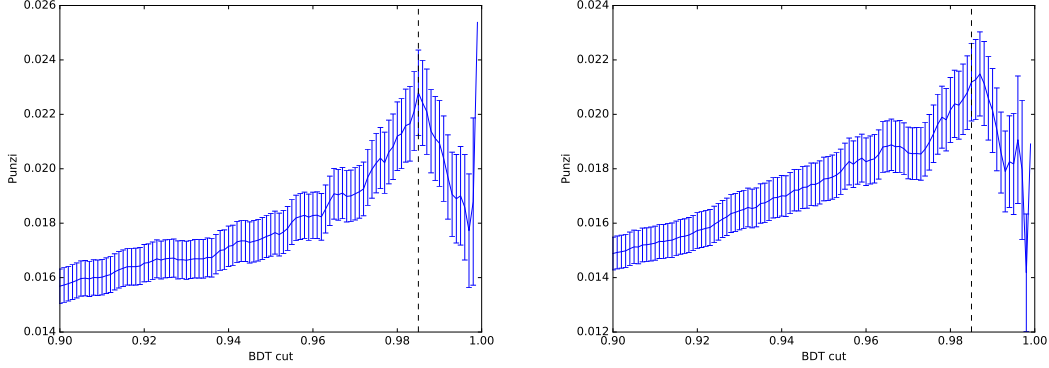
Figure 6.13: Punzi FoM as a function of the required value on the BDT output for half A (left) and B (right).

would be one involving a radiative baryon decay, for which also the hadronization fraction would cancel and the kinematics of the hadronic part of the decay would be more similar. Although the baryonic $\Lambda_b^0 \to \Lambda^*\gamma$ has been studied at LHCb [105], no precise measurement of its branching ratio is available yet and thus cannot be used as normalisation. A further reduction in systematic uncertainties could be achieved when this becomes available. Other normalisation stategies will also be discussed in Sec. 6.8.

The event yields entering in Eq. 6.5 can be obtained from a fit to the invariant mass distribution of the selected candidates. For simplification, the $\mathcal{B}(\Lambda_b^0 \to \Lambda\gamma)$ is directly used as a fit parameter. To do this, the signal yield is re-written as:

$$N(\Lambda_b^0 \to \Lambda\gamma) = \alpha \cdot \mathcal{B}(\Lambda_b^0 \to \Lambda\gamma) \cdot N(B^0 \to K^{*0}\gamma) \tag{6.6}$$

where both $\mathcal{B}(\Lambda_b^0 \to \Lambda\gamma)$ and $N(B^0 \to K^{*0}\gamma)$ are free parameters of the fit. We refer to α as the normalisation constant, which is given by:

$$\alpha = \frac{f_{\Lambda_b^0}}{f_{B^0}} \cdot \frac{1}{\mathcal{B}(B^0 \to K^{*0}\gamma)} \cdot \frac{\mathcal{B}(\Lambda \to p\pi^-)}{\mathcal{B}(K^{*0} \to K^+\pi^-)} \cdot \frac{\epsilon_{sel}(\Lambda_b^0 \to \Lambda\gamma)}{\epsilon_{sel}(B^0 \to K^{*0}\gamma)} \tag{6.7}$$

This parameter is fixed in the fit to the value obtained in the coming sections.

6.4.1 Hadronisation fractions

The ratio of hadronisation fractions $f_{\Lambda_b^0}/f_{B^0}$ has been observed to depend on the Λ_b^0 transverse momentum. More specifically this dependency has been studied by LHCb in pp collisions at a centre of mass energy of 7 TeV and it has been parametrized by an exponential function [106]:

$$f_{\Lambda_b^0}/f_{B^0}(p_T) = a + \exp(b + c \times p_T[\text{GeV}]) \tag{6.8}$$

with

$$a = +0.151 \pm 0.016 \, ^{+0.024}_{-0.025}$$
$$b = -0.573 \pm 0.040 \, ^{+0.101}_{-0.097}$$
$$c = -0.095 \pm 0.007 \pm 0.014 \, [\text{GeV}^{-1}]$$

The correlations among a, b and c are facilitated in Ref. [106] and we shall use them in our calculations.

In order to obtain the average ratio of hadronisation fractions in the LHCb acceptance, the generated Λ_b^0 p_T distribution in MC, shown in Fig. 6.14, is exploited. The weights obtained in Sec. 6.3.4 to correct the reconstructed distributions in MC are not used in the nominal calculation since they are not guaranteed
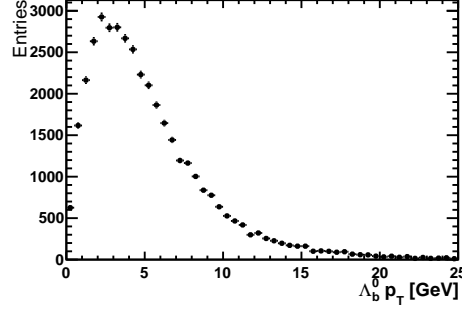
Figure 6.14: Generated Λ_b^0 p_{T} distribution in the LHCb acceptance.

Table 6.6: Values of the branching fractions entering in Eq. 6.7 from Ref. [51].

Decay	Branching fraction
$B^0 \to K^{*0}\gamma$	$(4.33 \pm 0.15) \times 10^{-5}$
$\Lambda \to p\pi^-$	(63.9 ± 0.5) %
$K^{*0} \to K^+\pi^-$	(99.754 ± 0.021) %

to work properly for the generated MC distribution, which is free from resolution effects. Their impact is assessed in Sec. 6.6 and the difference assigned as systematic.

The ratio of hadronisation fractions is calculated for each event using Eq. 6.8 and the average is computed:

$$f_{\Lambda_b^0}/f_{B^0}(p_{\mathrm{T}}-\mathrm{av}) \quad = \quad 0.493 \pm 0.055$$

where the uncertainty comes from the propagation of the parameter uncertainties taking into account the correlations. The effect of the finite size of the simulation sample is negligible and is thus not considered.

The extraction of the average $f_{\Lambda_b^0}/f_{B^0}$ from the results in Ref. [106] assumes that the dependency observed in pp collisions at 7 TeV holds at 13 TeV. This hypothesis should be cross-checked when this observable is studied at the latter energy. We take into account this shortcoming when presenting the results in Sec. 6.7.

6.4.2 Input branching ratios

The branching fractions of the normalisation mode and the intermediate decays are taken from Ref. [51] and listed in Table 6.6. From these values the inverse of the $\mathcal{B}(B^0 \to K^{*0}\gamma)$ and the ratio of intermediate state branching fractions are extracted:

$$\frac{1}{\mathcal{B}(B^0 \to K^{*0}\gamma)} = (2.31 \pm 0.08) \times 10^4 \qquad \frac{\mathcal{B}(\Lambda \to p\pi^-)}{\mathcal{B}(K^{*0} \to K^+\pi^-)} = 0.641 \pm 0.005 \qquad (6.9)$$

6.4.3 Selection efficiencies

The efficiency of selecting a given decay can be divided in smaller pieces related to the different steps of the reconstruction and selection:

$$\epsilon^{sel} = \epsilon^{gen.lev.cuts} \cdot \epsilon^{reco,strip} \cdot \epsilon^{presel} \cdot \epsilon^{trPID} \cdot \epsilon^{BDT} \cdot \epsilon^{\gamma PID} \cdot \epsilon^{trigger} \qquad (6.10)$$

Table 6.7: Number of generated events in the full MC samples, efficiencies of the topological and acceptance requirements and effective number of signal events generated with the parent particle inside the LHCb acceptance for the $\Lambda_b^0 \to \Lambda\gamma$ and $B^0 \to K^{*0}\gamma$ samples split by magnet polarity.

| | $\Lambda_b^0 \to \Lambda\gamma$ | | $B^0 \to K^{*0}\gamma$ | |
	Magnet Up	Magnet Down	Magnet Up	Magnet Down
N^{topo}	18.6×10^6	18.4×10^6	1.9×10^6	1.8×10^6
ϵ^{topo} [%]	50.19 ± 0.14	50.04 ± 0.14	25.006 ± 0.079	24.968 ± 0.080
ϵ^{acc} [%]	33.47 ± 0.19		33.36 ± 0.22	
N^{acc} [10^6]	12.405 ± 0.078	12.306 ± 0.078	2.59 ± 0.28	2.80 ± 0.31

where each term can be expressed as the ratio between the number of signal candidates in the previous step and the amount selected by the current requirement, i.e.:

$$\epsilon^{sel} = \frac{N^{gen.lev.cuts}}{N^{acc}} \cdot \frac{N^{reco,strip}}{N^{gen.lev.cuts}} \cdot \frac{N^{presel}}{N^{reco,strip}} \cdot \frac{N^{trPID}}{N^{presel}} \cdot \frac{N^{BDT}}{N^{trPID}} \cdot \frac{N^{\gamma PID}}{N^{BDT}} \cdot \frac{N^{trigger}}{N^{\gamma PID}} \qquad (6.11)$$

Each term is discussed in detail and obtained in the following for both $\Lambda_b^0 \to \Lambda\gamma$ and $B^0 \to K^{*0}\gamma$. The weights obtained in Section 6.3.4 to correct the Λ_b^0 p-p_T spectra are taken into account whenever relevant.

Acceptance considerations

Since the ratio of hadronisation fractions has been obtained inside the LHCb acceptance, we should compute the selection efficiency with respect to events where the parent Λ_b^0 or B^0 has been produced already in this acceptance. However, the MC samples simulating these decays have been generated with different topological cuts, as summarised in Table 6.1, so this effect should be accounted for.

On one hand, the $\Lambda_b^0 \to \Lambda\gamma$ sample used throughout the analysis is produced with the single requirement that the Λ_b^0 momentum in the Z direction —parallel to the beam pipe— is positive, *i.e.*, the particle moves in the forward direction. We refer to this sample as full sample. However the LHCb acceptance does not cover the full forward region, so some generated events are outside it. To account for this effect a smaller generator-level sample has been produced and the acceptance efficiency obtained from it as:

$$\epsilon^{acc} = \frac{N'^{acc}}{N'^{4\pi}} \qquad (6.12)$$

where N' indicates events in the small generator-level sample.

The effective number of events inside the LHCb acceptance in the full sample can be obtained by normalising the number of candidates in this sample by the ratio of the acceptance and the topological efficiencies:

$$N^{acc} = N^{topo} \cdot \frac{\epsilon^{acc}}{\epsilon^{topo}} \qquad (6.13)$$

where N denotes events in the full MC sample and ϵ^{topo} is extracted from the MC generation tables [107]. The number of events in the full sample, the efficiencies of each condition and the obtained effective number of events are reported in Table 6.7 for each magnet polarity.

On the other hand, the $B^0 \to K^{*0}\gamma$ sample contains only candidates where both the K^+ and π^- from the K^{*0} decay are within the LHCb acceptance. This condition is more stringent than requiring only the head of the decay to be within the acceptance, so in this case the effective number of events is larger than those present in the full sample. To account for this effect a small generator-level sample is produced requiring only that the B^0 is in the acceptance. Similarly to the previous case, the effective number of events in the full sample is obtained by normalising the generated events by the two acceptance efficiencies:

$$N^{acc} = N^{topo} \cdot \frac{\epsilon^{acc}}{\epsilon^{topo}} \qquad (6.14)$$

Table 6.8: Efficiencies of the generator level cut $\gamma\ p_{\mathrm{T}} > 1.5\,\mathrm{GeV}$ for the $B^0 \to K^{*0}\gamma$ MC sample split by magnet polarity and average.

Polarity	Efficiency (%)
Up	87.863 ± 0.084
Down	88.016 ± 0.085
Average	87.940 ± 0.060

Table 6.9: Reconstruction and stripping efficiencies for $\Lambda_b^0 \to \Lambda\gamma$ and $B^0 \to K^{*0}\gamma$.

	$\Lambda_b^0 \to \Lambda\gamma$	$B^0 \to K^{*0}\gamma$
$N_{acc}\ [10^6]$	24.71 ± 0.11	5.39 ± 0.42
$N_{strip}\ [10^4]$	33.812 ± 0.058	15.389 ± 0.039
$\epsilon^{reco,strip}\ [\%]$	1.3683 ± 0.0066	2.85 ± 0.22

where ϵ^{acc} is obtained from the small generator-level sample and ϵ^{topo} from the MC generation tables [108]. The value of each parameter and the final result is reported in Table 6.7 for the two magnet polarities.

Generator level requirements

In order to save disk space and CPU the production of simulated samples includes sometimes an extra selection at generator level, design to reject events that will not be used in the final selection and for which the process of emulating the detector response, reconstructing the candidates and storing them is unnecessary. The efficiency of this selection should however be taken into account since the MC sample does not include the rejected events. The $B^0 \to K^{*0}\gamma$ simulated sample includes the requirement that there is at least one photon in the event with transverse energy larger than $1.5\,\mathrm{GeV}$. Since a much stringent selection is applied latter on this variable, no events are lost in the final selection due to this generator level requirement. The efficiency of this condition is obtained from the MC generation statistics [108] and is reported in Table 6.8. No generator level requirement is imposed on the $\Lambda_b^0 \to \Lambda\gamma$ sample.

Reconstruction and stripping

The efficiency of the reconstruction algorithms and the stripping selection is evaluated on simulation as the number of events where a selected stripping candidate is matched to a simulated one over the effective number of generated events computed in Table 6.7. The results are reported in Table 6.9.

Preselection

The efficiency of the preselection defined in Sec. 6.3.3 is evaluated on simulation with respect to the events selected by the stripping. The PID cuts are treated separately in the next section and are not included here.

As discussed in Sec. 6.3.1, only candidates built from long tracks are kept in the preselection but most of the Λ from $\Lambda_b^0 \to \Lambda\gamma$ decay outside the VELO. The proportion of Λ reconstructed from long tracks in MC candidates satisfying the stripping requirements is $(19.746 \pm 0.068)\%$. For $B^0 \to K^{*0}\gamma$ this effect is negligible and is accounted for in the reconstruction efficiency, since only long tracks are used in the reconstruction of K^{*0}. On top of this, the preselection efficiency is $(31.85 \pm 0.18)\%$ and $(52.39 \pm 0.13)\%$ for $\Lambda_b^0 \to \Lambda\gamma$ and $B^0 \to K^{*0}\gamma$ signal events, respectively. The results are summarised in Table 6.10.

Table 6.10: Preselection efficiency for $\Lambda_b^0 \to \Lambda\gamma$ and $B^0 \to K^{*0}\gamma$. For $\Lambda_b^0 \to \Lambda\gamma$ the effect of selecting only candidates built from long tracks (LL) is accounted separately.

	$\Lambda_b^0 \to \Lambda\gamma$	$B^0 \to K^{*0}\gamma$
ϵ^{LL} [%]	19.746 ± 0.068	-
ϵ^{presel} [%]	27.25 ± 0.17	49.09 ± 0.13

Table 6.11: PID efficiency for $\Lambda_b^0 \to \Lambda\gamma$ and $B^0 \to K^{*0}\gamma$.

	$\Lambda_b^0 \to \Lambda\gamma$	$B^0 \to K^{*0}\gamma$
ϵ^{trPID} [%]	96.1984 ± 0.0019	95.71685 ± 0.000074

Charged PID

The efficiency of the charged PID selection is evaluated on top of the preselection. The PID variables are known to be not well reproduced in the simulation. Thus a data-driven method is needed to extract the PID efficiency. Calibration samples are provided by the PID group for each particle species. They contain pure candidates of a high rate mode that is self-tagging, *i.e.*, the particle type is known from the kinematics of the decay, without the need of PID cuts. In this way, the calibration tracks are PID unbiased and the efficiency of a given PID requirement can be obtained with a simple counting experiment. The method to obtain the efficiency for the decay of interest relies on the fact that the PID variables should give the same response for all tracks of a given species, no matter of their origin. The PID response depends however on the kinematics of the track. In particular, the strongest dependencies arise on the momenta and pseudorapidity (η) of the particle. Binning finely in these variables one can obtain kinematic regions where the PID response for a given particle specie is constant. Thus the PID efficiency for a given requirement is considered constant in this region and consequently the one obtained from the calibration samples can be used for any decay by reweighing for its kinematics. In practice, simulated events are used to reproduce the kinematics of the decay. The efficiency associated to each candidate is taken from the kinematic region where it belongs and the average for the full sample is computed. A tool named `PIDCalib` is used following this strategy. More details about this technique and its implementation can be found in Ref. [109].

For this analysis pure samples of p, $\pi^\pm$ and $K^\pm$ are obtained from $\Lambda \to p\pi^\mp$ and $D^0 \to K^\pm\pi^\mp$, respectively. The efficiencies of the PID requirements presented in Table 6.4 are computed from these samples in bins of p and η, using the binning scheme recommended by the PID group. The efficiency map for this configuration is shown in Fig. 6.15.

The p and η distributions for $\Lambda_b^0 \to \Lambda\gamma$ and $B^0 \to K^{*0}\gamma$ are obtained from simulated candidates satisfying the preselection requirements and are shown in Fig. 6.16. In the case of $\Lambda_b^0 \to \Lambda\gamma$ the events are weighted as explained in Section 6.3.4 to account for the mismodelling of the baryon momentum in MC. The weights are used to obtain the average PID efficiency as:

$$\bar{\epsilon} = \frac{\sum_i w_i \cdot \epsilon_i}{\sum_i w_i} \tag{6.15}$$

where w_i is the per-event weight and ϵ_i is the PID efficiency for event i obtained from the corresponding bin. The simulation does reproduce the kinematics of b-meson decays with accuracy and thus no weights are needed for $B^0 \to K^{*0}\gamma$, *i.e.*, $w_i = 1 \; \forall i$.

The average PID efficiencies are presented in Table 6.11 for both decay modes. The quoted errors are statistical only. For $\Lambda_b^0 \to \Lambda\gamma$ it is dominated by the uncertainty of the per-event weights. Systematic errors are expected to be larger for this method and we shall discuss them in detail in Sec. 6.6.
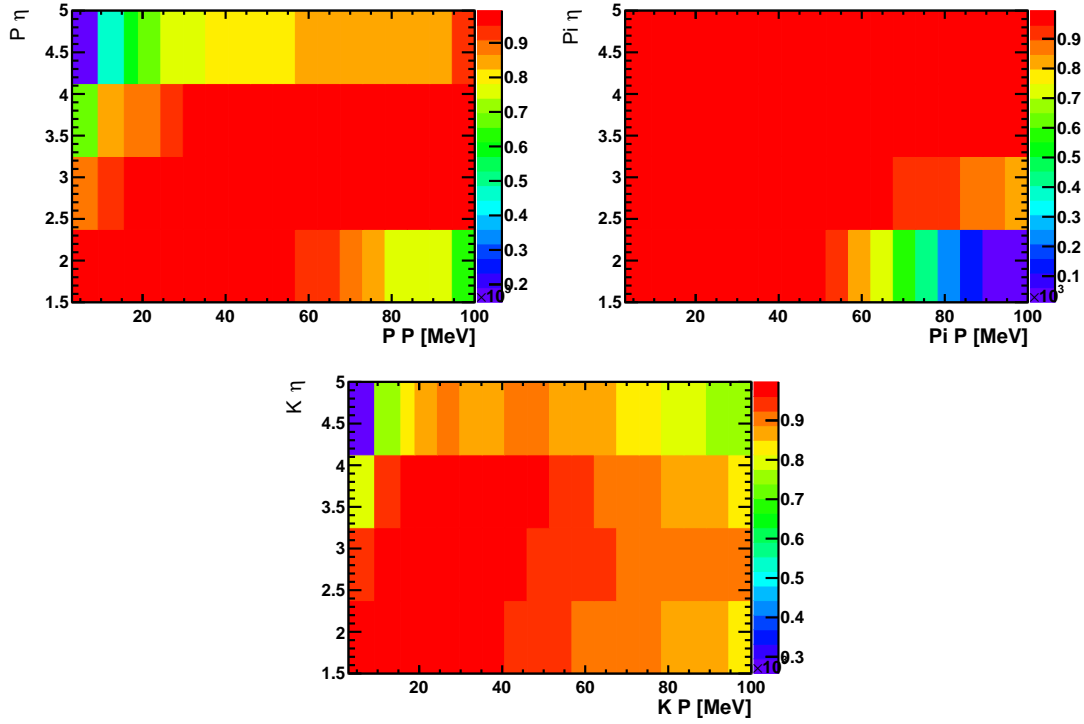
Figure 6.15: PID efficiencies in bins of momentum and pseudorapidity for p ProbNNp > 0.2 (top-left), $\pi^\pm$ ProbNNpi > 0.2 (top-right) and $K^\pm$ ProbNNK > 0.2 (bottom).

Table 6.12: BDT efficiency for $\Lambda_b^0 \to \Lambda\gamma$ and $B^0 \to K^{*0}\gamma$.

	$\Lambda_b^0 \to \Lambda\gamma$	$B^0 \to K^{*0}\gamma$
$\epsilon^{\text{BDT A}}$ [%]	27.27 ± 0.46	85.08 ± 0.19
$\epsilon^{\text{BDT B}}$ [%]	28.83 ± 0.47	85.23 ± 0.18
ϵ^{BDT} [%]	28.05 ± 0.33	85.15 ± 0.13

BDT

The BDT efficiency is obtained from MC on top of PID selected candidates. The BDT is applied to the simulation sample and the efficiency of the requirement on the output distribution is computed. For $\Lambda_b^0 \to \Lambda\gamma$ the p-p_{T} weights are taken into account.

As explained in Sec. 6.3.5 a BDT is trained on each half of the data. To get unbiased results the efficiency of each classifier is obtained from MC events corresponding to the other half, *i.e.*, events that have not been used to train that BDT. The efficiency of the two classifiers is found to be compatible within the statistical uncertainty as expected. The total BDT efficiency is obtained as the average of the two classifiers. The same strategy is used for the signal and normalisation modes and the results are presented in Table 6.12.
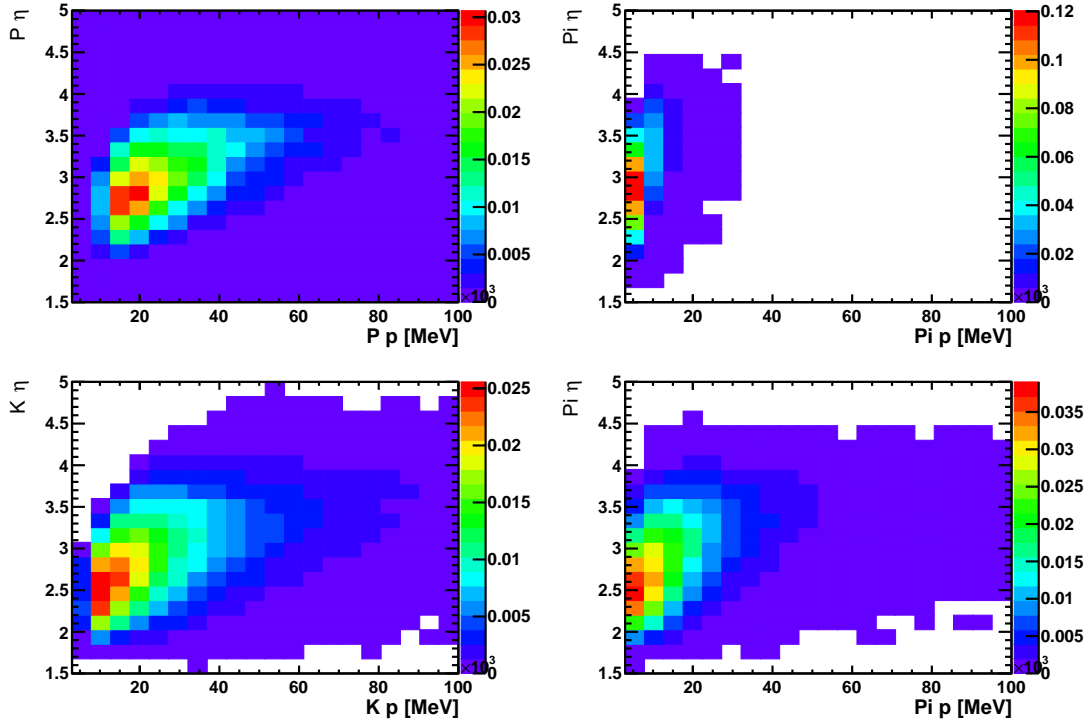
Figure 6.16: Momentum vs pseudorapidity distributions of p and $\pi^\pm$ from $\Lambda_b^0 \to \Lambda\gamma$ (top) and of $K^\pm$ and $\pi^\pm$ from $B^0 \to K^{*0}\gamma$ (bottom). MC candidates fulfilling the preselection requirements are shown.

Table 6.13: Neutral PID efficiency for $\Lambda_b^0 \to \Lambda\gamma$ and $B^0 \to K^{*0}\gamma$.

	$\Lambda_b^0 \to \Lambda\gamma$	$B^0 \to K^{*0}\gamma$
ϵ^{gPID} [%]	96.82 ± 0.40	96.578 ± 0.072

Neutral PID

The efficiency of the neutral PID requirement is computed using MC candidates that satisfy the BDT selection, taking into account the p-p_T weights for $\Lambda_b^0 \to \Lambda\gamma$. The results for each channel are reported in Table 6.13.

The neutral PID variables are known to be not perfectly modelled in the simulation. Unfortunately no calibration samples are available for 2016 data to extract the efficiency from data-driven methods. The possible systematic effect introduced by obtaining the efficiency from simulation is considered in Sec. 6.6.

Trigger

The trigger efficiency is obtained from MC candidates satisfying the full selection. Various trigger configurations at the hardware and HLT1 levels were used during the 2016 data-taking, which should be accounted for. Each of them is assigned a Trigger Configuration Key (TCK), an hexadecimal value uniquely identifying the full configuration. Table 6.14 summarises the different TCKs used during 2016 and the luminosity recorded with each of them, together with the L0 and HLT1 settings relevant for this analysis.

Table 6.14: L0 and HLT1 TCKs used during the 2016 LHCb data-taking, luminosity recorded with each of them and settings relevant to this analysis.

TCK	Luminosity $[\,\mathrm{pb}^{-1}\,]$	L0 E_T threshold $[\,\mathrm{MeV}\,]$		HLT1 configuration
		L0 Photon	L0 Electron	
0x11291603	35.00	2304	2122	Loose
0x11291604	24.78	2785	2256	Loose
0x11291605	78.42	2976	2592	Loose
0x11321609	107.00	2800	2400	Loose
0x11341609	118.06	2800	2400	Tight
0x11351609	23.46	2800	2400	Tighter
0x11361609	414.62	2800	2400	Tighter
0x11371609	72.14	2800	2400	Tighter
0x1137160e	22.76	2976	2592	Tighter
0x1138160f	575.25	2784	2400	Loose
0x11381611	44.13	2976	2616	Loose
0x11381612	89.73	2976	2616	Loose
0x11381609	6.86	2800	2400	Loose
0x1138160e	31.70	2976	2592	Loose

The L0 threshold applied on the photon transverse energy (E_T) evolved during the year, the tightest being $E_\mathrm{T} > 2976\,\mathrm{MeV}$. Since a more stringent requirement on this quantity is applied in the offline selection (see Table 6.4), the different L0 configurations should not have an impact on the total efficiency and are thus not accounted for. Differences in the measurement of the photon energy between the L0 and the offline reconstruction are studied in Sec. 6.6 and potential effects arising from them are assigned as systematic uncertainties.

The HLT1 requirement also changed during the year and this is expected to have an impact on the total trigger efficiency. More specifically three different configurations were used, varying the ellipsoidal cut on the p_T-IPχ^2 plane of a given track. The HLT2 configuration relevant for this analysis was stable during the full year.

Effectively, three different trigger configurations were used to select the data, which we refer to as loose, tight and tighter, corresponding to the different HLT1 settings. However only the tight configuration, the most used during the data-taking, is emulated in the MC samples used for this analysis. Moreover, the trigger software as run online can not process the MC offline selected candidates since the raw information from the detectors as used by the trigger is not available in our samples. Thus the trigger requirements in the different configurations are reproduced using the offline reconstructed information, which for tracking related variables as used at HLT1 is perfectly aligned to the trigger version.

The luminosity recorded with each configuration and its efficiency on $\Lambda_b^0 \to \Lambda\gamma$ and $B^0 \to K^{*0}\gamma$ candidates satisfying the full offline selection are summarised in Table 6.15. The final efficiency is computed as the weighted average of the different configurations taking into account the luminosity recorded with each of them.

6.4.4 Normalisation constant

Putting all the terms obtained in the previous sections together the value of the normalisation constant is obtained from Eq. 6.7:

$$\alpha = 716 \pm 81 \pm 28 \tag{6.16}$$

where the first uncertainty comes from the ratio of hadronisation fractions and the second from the combined uncertainty on the input branching ratios and the ratio of selection efficiencies.

Table 6.15: Effective trigger configurations used during the 2016 data-taking, luminosity recorded with them and efficiency selecting $\Lambda_b^0 \to \Lambda\gamma$ and $B^0 \to K^{*0}\gamma$ events. The weighted average for each channel is obtained taking into account the amount of data recorded in each configuration.

Configuration	Luminosity $[\,\text{pb}^{-1}\,]$	Efficiency on $\Lambda_b^0 \to \Lambda\gamma$ [%]	Efficiency on $B^0 \to K^{*0}\gamma$ [%]
Loose	992.89	83.27 ± 0.58	77.72 ± 0.17
Tight	118.06	82.49 ± 0.58	76.74 ± 0.17
Tighter	532.98	80.16 ± 0.60	74.64 ± 0.18
Weighted average	1643.93	82.21 ± 0.40	76.65 ± 0.12

6.5   Mass fit

As discussed in the previous section, the $\mathcal{B}(\Lambda_b^0 \to \Lambda\gamma)$ will be obtained from the signal yield observed in data. The event selection developed in Sec. 6.3 is designed to separate signal events from the large combinatorial background but it is not a perfect discriminant so non-signal events remain in the final selected sample. In order to extract the signal yield, the different components need to be disentangled. This is achieved by means of an unbinned maximum likelihood fit to the invariant mass distribution of the selected candidates.

The adopted fit strategy consists on a simultaneous fit to the signal and normalisation modes. This allows in the first place to extract the $\mathcal{B}(\Lambda_b^0 \to \Lambda\gamma)$ and $N(B^0 \to K^{*0}\gamma)$ parameters from a single fit, ensuring the correlations between both values are properly accounted for. Moreover other nuisance parameters of the fit such as the signal peak position and width can be shared between the signal and normalisation modes. This is helpful when fitting low yield samples where the available statistics might not be enough to disentangle univocally all the parameters entering in the fit, as it is the case for the $\Lambda_b^0 \to \Lambda\gamma$ channel. In the following the shapes and parameters used to describe the signal, normalisation and background components are presented.

6.5.1   Signal shape

The $\Lambda_b^0 \to \Lambda\gamma$ and $B^0 \to K^{*0}\gamma$ invariant mass distributions are modeled by a double-tail Crystal Ball [77], a function composed of a Gaussian core and two independent power-law tails above and over certain thresholds that account for different energy losses at low and high mass:

$$CB(m; \mu, \sigma, \alpha_L, \alpha_R, n_L, n_R) = N \cdot \begin{cases} A_L \cdot \left(B_L - \frac{m-\mu}{\sigma}\right)^{-n_L}, & \text{for } \frac{m-\mu}{\sigma} \leq -|\alpha_L| \\ \exp\left(-\frac{(m-\mu)^2}{2\sigma^2}\right), & \text{for } -|\alpha_L| < \frac{m-\mu}{\sigma} < |\alpha_R| \\ A_R \cdot \left(B_R - \frac{m-\mu}{\sigma}\right)^{-n_R}, & \text{for } \frac{m-\mu}{\sigma} \geq |\alpha_R| \end{cases} \quad (6.17)$$

where N is a normalisation factor and

$$A_X = \left(\frac{n_X}{|\alpha_X|}\right)^{n_X} \exp\left(-\frac{1}{2}|\alpha_X|^2\right) \qquad B_X = -\frac{n_X}{|\alpha_X|} + |\alpha_X|$$

for $X = L, R$.

The tail parameters are extracted from a fit to simulated candidates satisfying the full selection. The mean and sigma of the Gaussian core are left free in the fit to data for the normalisation mode. For $\Lambda_b^0 \to \Lambda\gamma$ they are described as a function of the $B^0 \to K^{*0}\gamma$ parameters:

$$\mu^{\Lambda_b^0} = \mu^{B^0} + \Delta M \qquad \sigma^{\Lambda_b^0} = \sigma^{B^0} \cdot f_\sigma \quad (6.18)$$

where $\Delta M = 339.72 \pm 0.30\,\text{MeV}$ is the mass difference as measured by LHCb [110] and f_σ is a scale factor obtained from simulation that takes into account possible differences in the mass resolution arising from
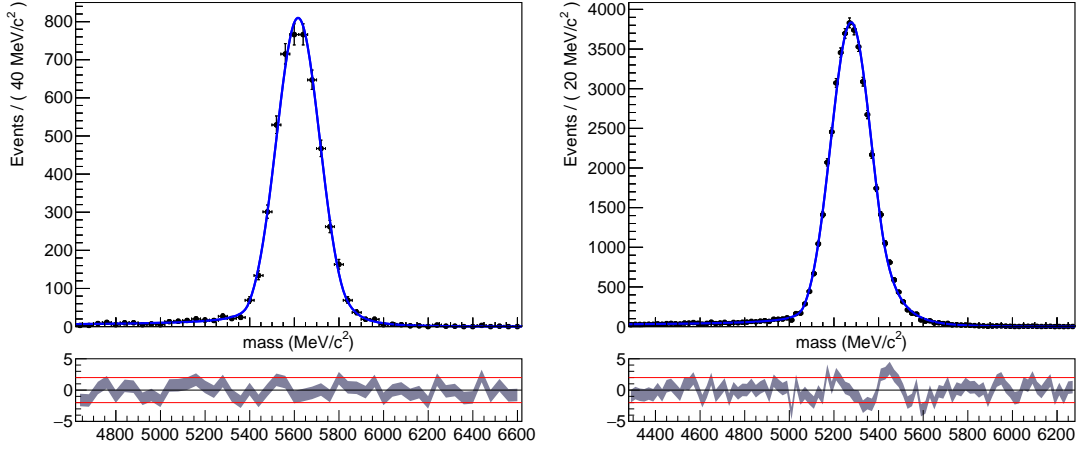
Figure 6.17: Invariant mass distribution of selected MC $\Lambda_b^0 \to \Lambda\gamma$ (left) and $B^0 \to K^{*0}\gamma$ (right) candidates (black dots). The results of a simultaneous fit with a double-tail Crystal Ball for each decay are overlaid (blue curve).

Table 6.16: $\Lambda_b^0 \to \Lambda\gamma$ and $B^0 \to K^{*0}\gamma$ invariant mass distribution shape parameters from a simultaneous fit with a double-tail Crystal Ball for each decay.

Parameter	Value
α_L^{signal}	1.98 ± 0.14
α_R^{signal}	2.306 ± 0.080
n_L^{signal}	3.38 ± 0.85
n_R^{signal}	0.64 ± 0.12
f_σ	1.069 ± 0.016
α_L^{norm}	1.466 ± 0.036
α_R^{norm}	2.355 ± 0.030
n_L^{norm}	7.17 ± 0.70
n_R^{norm}	0.582 ± 0.041
μ^{B^0}	5276.83 ± 0.54
σ^{B^0}	91.23 ± 0.54

the different mass scale [111]. This factor is expected to be small since the mass resolution of both the signal and the normalisation modes is dominated by the photon energy resolution.

The results of the simultaneous fit on simulated $\Lambda_b^0 \to \Lambda\gamma$ and $B^0 \to K^{*0}\gamma$ candidates are shown in Fig. 6.17 and the obtained fit parameters are summarised in Table 6.16. The mean of the $B^0 \to K^{*0}\gamma$ peak is slightly smaller than the B^0 world average mass [51], which can be caused by a small miscalibration of the MC and so this parameter and the width of the distribution are left free in the fit to data. The scale factor between the resolution on the signal and normalisation modes is found to be a bit larger than unity, as could be explained by the dependency on the mass scale. This parameter is fixed to this value in the fit to data but potential differences between MC and data are evaluated in Sec. 6.6 by allowing it to float.

Table 6.17: Physical background contributions to $B^0 \to K^{*0}\gamma$ and their shape parameters obtained in Ref. [42].

Parameter	Missing pion	$K^+\pi^-\pi^0 X$
Δm [MeV]	-139.57	-418.7
c	-5.5	-3.3
p	0.13	1.7
f_σ	1.21	2.15

6.5.2   Background studies

One of the main sources of background is that coming from a random combination of a $p\pi$ ($K\pi$) and a photon. This contamination is referred to as combinatorial background and it is modeled by an exponential distribution with free yield and decay parameter:

$$\text{Exp}(m; \tau) = \frac{1}{\tau} \exp(\tau \cdot m) \tag{6.19}$$

where τ is the decay parameter.

In addition to the combinatorial background, any b-decay with at least two hadrons and a high-E_T neutral particle in the final state can potentially be reconstructed as a signal candidate. These decays should satisfy the full event selection in order to contribute to the selected sample and are in general suppressed by it. In order to evaluate which are the most dangerous sources of background different decays are studied using simulation.

Backgrounds for $B^0 \to K^{*0}\gamma$

The background sources for the $B^0 \to K^{*0}\gamma$ decay were studied in detail in Ref. [42] with MC in Run 1 conditions. Since no Run 2 background samples are available at the moment of writing to repeat these studies, we use the main contributions and their shapes as obtained in Ref. [42]. In particular, we include a term to account for any decay to a $K^+\pi^+\pi^-$ and a neutral (γ or π^0) final state where one of the pions has not been reconstructed and a π^0 might have been wrongly identified as a photon. This contribution is referred to as missing pion. A second term is included to account for partially reconstructed backgrounds with a π^0 in the final state and any missing particle, which we refer to as $K^+\pi^-\pi^0 X$. Both backgrounds are modeled with a generalised Argus probability density function (PDF) [112], which is defined as:

$$A(m; m_0, c, p) = \frac{2^{-p} \cdot c^{2(p+1)}}{\Gamma(p+1) - \Gamma(p+1, \frac{1}{2}c^2)} \frac{m}{m_0} \left(1 - \frac{m^2}{m_0^2}\right)^p \exp{-\frac{1}{2}c^2\left(1 - \frac{m^2}{m_0^2}\right)} \tag{6.20}$$

where $\Gamma(x)$ is the gamma function and $\Gamma(x; x_0)$ is the upper incomplete gamma function. The parameters m_0, c and p represent the threshold, slope and power, respectively, and the PDF is defined in the range $0 \le m \le m_0$. We describe the threshold as $m_0 = m_{B^0} - \Delta m$ where m_{B^0} is the mean of the PDF describing the $B^0 \to K^{*0}\gamma$ signal. For the missing pion contribution Δm is fixed to the pion mass while it is obtained from simulation for $K^+\pi^-\pi^0 X$. The Argus PDF is convolved with a Gaussian to account for the detector resolution, the mean of which is fixed to zero since no bias should be introduced by this effect and the width is described as a function of the signal width, $\sigma^{res} = f_\sigma \cdot \sigma^{B^0 \to K^{*0}\gamma}$. The shape parameters are fixed in the fit to data and their values are summarised in Table 6.17, while the yields are free to vary.

Backgrounds for $\Lambda_b^0 \to \Lambda\gamma$

Potential background contributions to $\Lambda_b^0 \to \Lambda\gamma$ are studied in detail from simulation. The samples used for these studies are listed in Table 6.18. For some decay modes no MC is available in 2016 conditions

Table 6.18: Backgrounds to $\Lambda_b^0 \to \Lambda\gamma$, simulation samples used for the studies and expected normalised contamination obtained.

Decay mode	Simulation type	Expected normalised contamination
$B^0 \to K^{*0}\gamma$	2016	$< 2.0 \times 10^{-7}$
$B_s^0 \to \phi\gamma$	2016	$< 4.4 \times 10^{-8}$
$\Lambda_b^0 \to \Lambda(1520)\gamma$	2012	$< 1.7 \times 10^{-7}$
$\Lambda_b^0 \to \Lambda(1670)\gamma$	2012	$< 2.7 \times 10^{-7}$
$\Lambda_b^0 \to \Lambda(1820)\gamma$	2012	$< 3.0 \times 10^{-7}$
$\Lambda_b^0 \to \Lambda(1830)\gamma$	2012	$< 3.0 \times 10^{-7}$
$\Lambda_b^0 \to \Lambda^*\gamma, \Lambda^* \to \Lambda\gamma$	RapidSim	$(8.2 \pm 2.0) \times 10^{-8}$
$\Lambda_b^0 \to \Lambda\eta, \eta \to \gamma\gamma$	2016	$(3.2 \pm 2.5) \times 10^{-6}$
$\Xi_b^- \to \Xi\gamma$	2012	$< 7.5 \times 10^{-8}$
$\Lambda_b^0 \to \Lambda_c^+(\to \Lambda\pi^+)D^-(\to \pi^-\pi^0)$	RapidSim	$(8.8 \pm 1.4) \times 10^{-13}$
$\Lambda_b^0 \to \Lambda_c^+(\to \Lambda\pi^+)D_s^-(\to K^0\pi^-\pi^0)$	RapidSim	$(3.5 \pm 0.8) \times 10^{-11}$

so samples simulating the 2012 ones are used as a proxy. When no MC is available at all for a given channel, the RapidSim [113] fast MC generator is used to generate the kinematics of the decay of interest including momenta smearing. In this case, only the kinematic selection can be applied and a RapidSim signal sample is used to obtain the ratio of selection efficiencies. This is expected to provide a good estimation of the contamination for decays where the differences to the signal mode arise mainly from the kinematics.

The contamination of a given background, $H_b \to X$, is defined as:

$$C_{H_b \to X} = \frac{N(H_b \to X)}{N(signal)} = \frac{f_{H_b}}{f_{\Lambda_b^0}} \cdot \frac{\mathcal{B}(H_b \to X)}{\mathcal{B}(\Lambda_b^0 \to \Lambda\gamma)} \cdot \frac{\epsilon_{MC}(H_b \to X)}{\epsilon_{MC}(signal)} \qquad (6.21)$$

where $N(X)$ is the yield of the given decay after the full selection, $\epsilon_{MC}(X)$ is the reconstruction and selection efficiency for mode X obtained from the simulation, f_{H_b} is the probability that a b-quark hadronises into H_b and $\mathcal{B}(X)$ is the branching fraction of the particular mode. Since the $\mathcal{B}(\Lambda_b^0 \to \Lambda\gamma)$ is not known a normalised contamination is defined as:

$$C_{H_b \to X}^{norm} = \mathcal{B}(\Lambda_b^0 \to \Lambda\gamma) \cdot C_{H_b \to X} = \frac{f_{H_b}}{f_{\Lambda_b^0}} \cdot \mathcal{B}(H_b \to X) \cdot \frac{\epsilon_{MC}(H_b \to X)}{\epsilon_{MC}(signal)} \qquad (6.22)$$

Since the signal branching fraction is expected to be of the order $10^{-6} - 10^{-5}$, only normalised contaminations larger than 5×10^{-7} will be considered significant.

Detailed studies have been performed to estimate the contaminations from different decay modes. The simulated background samples reconstructed and selected as the signal mode are used to obtain the efficiencies. When a significant contamination is expected the mass shape is obtained from the same samples and a term is added to the final mass fit to account for this contribution. The contaminations for all the studied backgrounds are reported in Table 6.18 and their computation is detailed below grouped by physics origin.

Mis-identified backgrounds This category includes any decay to an $hh\gamma/\pi^0$ final state where one of the hadrons has been wrongly identified or a π^0 has been miss-identified as a photon. The first type is largely suppressed by the purity of the Λ selection but some small contamination is still possible. Decays contributing to this background type are $B^0 \to K^{*0}\gamma$, $B_s^0 \to \phi\gamma$ and $\Lambda_b^0 \to pK^-\gamma$. No events from the simulated samples of these decays satisfy the full selection so upper limits are obtained for their contaminations. The $\mathcal{B}(\Lambda_b^0 \to pK^-\gamma)$ has not been measured to date but it has been studied in Ref. [105] and estimated to be:

$$\mathcal{B}(\Lambda_b^0 \to pK^-\gamma) = (3.39 \pm 0.48) \times 10^{-5} \qquad (6.23)$$

Table 6.19: Branching fractions for the decays $X_b \to X J/\psi$ taking into account the hadronisation fractions.

Decay mode	$\mathcal{B}(X_b \to X J/\psi) \times \mathcal{B}(b \to X_b)[10^{-5}]$
$\Lambda_b^0 \to \Lambda J/\psi$	5.8 ± 0.8
$\Xi_b^- \to \Xi J/\psi$	$1.02\,{}^{+\,0.26}_{-\,0.21}$

including resonant and non-resonant pK^- contributions in a mass range $[1400 - 2600]\,\text{MeV}$ dominated by the $\Lambda(1520)$ peak. Simulated samples for different Λ^* resonances are available as shown in Table 6.18. Since the exact contribution of each of them to the total pK^- spectra is not known we use the full $\mathcal{B}(\Lambda_b^0 \to pK^-\gamma)$ for each term to obtain a safe upper limit on the contamination. All the contributions from this type are found to be negligible.

The main background from a π^0 mis-identification comes from $\Lambda_b^0 \to \Lambda\pi^0$. This decay has never been observed at experiments and no reliable prediction is available to our knowledge. Furthermore, no simulated sample for $\Lambda_b^0 \to \Lambda\pi^0$ is available and in this case the RapidSim generator is not helpful since the differences between this decay and the signal arise mostly from the γ/π^0 separation power of the IsPhoton requirement, which can not be reproduced by RapidSim. On top of this, these events are expected to accumulate right under the signal peak so cannot be directly distinguished by the invariant mass fit. Consequently any potential contamination from this background is absorbed in the signal contribution. Cross-checks are performed in Sec. 6.7 to estimate the effect of this assumption.

Partially reconstructed radiative decays Any radiative decay to a $\Lambda\gamma X$ final state can mimic the signal if part of the decay has not been reconstructed. Decays with this topology include $\Lambda_b^0 \to \Lambda^*\gamma$ with $\Lambda^* \to \Lambda\gamma$ and $\Xi_b^- \to \Xi\gamma$ with $\Xi \to \Lambda\pi^-$ almost 100% of the times. Neither of these decays has been observed to date but some predictions and estimations are available.

For the first mode, only the $\Lambda(1520)$ has been observed to decay to $\Lambda\gamma$, with a probability of $(0.85 \pm 0.15)\%$, but the branching fraction of the exclusive $\Lambda_b^0 \to \Lambda(1520)\gamma$ is not known. The $\mathcal{B}(\Lambda_b^0 \to pK^-\gamma)$ from Eq. 6.23 is used instead as an upper limit for $\mathcal{B}(\Lambda_b^0 \to \Lambda(1520)\gamma)$. The contamination from this mode is found to be negligible.

No predictions for the decay mode $\Xi_b^- \to \Xi\gamma$ are available in the literature to our knowledge but since the underlying quark transition is the same as for $\Lambda_b^0 \to \Lambda\gamma$, difference will mainly arise from form factors. To estimate this effect, the corresponding J/ψ modes are compared. The measured branching ratios are shown in Table 6.19 taking into account also the hadronisation probabilities and the proportions are assumed to hold for the corresponding radiative decays. No candidates satisfy the full signal selection and thus an upper limit on the contamination from this mode is obtained and is found to be negligible. Other partially reconstructed radiative decays, such as $\Omega_b^- \to \Omega\gamma$ are expected to be further suppressed and are not considered.

Partially reconstructed backgrounds with π^0 Another dangerous source of partially reconstructed background comes from b-baryon decays with a π^0 in the final state, specially those including also a Λ. The copious $\Lambda_b^0 \to \Lambda_c^+\pi^-$ with either $\Lambda_c^+ \to \Lambda\pi^+\pi^0$ or $\Lambda_c^+ \to pK_S^0\pi^0$ contributes to very low mass (outside the signal region) since both the Λ and the π^0 come from the light Λ_c^+, and is thus not considered. Decays with an intermediate $\Lambda_c^+ \to \Lambda\pi^+$ and a π^0 have smaller branching rations but might still contribute if selection efficiencies are large. As proxy for this kind of decays, the $\Lambda_b^0 \to \Lambda_c^+(\to \Lambda\pi^+)D^-(\to \pi^-\pi^0)$ and $\Lambda_b^0 \to \Lambda_c^+(\to \Lambda\pi^+)D_s^-(\to K^0\pi^-\pi^0)$ modes are studied using RapidSim. The kinematic selection efficiencies are found to be very small and thus the contamination from these decays is also negligible.

Partially reconstructed backgrounds with η The last source of partially reconstructed background comes from decays with an η going to $\eta \to \gamma\gamma$ where one of the photons is not reconstructed. The most dangerous mode of this type is $\Lambda_b^0 \to \Lambda\eta$, which has been observed at LHCb through the $\pi^+\pi^-\pi^0$

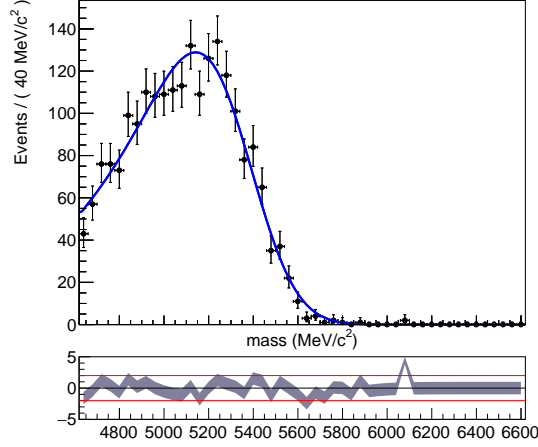Figure 6.18: $\Lambda_b^0 \to \Lambda\eta$ simulated events reconstructed as $\Lambda_b^0 \to \Lambda\gamma$ (black dots) and result of a fit with a double-tail Crystal Ball (blue curve).

Table 6.20: Shape parameters of the $\Lambda_b^0 \to \Lambda\eta$ contribution to the $p\pi^-\gamma$ invariant mass distribution as obtained from the fit in Fig. 6.18.

Parameter	Value
Δm	-227 ± 66
c	-7.9 ± 4.1
p	0.32 ± 0.20
f_σ	1.73 ± 0.29

decay of the η and its branching ratio has been measured to be similar to the expected signal one, $\mathcal{B}(\Lambda_b^0 \to \Lambda\eta) = \left(9.3^{+7.3}_{-5.3}\right) \times 10^{-6}$ [114]. The contamination of this mode is studied with simulated candidates and is found to be potentially significant. Thus a term is added to the $p\pi^-\gamma$ invariant mass model to account for this contribution. It is modelled by an Argus distribution convolved with a Gaussian to account for the resolution and the shape parameters are obtained from a fit to simulated events, as shown in Fig. 6.18 and reported in Table 6.20, with the mean and width of the Gaussian core expressed as a function of the signal parameters, $\mu^{\Lambda_b^0 \to \Lambda\eta} = \mu^{\Lambda_b^0 \to \Lambda\gamma} + \Delta m$ and $\sigma^{\Lambda_b^0 \to \Lambda\eta} = f_\sigma \cdot \sigma^{\Lambda_b^0 \to \Lambda\gamma}$. The expected yield in data for this mode after the full selection is 46 ± 39. This value is included in the nominal fit to data with a Gaussian constraint. This is the only source of physical background to $\Lambda_b^0 \to \Lambda\gamma$ found to be relevant.

6.5.3 Blind mass fit

In order to validate the normalisation and background model a simultaneous fit is first performed with the signal region 5100–6100 MeV in the $p\pi^-\gamma$ invariant mass distribution blinded. Only the background PDFs are included for this category. The normalisation mode is fitted in the full range with all the contributions obtained in the previous sections. The mean and width of the Gaussian core describing the $B^0 \to K^{*0}\gamma$ peak are left free in this fit, together with the signal, combinatorial, missing pion and $K^+\pi^-\pi^0 X$ yields in the normalisation model and the combinatorial yield in the signal one. The yield of the $\Lambda_b^0 \to \Lambda\eta$ is fixed in this fit to the contamination expected in the side-band regions while for the final fit it will be constrained to the yield expected from MC. The slope of the combinatorial background is also free in both models. The results of the fit are shown in Fig. 6.19 and the values of the free parameters are listed in Table 6.21. It can be seen that the distributions describe the data both for the signal side-bands
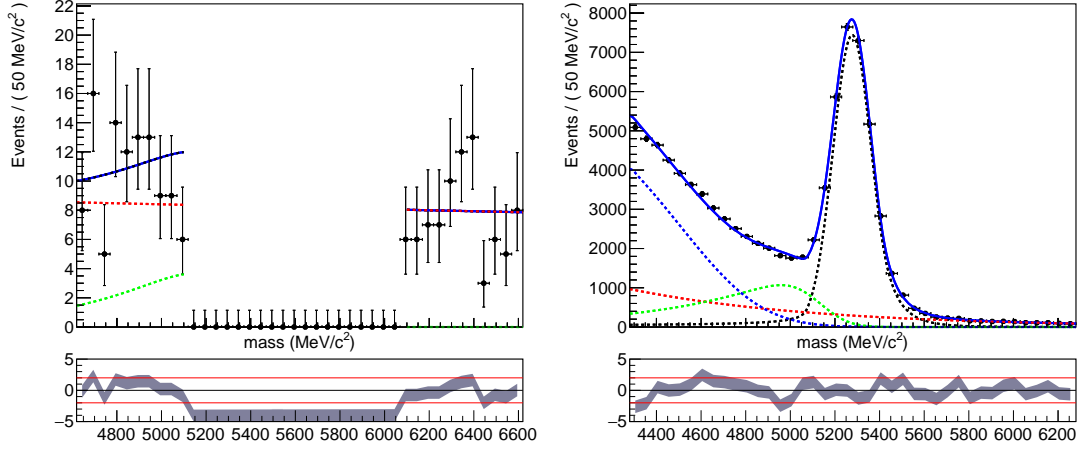
Figure 6.19: Simultaneous fit to the $p\pi^-\gamma$ (left) and $K^+\pi^-\gamma$ (right) invariant mass distributions of the data candidates with the $p\pi^-\gamma$ signal region blinded. The data is represented by black dots and the result of the fit by a solid blue curve. The dashed black line describes the signal contribution, the red dashed one the combinatorial background and the dashed blue (and green) the $\Lambda_b^0 \to \Lambda\eta$ (missing pion and $K^+\pi^-\pi^0 X$) for $p\pi^-\gamma$ ($K^+\pi^-\gamma$).

Table 6.21: Values of the fit parameters of the $p\pi^-\gamma$ (left) and $K^+\pi^-\gamma$ (right) invariant mass models obtained from the blinded simultaneous fit to data candidates shown in Fig. 6.19.

| Parameter	Value
N_{comb}	164 ± 23
τ_{comb}	$(-0.4 \pm 1.1) \cdot 10^{-4}$
N_{signal}	34650 ± 190
N_{comb}	14600 ± 1200
$N_{mis-\pi}$	13290 ± 360
$N_{K^+\pi^-\pi^0 X}$	26740 ± 810
μ^{B^0}	5277.37 ± 0.46
σ^{B^0}	85.97 ± 0.46
τ_{comb}	$(-1.202 \pm 0.080) \cdot 10^{-3}$

and the normalisation mode accurately validating the invariant mass models.

Before proceeding with the final fit to the full $p\pi^-\gamma$ mass distribution, the stability and performance of the final configuration is assessed with pseudo-experiments. The $\Lambda_b^0 \to \Lambda\gamma$ component is added to the $p\pi^-\gamma$ description to build the final model. Events are generated using the parameters obtained from the blind fit for the normalisation and background components. For the signal the shape parameters are fixed to those obtained from simulation. Three sets of experiments are run with $\mathcal{B}(\Lambda_b^0 \to \Lambda\gamma) = \{1 \times 10^{-5}, 5 \times 10^{-6}, 1 \times 10^{-6}\}$ to account for the range of predictions from the theory. For each configuration, 1000 datasets are generated and fit with the full model.

The pull distributions for the $\mathcal{B}(\Lambda_b^0 \to \Lambda\gamma)$ parameter obtained from the three experiments are shown in Fig. 6.20. The shapes are compatible with a normal distribution in all the cases proving that the fit does not introduce any bias on the measurement of this parameter and that the statistical error is properly estimated. The same is observed for the rest of the free parameters in the final fit configuration, the pull distributions of which can be found in Appendix A. This validates the invariant mass model that shall be used in the final fit to data.

Table 6.22: Probability to achieve an evidence or observation obtained from pseudoexperiments for the different $\mathcal{B}(\Lambda_b^0 \to \Lambda\gamma)$ hypothesis.

$\mathcal{B}(\Lambda_b^0 \to \Lambda\gamma)$	Probability ($\sigma \geq 3$)	Probability ($\sigma \geq 5$)
1×10^{-5}	100.0%	100.0%
5×10^{-6}	100.0%	100.0%
3×10^{-6}	99.6%	88.2%
1×10^{-6}	24.9%	1.1%
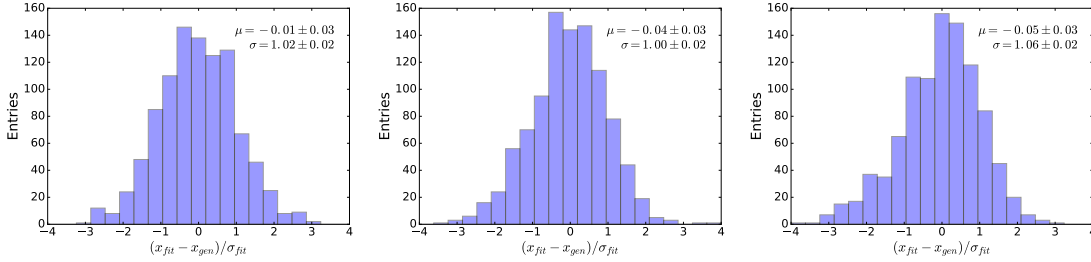
Figure 6.20: Pull distributions of the $\mathcal{B}(\Lambda_b^0 \to \Lambda\gamma)$ parameter obtained from 1000 pseudoexperiments generated with the hypotheses $\mathcal{B}(\Lambda_b^0 \to \Lambda\gamma) = \{1 \times 10^{-5}, 5 \times 10^{-6}, 1 \times 10^{-6}\}$ (left, middle and right, respectively).

The pseudoexperiments allow also to extract the probability to achieve an evidence or observation for a given $\mathcal{B}(\Lambda_b^0 \to \Lambda\gamma)$ hypothesis. This is computed by counting the number of experiments providing a signal significance higher than 3 or 5, respectively. For each generated pseudo-dataset two fits are performed, one with the nominal configuration, allowing the $\mathcal{B}(\Lambda_b^0 \to \Lambda\gamma)$ parameter to float, and a second one with this value fixed to zero (null hypothesis). Following Wilks' theorem [87] the statistical significance with which the null hypothesis can be rejected is given by the logarithm of the ratio of the minimized likelihood of the fits:

$$\sigma_i^2 = -2 \cdot \log \frac{\mathcal{L}_i(H_1)}{\mathcal{L}_i(H_0)} \tag{6.24}$$

where $\mathcal{L}$ is the Likelihood value obtained from the null hypothesis (H_0) and the alternative hypothesis (H_1). The probabilities obtained for different branching fractions are reported in Table 6.22, where an extra $\mathcal{B}(\Lambda_b^0 \to \Lambda\gamma)$ value has been added. In summary, if the $\mathcal{B}(\Lambda_b^0 \to \Lambda\gamma)$ is larger than 3×10^{-6} we shall with high probability achieve an observation of this decay mode using the 2016 dataset.

6.5.4 Fit results

The final invariant mass model described above is used to fit the selected data candidates, with the $\Lambda_b^0 \to \Lambda\eta$ yield and the mass difference between Λ_b^0 and B^0 constrained to the values obtained from MC and from the LHCb measurement, respectively. The result of the simultaneous fit on the full mass range is shown in Fig. 6.21 and the values of the free parameters are reported in Table 6.23.

A clear $\Lambda_b^0 \to \Lambda\gamma$ peak of (64 ± 13) events is observed in the $p\pi\gamma$ invariant mass spectra. In order to quantify its significance a profile likelihood scan is performed, shown in Fig. 6.22. The difference in the likelihood value between the best fit point and the null hypothesis gives a measure of the significance of the signal:

$$s = \sqrt{2 \cdot \Delta(\log \mathcal{L})} \tag{6.25}$$

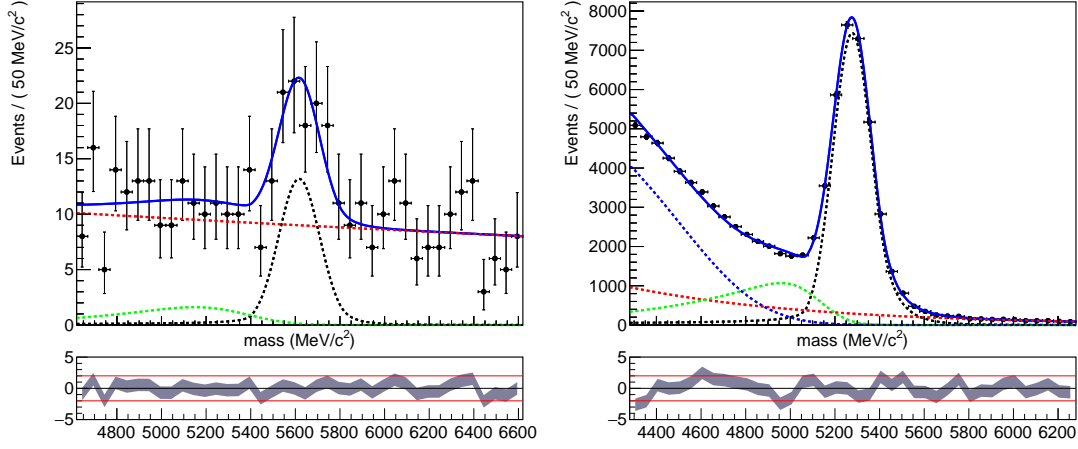A statistical significance of 5.7σ is obtained.

Figure 6.21: Simultaneous fit to the $p\pi^-\gamma$ (left) and $K^+\pi^-\gamma$ (right) invariant mass distributions of the selected data candidates. The data is represented by black dots and the result of the fit by a solid blue curve. The dashed black line describes the signal contribution, the red dashed one the combinatorial background and the dashed blue (and green) the $\Lambda_b^0 \to \Lambda\eta$ (missing pion and $K^+\pi^-\pi^0 X$) for $p\pi^-\gamma$ ($K^+\pi^-\gamma$).

Table 6.23: Values of the fit parameters of the $p\pi^-\gamma$ (left) and $K^+\pi^-\gamma$ (right) invariant mass models obtained from the blinded simultaneous fit to data candidates shown in Fig. 6.21.

Parameter	Value
$\mathcal{B}(\Lambda_b^0 \to \Lambda\gamma)$	$(2.59 \pm 0.52) \times 10^{-6}$
$\Delta\mu$	$339.72 \pm 0.30\,\mathrm{MeV}$
$N_{\Lambda_b^0 \to \Lambda\eta}$	21 ± 22
N_{comb}	361 ± 30
τ_{comb}	$(-1.2 \pm 1.2) \times 10^{-4}$
$N_{B^0 \to K^{*0}\gamma}$	34650 ± 270
μ^{B^0}	5277.44 ± 0.63
σ^{B^0}	85.98 ± 0.64
$N_{mis-\pi}$	13310 ± 480
$N_{K^+\pi^-\pi^0 X}$	26800 ± 1000
N_{comb}	15000 ± 1600
τ_{comb}	$(-1.2 \pm 0.10) \times 10^{-3}$

The measured μ^{B^0} is in good agreement with the world average B^0 mass [51] and the mass difference between Λ_b^0 and B^0, $\Delta\mu$, as measured by LHCb [110] is recovered. The mass resolution is similar to that reported by LHCb in Run 1 for radiative decays [42] and has been achieved thanks to the offline recalibration of the data to account for ageing effects in the ECAL.

6.6 Systematic uncertainties

Possible sources of systematic uncertainties affecting the measurements obtained in the previous section are studied. They are split in two main groups: uncertainties coming from the fit model, which affect both the significance of the signal and the measurement of the branching ratio, and systematic uncertainties on the computation of the normalisation constant, which affect only the latter.
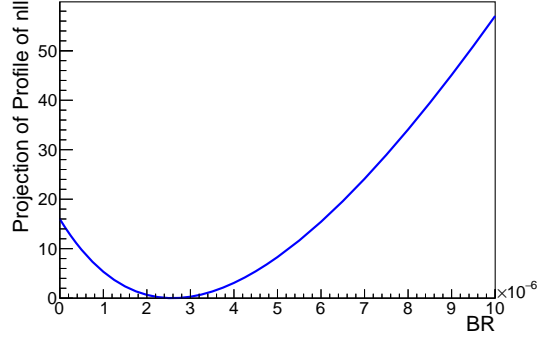
Figure 6.22: Profile likelihood scan along the $\mathcal{B}(\Lambda_b^0 \to \Lambda\gamma)$ parameter. The significance of the signal is extracted from the value of the curve at zero (null hypothesis).
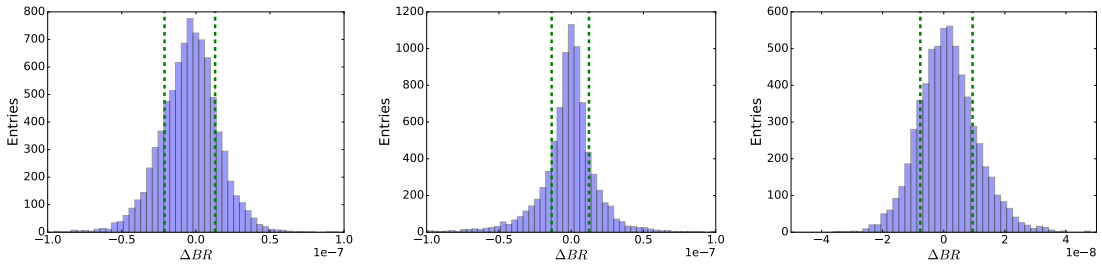

Figure 6.23: Distribution of the difference in the branching ratio measurement obtained from 10000 pseudoexperiments performed to evaluate the systematic effect of the limited precision on the knowledge of the shape parameters of the signal (left), $\Lambda_b^0 \to \Lambda\eta$ background (center) and normalisation (right) invariant mass distributions. The green dashed lines delimit the central region covering a 68% of the distribution.

6.6.1 Fit model

Three different effects are considered related to the particular model employed to fit the data. On one hand, several parameters are fixed in the nominal fit to the values extracted from MC. The finite size of the simulation implies that these values are known within a statistical uncertainty. This effect is evaluated by varying the parameters according to the covariance matrix obtained from the fit to MC. Pseudosamples are generated using the randomised values and then fitted both with the nominal model —this is with these parameters fixed to the values used to fit the data— and with the parameters fixed to the particular set of values used to generate each pseudoexperiment. The difference in the branching ratio obtained with each configuration is computed and the central range covering 68% of the distribution of this quantity for the 10000 pseudoexperiments is assigned as systematic uncertainty. Figure 6.23 shows this distribution when varying the signal, $\Lambda_b^0 \to \Lambda\eta$ and normalisation shape parameters. An uncertainty of $^{+0.5}_{-0.8}\%$, $\pm0.5\%$ and $^{+0.4}_{-0.3}\%$ is assigned for each case. The systematic effects related to the modeling of the background components included in the $K^+\pi^-\gamma$ invariant mass fit were studied in detail in Ref. [42]. From these results a systematic of 0.8% and 0.9% is assigned to the missing pion and $K^+\pi^-\pi^0X$ components, respectively.

On the other hand, the scale factor between the width of the signal and the normalisation mode distributions is fixed to that obtained from MC but differences could arise in data. To account for this effect the fit is repeated leaving this parameter free. A value of $f_\sigma = 1.20 \pm 0.27$ is obtained, which is

67

compatible with the one extracted from MC reported in Table 6.16. Thus no systematic uncertainty is assigned for this effect. Also the $\Lambda_b^0 \to \Lambda\gamma$ and $B^0 \to K^{*0}\gamma$ tail parameters are fixed to the values obtained in MC. Potential differences in data are assessed by repeating the fit with these values free for the normalisation mode —the low statistics does not allow to do the same for the signal. Most of the parameters are found to be significantly different and a reduction of the $B^0 \to K^{*0}\gamma$ yield of 4.9% is observed. We conservatively assume that a change as large as this one could also affect the signal mode and therefore assign this difference as systematic for both the signal significance and the branching ratio measurements. In the latter case the difference in the yield is expected to cancel to some extent in the ratio, but we choose to be conservative. The effect of the variation of the tail parameters within the uncertainty obtained from the fit to MC computed above is already included in this systematic for the signal and normalisation models and thus no extra term will be added for this effect.

Finally, the nominal modeling of the combinatorial background in the $p\pi\gamma$ invariant mass fit is changed to a linear one and the invariant mass fit is repeated with this alternative model. A $\mathcal{B}(\Lambda_b^0 \to \Lambda\gamma) = (2.58 \pm 0.53) \times 10^{-6}$ is obtained and the difference with respect to the nominal fit, 0.4%, is assigned as systematic.

The different sources of uncertainty are independent and thus the total systematic associated to the fit model is computed combining them in quadrature. A value of 5.1% is obtained taking into account all the sources. The significance of the signal is however not affected at first order by systematic effects coming from the modeling of the normalisation mode. Thus considering only the terms related to the $p\pi^-\gamma$ spectra model a systematic of 5.0% is obtained for this measurement. This is the only source of systematic uncertainty affecting the significance of the signal.

6.6.2 Normalisation constant

Several effects are considered as potential source of systematic uncertainty in the evaluation of the normalisation constant: those affecting the ratio of hadronisation fractions, those coming from the precision on the knowledge of the branching fractions of the normalisation mode and the intermediate states and those related to the ratio of efficiencies. Each of them is studied in detail below.

Ratio of hadronisation fractions

The ratio of hadronisation fractions relies on the parametrisation as a function of p_T from Ref. [106]. The uncertainty on the parameters has been propagated to the average $f_{\Lambda_b^0}/f_{B^0}$ in Section 6.4.1. On top of this, another source of uncertainty is considered: the fact that the generated p_T distribution of the Λ_b^0 in simulation is used to extract the average hadronisation ratio. The limitation in the knowledge of this distribution is assessed by re-weighting it using the corrections obtained from $\Lambda_b^0 \to pK^-J/\psi$ in Section 6.3.4. The difference in the $f_{\Lambda_b^0}/f_{B^0}$ average, 0.012, is considered as a systematic too. The two sources of error are independent and thus combined in quadrature to obtain a total systematic uncertainty associated to $f_{\Lambda_b^0}/f_{B^0}$ of 0.056. This is a relative error of 12.8% and represents the largest systematic uncertainty.

Branching fractions

The precision on the knowledge of $\mathcal{B}(B^0 \to K^{*0}\gamma)$, $\mathcal{B}(\Lambda \to p\pi^-)$ and $\mathcal{B}(K^{*0} \to K^+\pi^-)$ from [51] is combined in quadrature and a total uncertainty of 3.5% is obtained, dominated by the precision on the measurement of $\mathcal{B}(B^0 \to K^{*0}\gamma)$.

Efficiency ratio

The uncertainty associated to the finite size of the MC samples used to extract the ratio of efficiencies has been obtained in Sec. 6.4.3. Other systematic uncertainties arise from various components of the efficiency ratio that are studied separately. It is important to emphasise that although large uncertainties
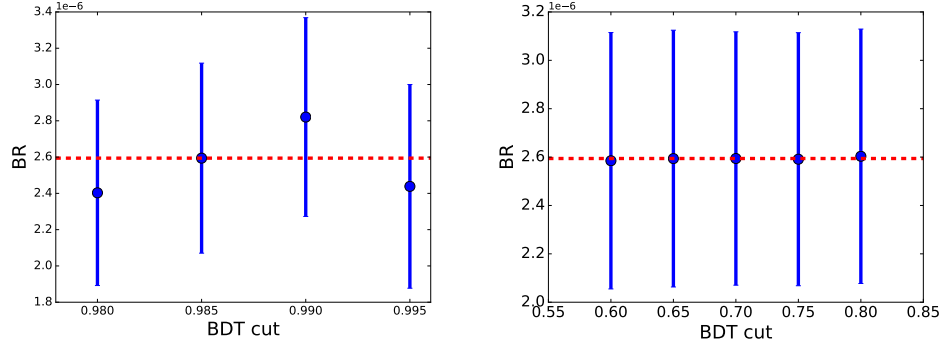
Figure 6.24: Measured value of $\mathcal{B}(\Lambda_b^0 \to \Lambda\gamma)$ as a function of the requirement on the BDT output selecting the signal (left) and normalisation (right) modes.

can affect the extraction of absolute efficiencies for some terms, the measured $\mathcal{B}(\Lambda_b^0 \to \Lambda\gamma)$ depends only on the ratio of efficiencies and thus many effects are expected to cancel.

Charged PID efficiency   It has been obtained from data-driven techniques using calibration samples. The PID group recommends to assign a 0.1% systematic effect per track associated to the background subtraction method employed to obtain pure samples [109]. In this analysis PID cuts are applied to two tracks in each decay and then the ratio is evaluated. Since both modes contain a pion we consider the uncertainty in each mode to be correlated and obtain a total systematic associated to this effect of 0.28%. This is a conservative approach since due to the correlations some effects may cancel in the ratio. Moreover the average efficiency for the decays of interest has been obtained relying on the assumption that the efficiency extracted from a given kinematic bin in the calibration sample is a good estimate of the efficiency in the same bin for the decay under study. This property depends on the employed binning scheme and any possible systematic effect that this choice could introduce is evaluated by repeating the calculation with a different one. We choose a new binning with twice as many intervals and compute the ratio of efficiencies between the signal and the normalisation mode with this new configuration. A difference with respect to the nominal ratio of 0.26% is obtained and assigned as systematic. Since both sources of uncertainty are independent, they are added in quadrature to obtain a total of 0.39%.

Data/simulation differences   Potential systematic effects arising from residual data/MC differences are assessed by varying the requirement on the output of the BDT. The normalisation constant is re-computed at each point and the fit to data repeated to obtain an alternative measurement of the $\mathcal{B}(\Lambda_b^0 \to \Lambda\gamma)$. This is done independently for the BDT selecting the signal and the normalisation modes and the results are shown in Fig. 6.24. While changing the requirement on the BDT selecting $B^0 \to K^{*0}\gamma$ candidates gives no difference in the the measurement of $\mathcal{B}(\Lambda_b^0 \to \Lambda\gamma)$, deviations are observed when varying the signal BDT. The largest difference to the nominal result, 2.3×10^7, is assigned as systematic. This represents a relative uncertainty of 8.7%. This estimation is conservative since part of the differences could arise from possible fluctuations of the fit.

Neutral PID efficiency   The ratio of neutral PID efficiencies has been obtained from simulation in Section 6.4.3. However it was found in Ref. [66] that the distribution of the `IsPhoton` variable in data is not well reproduced by the MC. In particular a dependency with the photon E_{T} and η was observed. A tool is provided in the same reference to extract the efficiency from data-driven techniques but unfortunately calibration samples of photons in Run 2 conditions are not yet available. Thus we try to evaluate this effect by other means. Due to the similar kinematics between the signal and normalisation
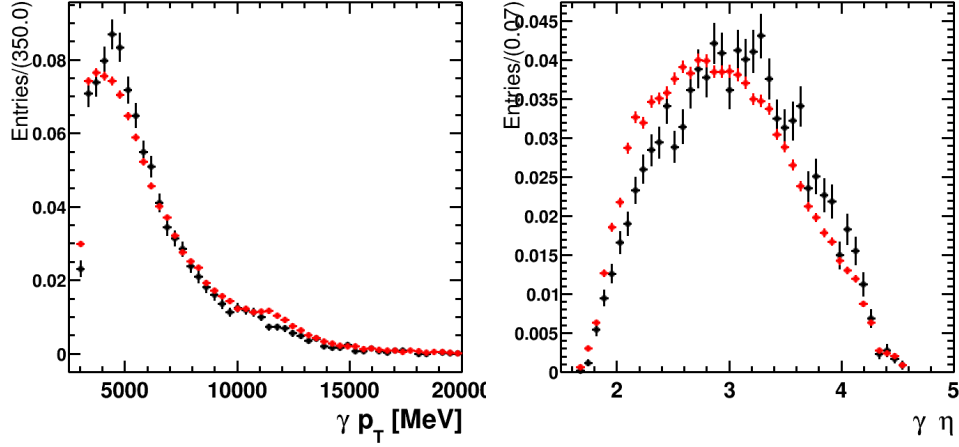
Figure 6.25: Distributions of γ E_{T} (left) and η (right) for $\Lambda_b^0 \to \Lambda\gamma$ (black) and $B^0 \to K^{*0}\gamma$ (red) candidates without the neutral PID requirement.

modes, differences between data and MC are expected to cancel at first order in the efficiency ratio. To cross-check this hypothesis, the E_{T} and η signal and normalisation distributions for candidates selected without applying a requirement on the neutral PID are compared in Figure 6.25. Although a good agreement is found, small discrepancies are observed. In order to assess their effect the Run 1 calibration sample is used to extract the ratio of efficiencies from data using the tool developed in Ref. [66]. Similarly to the charged PID strategy, the tool relies on the assumption that the efficiency of any cut is constant in a given bin of E_{T} and η. The efficiency in each bin is obtained from the calibration sample and the kinematics of the decay of interest given by the MC are used to obtain the average efficiency. We follow this technique using the Run 1 calibration data and the Run 2 MC samples for the signal and normalisation modes. The ratio of efficiencies obtained from this technique is compared to the one extracted from MC and they are found to be in good agreement, $r_\epsilon^{\mathrm{MC}}/r_\epsilon^{\mathrm{data}} = 1.0025 \pm 0.0050$. Thus no systematic is assigned to this term.

Trigger efficiency Systematic uncertainties in the ratio of trigger efficiencies could arise from various sources. The L0 requirement is equal for both modes and superseded by tighter offline cuts on the E_{T} of the photon. However the efficiency of the L0 requirement on top of offline selected candidates is found to be smaller than 1, $\epsilon_{L0} = (93.8 \pm 0.5)\%$ and $\epsilon_{L0} = (93.7 \pm 0.5)\%$ for the signal and normalisation modes, respectively. In order to understand this effect, the difference between the transverse energy as measured by the L0 and offline is shown in Fig. 6.26 for offline selected events in the MC samples that satisfy the L0 photon condition. One can observe that the L0 tends to measure smaller energies with worse resolution —a bias of around 400 MeV with a width of 200 MeV can be seen. Only for a small fraction of the events the energy measured by the L0 is larger causing the efficiency of this requirement to be lower than 1 as observed. The differences in the energy measurements are understood by the different cluster definition at both stages —clusters of 2x2 cells are built at L0 [115] while 3x3 cell clusters are reconstructed offline [116]. Since the effect is observed to be small and of compatible size between the signal and normalisation modes, no systematic is assigned to the L0 efficiency. Potential differences between MC and data are also assumed to cancel in the ratio, since the E_{T} spectra are very similar.

The HLT1 requirement is also the same for the signal and normalisation modes and the HLT2 and the BDT discriminant use the same information to apply a tight selection. Therefore potential systematic effects are already taken into account. Moreover, potential misalignments between the trigger and the BDT requirements are expected to cancel to a good extent in the ratio. Residual differences could only
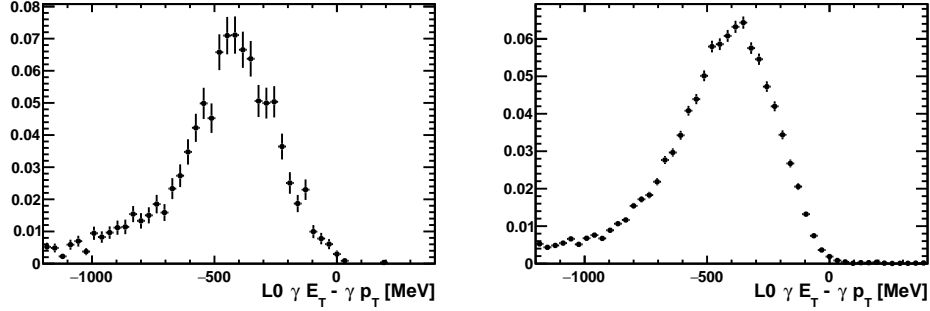
Figure 6.26: Distributions of the difference between the photon E_{T} as measured by L0 and offline for selected $\Lambda_b^0 \to \Lambda\gamma$ (left) and $B^0 \to K^{*0}\gamma$ (right) MC candidates satisfying the L0 photon requirement.

arise from MC mismodeling being significantly different for the signal and the normalisation modes. This is expected to be a second order effect and is thus neglected. The same arguments apply to the exclusive HLT2 selection triggering signal candidates, whose requirements have been applied offline to the normalisation mode.

The inclusive radiative HLT2 requirement is on the contrary only applied to $B^0 \to K^{*0}\gamma$ candidates and consequently potential discrepancies between MC and data could affect the result. In order to assess this effect, the TISTOS method [117] is used to compute the efficiency of this selection from data. This technique is based on the extraction of a trigger unbiased data sample from which the efficiency of a given requirement can be computed as the number of selected events over the total one. This counting cannot be done directly on offline selected candidates because they have actually already passed some trigger selection —otherwise they would not have been recorded in the first place. Thus the sample is biased. The TISTOS method proposes to apply a TIS requirement on offline candidates to get a trigger unbiased sample, up to a dependency on the parent momenta. Here TIS states for Trigger Independent of Signal and a trigger decision is defined to be TIS on a candidate when the candidate components —hits, tracks, neutral objects— are not needed for the trigger to fire. In other words, the trigger would fire for that event if the signal was not present, i.e. it is independent of it. To estimate the efficiency of the radiative inclusive selection, an HLT2 TIS requirement is first applied on offline selected candidates satisfying the L0 and HLT1 cuts. The candidates are fit using the nominal mass model to obtain the number of signal events in the TIS sample. Then the HLT2 inclusive selection is applied and the remaining candidates are fit again with the same model to extract the signal yield in the TISTOS sample. The efficiency obtained with this method is compatible with the one computed from MC and thus no systematic is added.

6.6.3 Summary of uncertainties

All the uncertainties computed above are assumed to be independent at first order and thus added in quadrature to obtain a total systematic uncertainty on the branching ratio measurement of 16.8%. As previously mentioned, only the signal fit model can affect the measured statistical significance. The systematic uncertainty on this value is found to be 5.0%.

The various contributions and the total systematic uncertainty on the measurement of $\mathcal{B}(\Lambda_b^0 \to \Lambda\gamma)$ are summarised in Table 6.24. Most uncertainties are negligible compared to the statistical one, only the one coming from the ratio of hadronisation fractions is comparable. This systematic will be reduced when a more precise measurement of this quantity is available. Additionally one could get rid of this contribution by choosing a normalisation mode from a Λ_b^0 decay. An interesting candidate for such a measurement is $\Lambda_b^0 \to \Lambda J/\psi$, but the differences in the reconstruction and selection between photons and J/ψ should be carefully controlled. Moreover such a normalisation would also cancel potential differences in the reconstruction and selection of Λ and K^{*0}, which have not been considered in the current analysis,

71

Table 6.24: Dominant systematic uncertainties on the measurement of $\mathcal{B}(\Lambda_b^0 \to \Lambda\gamma)$.

Source	Value (%)
$f_{\Lambda_b^0}/f_{B^0}$	12.8
BDT	8.7
$\mathcal{B}$	3.5
Fit model	5.1
Efficiency ratio	1.7
Total	16.8
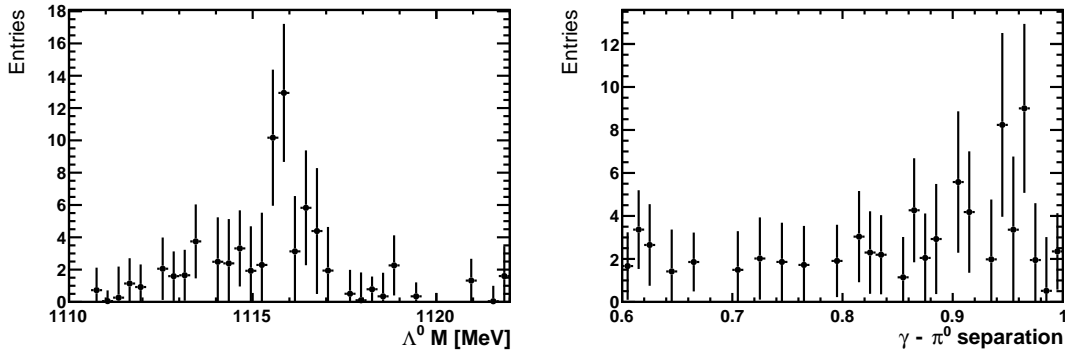
Figure 6.27: Signal distributions in data for the $p\pi^-$ invariant mass (left) and the γ-π^0 separation variable (right) obtained using the *sPlot* technique.

but would remove potential cancellations on the photon systematics. A solution to deal with both at the same time is proposed in Sec. 6.8.

6.7 Results

The invariant mass fit presented in Sec. 6.5 provides a measurement of the $\mathcal{B}(\Lambda_b^0 \to \Lambda\gamma)$ and the signal significance in the analysed data sample. Systematic uncertainties affecting these results have been studied in detail in the above. We shall perform in this section further cross-checks and present the final results.

6.7.1 Cross-checks

As a cross-check the $p\pi^-$ invariant mass distribution in data is plotted for the signal using the *sPlot* technique [100], which consists on weighting the events according to the probability that they belong to the signal category as obtained from the invariant mass fit. This distribution is presented in Fig. 6.27 (left) showing a clear Λ peak as expected. No peaks from potential misidentified backgrounds are observed.

The same statistical technique is used to plot the γ/π^0 separation variable for the signal component as shown in Fig. 6.27 (right). The distribution peaks at zero as expected for photons confirming no large contamination from π^0 is present in the data.

6.7.2 Signal significance

The statistical significance for the signal has been obtained from the scan of the likelihood profile on data and a systematic uncertainty of 5.0% coming from the fit model has been estimated to affect this

measurement. Since the systematic error is much smaller than the statistical one, the shape of the likelihood is not expected to be distorted and the combined significance can be directly obtained as:

$$s = \frac{s_{\text{stat}}}{\sqrt{1 + \left(\frac{\sigma_{\text{syst}}}{\sigma_{\text{stat}}}\right)^2}} \qquad (6.26)$$

where σ_{stat} and σ_{syst} are the statistical and systematic uncertainties, respectively. Combining the values obtained in Section 6.5 and 6.6 a combined significance of

$$s = 5.5$$

is measured. This represents the first observation of the $\Lambda_b^0 \to \Lambda\gamma$ decay mode and opens the doors to further studies exploiting this channel, such as the measurement of the photon polarisation from the angular distribution of the final state particles as detailed in Chapter 2.

6.7.3 Branching ratio

The branching ratio of the $\Lambda_b^0 \to \Lambda\gamma$ decay has been obtained from the fit to data in Section 6.5. This result is combined with the systematic uncertainties computed in the previous section to obtain the final result:

$$\mathcal{B}(\Lambda_b^0 \to \Lambda\gamma) = (2.59 \pm 0.52(\text{stat.}) \pm 0.28(\text{syst.}) \pm 0.33(f_{\Lambda_b^0}/f_{B^0})) \times 10^{-6}$$

where the first uncertainty is statistical, the second is systematic and the third is the systematic associated to the ratio of hadronisation fractions. LHCb has recorded new data in 2017, corresponding to an integrated luminosity of $1.7\,\text{fb}^{-1}$, which will be soon available for analysis allowing an improvement of the statistical precision.

The dominant systematic uncertainty affecting the measurement of the branching ratio comes from the limited knowledge on the ratio of hadronisation fractions between Λ_b^0 and B^0. An updated measurement of this quantity would help improve the precision in our results. Moreover no analysis has yet studied this ratio in pp collisions at $13\,\text{TeV}$. To obtain the results quoted above we have assumed that the measurements available at $7\,\text{TeV}$ can be used at higher energies but this has not been confirmed by experiments yet. In order to provide a result that is not affected by this uncertainty the quantity $\mathcal{B}(\Lambda_b^0 \to \Lambda\gamma) \times f_{\Lambda_b^0}/f_{B^0}$ is also measured. A new normalisation constant is computed dropping this term from Eq. 6.7 and the fit is repeated with the obtained value. The remaining systematic uncertainties are propagated to this new observable to obtain the final measurement:

$$\mathcal{B}(\Lambda_b^0 \to \Lambda\gamma) \times \frac{f_{\Lambda_b^0}}{f_{B^0}} = (1.28 \pm 0.26(\text{stat.}) \pm 0.14(\text{syst.})) \times 10^{-6}$$

This result can be used to obtain a more precise value of $\mathcal{B}(\Lambda_b^0 \to \Lambda\gamma)$ when an updated measurement of the ratio of hadronisation fractions becomes available.

Another limitation of the current analysis lies in the modeling of the $B^0 \to K^{*0}\gamma$ backgrounds, since dedicated studies could not have been performed due to the lack of simulation samples in Run 2 conditions for the relevant modes. In particular, peaking backgrounds, whose yield cannot be extracted from the fit to data since they lie right under the signal, have not been included in our model and this can have an impact on the result. In Ref. [42] contaminations of 2.05, 2.04, 1.4, 0.24 and 0.15% from $B^0 \to K^+\pi^-\pi^0$, $B^0 \to K^{*0}\eta$, $\Lambda_b^0 \to \Lambda^*\gamma$, $B_s^0 \to \phi\gamma$ and $B^0 \to \rho^0\gamma$, respectively, were estimated. Assuming the same contaminations in our analysis, despite the different reconstruction and selections, the effective $B^0 \to K^{*0}\gamma$ yield would be reduced by a 5.8%, with a direct impact on the branching ratio measurement, which would be enhanced by the same amount, yielding to a value of $\mathcal{B}(\Lambda_b^0 \to \Lambda\gamma) = (2.75 \pm 0.55 \pm 0.30 \pm 0.35) \times 10^{-6}$. This result is still within the statistical uncertainty but more detailed studies will be performed when the samples become available.

6.8   Conclusions and future prospects

A search for the previously unobserved $\Lambda_b^0 \to \Lambda\gamma$ decay has been performed using the data collected by the LHCb experiment in 2016, corresponding to an integrated luminosity of $1.6\,\text{fb}^{-1}$. Dedicated trigger and offline algorithms have been developed and exploited to reconstruct and select the candidates overcoming the particularly challenging topology of this decay. In particular, a BDT with large discrimination power has been trained to reduce the huge combinatorial background.

After the full selection, the invariant mass distribution of the candidates is fitted to disentangle the signal component. A signal yield of (64 ± 13) events is observed, with a signal significance of 5.5σ. This represents the first observation of this decay mode.

Moreover the $B^0 \to K^{*0}\gamma$ mode is used as normalisation channel to extract the branching ratio of the signal decay. A value of $\mathcal{B}(\Lambda_b^0 \to \Lambda\gamma) = (2.59\pm0.52(\text{stat.})\pm0.28(\text{syst.})\pm0.33(f_{\Lambda_b^0}/f_{B^0}))\times10^{-6}$ is measured. A measurement independent of the ratio of hadronisation fractions, which is the dominant systematic uncertainty and has not yet been measured with $13\,\text{TeV}$ data, is found to be $\mathcal{B}(\Lambda_b^0 \to \Lambda\gamma) \times f_{\Lambda_b^0}/f_{B^0} = (1.28 \pm 0.26(\text{stat.}) \pm 0.14(\text{syst.})) \times 10^{-6}$. This quantity can be used to obtain a new measurement of the $\mathcal{B}(\Lambda_b^0 \to \Lambda\gamma)$ when an updated value of the ratio of hadronisation fractions becomes available.

This analysis provides the first observation of the $\Lambda_b^0 \to \Lambda\gamma$ decay and opens the doors to the exploitation of this mode for further measurements. Of particular interest is the polarisation of the emitted photon, which provides a null test of the SM, and can be accessed in this decay through an angular analysis. Taking into account the observed yield, around 200 signal events will be recorded by the end of the Run 2 of the LHC, which should allow to measure the photon polarisation with an accuracy of around 20%, as obtained from preliminary studies [118]. A proof of concept study can be performed earlier using the dataset analysed in this study together with the data recorded by LHCb during 2017, which shall be soon available for analysis. Much larger statistics will be available during the upgrade phase of LHCb—scheduled between 2021 and 2024— allowing the measurement of the photon polarisation to be further improved. At this stage a CP measurement of this quantity would be feasible exploiting the self-tagging power of the decay and would provide a test of the structure of potential new physics models. A measurement of the direct CP asymmetry in this mode could be performed much sooner but its sensitivity to beyond the SM effects is limited by the existing results of similar measurements in other $b \to s\gamma$ transitions.

The study reported in this chapter also provides the first measurement of the branching fraction of this decay. Although several sources of systematic uncertainty have been studied further checks would be desirable. In particular we have assumed throughout the analysis that the simulation reproduces properly the reconstruction and selection of long-lived particles such as Λ. A cross-check of this assumption could be performed by repeating the measurement considering the $\Lambda_b^0 \to \Lambda J/\psi$ mode as control channel. In this case any mis-modelling of the hadronic part of the decay would cancel in the ratio. Special care would be required however with the differences between the photon and J/ψ reconstruction. A solution for both issues could consist on exploiting a double ratio of decay modes including also the $B^0 \to K^{*0}J/\psi$ decay. In this approach all the terms entering in the efficiency calculation can be paired in such a way that systematic uncertainties cancel in the ratio of all the modes. Such a measurement would provide a cleaner extraction of the $\mathcal{B}(\Lambda_b^0 \to \Lambda\gamma)$.

Further improvements to the analysis presented here could be achieved with more sophisticated strategies for the reconstruction of the signal candidates. Complementary approaches have been considered and explored in detail in Ref. [119]. The largest potential improvement would be the inclusion of downstream tracks in the reconstruction of the Λ daughters since due to its large life-time this particle decays most of the time outside the LHCb VELO. More precisely, around 80% of the simulated events are reconstructed from downstream tracks. Unfortunately in this case the worse momentum resolution does not allow for signal and background separation. Information on the Λ_b^0 decay vertex would be even more crucial for this approach. Consequently, an alternative reconstruction has been explored consisting on globally fitting the full decay chain in order to obtain the photon direction and the Λ_b^0 decay vertex following the method proposed in Ref. [120]. The results in Ref. [119] show that this technique is very promising for this decay but there are still some reconstruction issues to be understood.

Another approach consists on exploiting photon conversion to a di-electron pair in the detector material. In this case, the photon is reconstructed from two tracks and thus its momentum can be obtained with precision and the Λ_b^0 decay vertex reconstructed. However, only around 20% of the photons at LHCb decay before the magnet and the reconstruction efficiency for those is around 30% [121], so the effective statistics are much lower. This option is particularly interesting in combination with the reconstruction of the Λ from downstream tracks since the information from the SV should provide a larger signal to background discrimination and the lower proportion of converted photons would be compensated to some extent by the larger amount of reconstructed Λ decays. This option is complementary to the one developed in this analysis and thus it should be further explored in the future. However it would require the development of a new trigger selection to exploit the downstream tracks, so such an analysis might not be feasible until the LHCb upgrade.

Chapter 7

Conclusions

This document has presented my contributions to the expansion of the LHCb rare decays program in two areas: radiative beauty and rare strange decays. Both are examples of flavour-changing neutral-currents appearing in the Standard Model only at loop order, which makes them very sensitive to potential new particles entering the loop and therefore an ideal benchmark to probe New Physics.

On one hand, radiative decays share the particular feature of the presence of a high energetic photon in the final state. Therefore, a key point on the study of these modes is the availability of dedicated selections at trigger level that allow to extract sizeable signal samples from the huge background produced in pp collisions at the LHC. An inclusive dedicated selection has been developed for the Run 2 of LHCb taking advantage of the common properties of these decays and the separation power provided by state-of-the-art multivariate techniques. For modes previously studied at LHCb, up to 20% absolute improvements in the trigger efficiencies have been achieved. Furthermore, for other decay topologies such as $B^0 \to K^+\pi^-\gamma$ and $B^+ \to K^{*+}\gamma$, which were poorly triggered in the past, efficiencies of 96% and 73%, respectively, have been reached, allowing the future exploitation of these modes for physics analyses. At the same time, the total rate of the inclusive radiative trigger has been reduced by a factor 2 with respect the Run 1 configuration, allowing to allocate the remaining budget to the exclusive selection of decays that require a special reconstruction, expanding even more the radiative decays program.

An example of such a decay is the baryonic $\Lambda_b^0 \to \Lambda\gamma$, where due to the long life-time of the Λ and the lack on information of the photon direction provided by the LHCb calorimeter system, the Λ_b^0 decay vertex cannot be directly reconstructed. The introduction of a special reconstruction for this mode in the Run 2 trigger has allowed to perform a search for this previously unobserved decay using the 2016 LHCb dataset. A signal yield of (64 ± 13) events with a significance of 5.5σ, including systematic uncertainties, has been obtained leading to the first observation of this mode. This achievement opens the doors to the study of interesting properties of this decay, such as the angular distribution of the final state particles that gives access to the photon polarisation observable, which can be used to test the Standard Model and constraint New Physics scenarios. Moreover, the branching ratio of this mode has been measured to be

$$\mathcal{B}(\Lambda_b^0 \to \Lambda\gamma) = (2.59 \pm 0.52(\text{stat.}) \pm 0.28(\text{syst.}) \pm 0.33(f_{\Lambda_b^0}/f_{B^0})) \times 10^{-6}$$

where the first uncertainty is statistical and the rest are systematic. The latter is dominated by the knowledge of the ratio of hadronisation fractions, which is also limited by the absence of a measure of this quantity in pp collisions at a centre of mass energy of 13 TeV. Consequently a cleaner observable has been also measured:

$$\mathcal{B}(\Lambda_b^0 \to \Lambda\gamma) \times \frac{f_{\Lambda_b^0}}{f_{B^0}} = (1.28 \pm 0.26 \ (\text{stat.}) \pm 0.14 \ (\text{syst.})) \times 10^{-6}$$

which shall allow to obtain the value of $\mathcal{B}(\Lambda_b^0 \to \Lambda\gamma)$ with larger precision when an updated measurement of $f_{\Lambda_b^0}/f_{B^0}$ becomes available. This study relies on the MC describing accurately potential differences

in the reconstruction and selection of Λ and K^{*0} particles and therefore improvements to deal with this shortcoming been proposed.

On the other hand, LHCb is expanding its rare decays program into the exploration of rare strange modes. Of particular interest are the leptonic $K_\mathrm{S}^0 \to \ell^+\ell^-\ell^+\ell^-$ modes, which are sensitive probes to New Physics effects. In the context of this thesis the feasibility of observing the related and well-known $K_\mathrm{S}^0 \to \pi^+\pi^- e^+ e^-$ decay has been studied using Run 1 data, reaching the conclusion that an observation with this dataset is possible by means of a high-efficiency large-rejection selection, such as a multivariate one. Moreover, dedicated selections have been included in the trigger for Run 2 leading to an expected signal yield of

$$N_\mathrm{Run2}^{exp}(K_\mathrm{S}^0 \to \pi^+\pi^- e^+ e^-) = 620^{+290}_{-120}/\,\mathrm{fb}^{-1}$$

where the error is dominated by the MC statistics. Such a yield should allow a complete study of this mode using Run 2 data and its exploitation in the search for the $K_\mathrm{S}^0 \to \ell^+\ell^-\ell^+\ell^-$ modes, providing a further test of the Standard Model.

To sum up, this thesis has exploited the flexibility of the LHCb trigger to extend the reach of the rare decays physics program in the areas of radiative beauty and rare strange decays, achieving the first observation of the baryonic $\Lambda_b^0 \to \Lambda\gamma$ mode, contributing to the selection of larger signal samples of radiative decays and laying the foundations for the observation of the $K_\mathrm{S}^0 \to \pi^+\pi^- e^+ e^-$ transition at LHCb.

Appendix A

Pull distributions from blind fit in the search for $\Lambda_b^0 \to \Lambda\gamma$
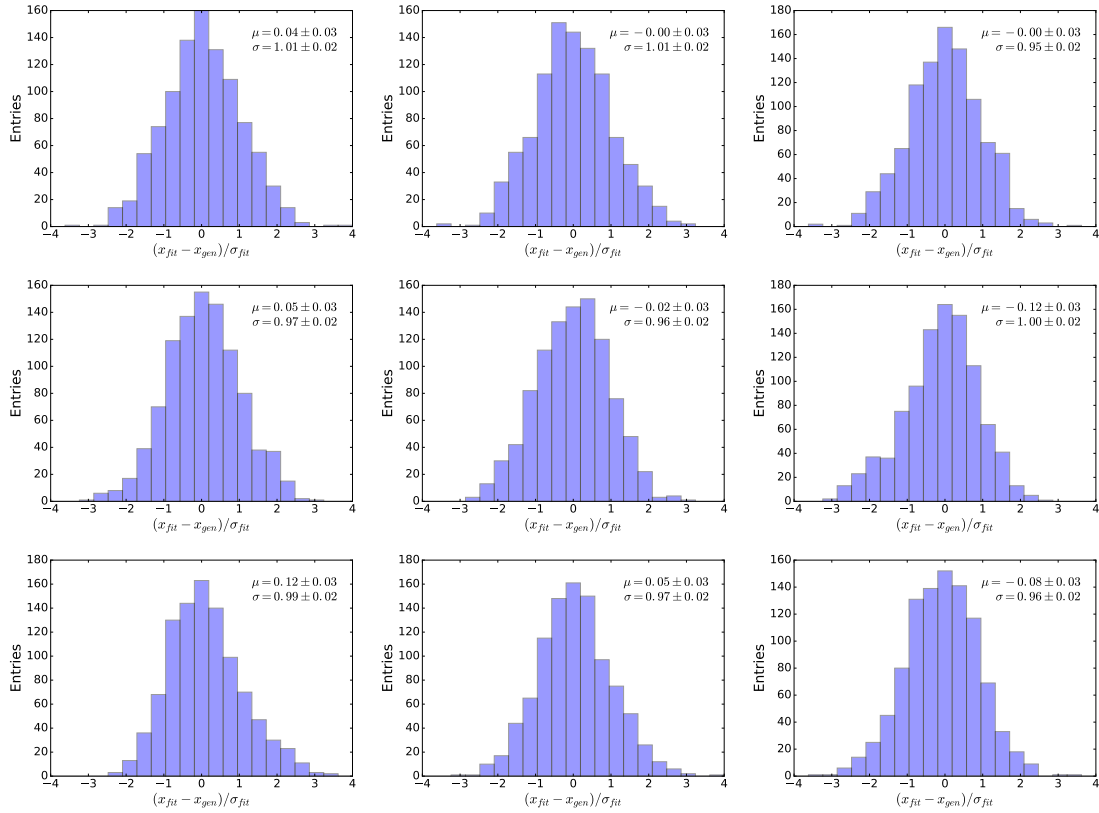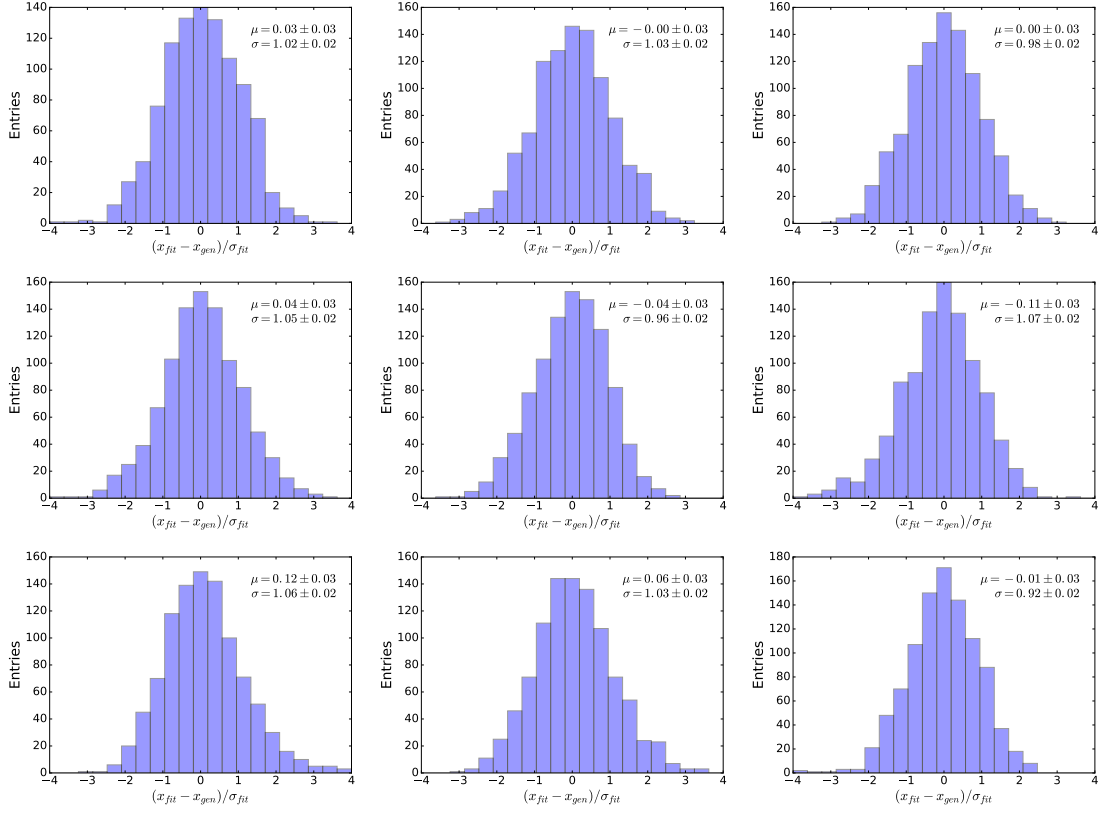

Figure A.1: Pull distributions of the nuisance parameters obtained from 1000 pseudoexperiments generated with the hypothesis $\mathcal{B}(\Lambda_b^0 \to \Lambda\gamma) = \{1 \times 10^{-5}\}$. From top-left to bottom-right the parameters are: $N_{B^0 \to K^{*0}\gamma}$, μ^{Bd}, σ^{Bd}, $\tau_{norm;comb}$, $\tau_{signal;comb}$, $N_{norm;comb}$, $N_{norm;K^+\pi^-\pi^0 X}$, $N_{norm;mis-\pi}$ and $N_{signal;comb}$.
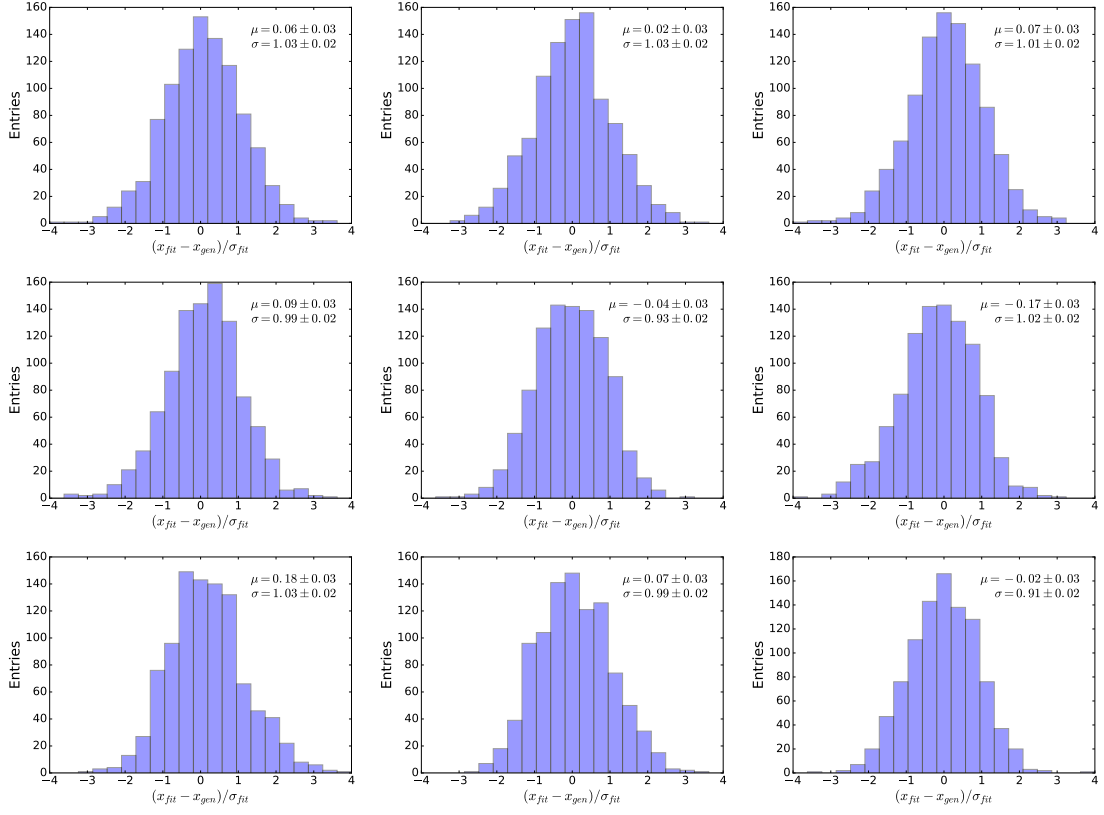
Figure A.2: Pull distributions of the nuisance parameters obtained from 1000 pseudoexperiments generated with the hypothesis $\mathcal{B}(\Lambda_b^0 \to \Lambda\gamma) = \{5 \times 10^{-6}\}$. From top-left to bottom-right the parameters are: $N_{B^0 \to K^{*0}\gamma}$, μ^{Bd}, σ^{Bd}, $\tau_{norm;comb}$, $\tau_{signal;comb}$, $N_{norm;comb}$, $N_{norm;K^+\pi^-\pi^0X}$, $N_{norm;mis-\pi}$ and $N_{signal;comb}$.

Figure A.3: Pull distributions of the nuisance parameters obtained from 1000 pseudoexperiments generated with the hypothesis $\mathcal{B}(\Lambda_b^0 \to \Lambda\gamma) = \{1 \times 10^{-6}\}$. From top-left to bottom-right the parameters are: $N_{B^0 \to K^{*0}\gamma}$, μ^{Bd}, σ^{Bd}, $\tau_{norm;comb}$, $\tau_{signal;comb}$, $N_{norm;comb}$, $N_{norm;K^+\pi^-\pi^0 X}$, $N_{norm;mis-\pi}$ and $N_{signal;comb}$.

Appendix B

Bremsstrahlung recovery in $K_{\mathrm{S}}^0 \to \pi^+\pi^- e^+ e^-$

Electron energy loss due to the emission of Bremsstrahlung photons is recovered at reconstruction level with the association of soft photons to the reconstructed electrons when possible. Details can be found in Ref. [122]. The reconstructed candidate mass distribution may vary depending on the number of photons associated to the electrons in the decay chain. Figure B.1 shows the reconstructed invariant mass distribution for 2012 MC signal and data candidates separated by number of Bremsstrahlung photons associated. Most of the candidates both for MC signal and data have no photons associated. For signal, those candidates that have 1, 2 or more photons associated tend to have larger mass values than the nominal K_{S}^0 mass. This points to a non-efficient energy recovery. Since the electrons in the $K_{\mathrm{S}}^0 \to \pi^+\pi^- e^+ e^-$ decay are very soft, the photons they may emit are even softer. However at LHCb only photons with a transverse momentum larger than $75\,\mathrm{MeV}/c$ are reconstructed. So most of the photons emitted by this soft electrons can not be recovered and those associated to the signal come from other sources and are in general harder. Consequently, there is an excess on the correction energy of those electrons with associated photons. Requiring that no photons are associated to the electrons, the tail at high values in the mass distribution of signal candidates disappears.

The effect of completely removing the Bremsstrahlung recovery is also studied. For this, as a first approach, the momentum of those candidates with associated photons is corrected by subtracting the momentum of the photons. The invariant mass distribution of signal and data candidates after the correction is shown in Fig. B.2. While for background, the effect is negligible, for signal, the high mass tail disappears while the low mass one is broadened, as expected. This is exploited to tighten the mass requirement on the candidates in the HLT2 line described in Sec. 5.6.2. Improvement of the Bremsstrahlung correction for low momentum electrons could benefit future studies on this mode or other K_{S}^0 decays with electrons in the final state.
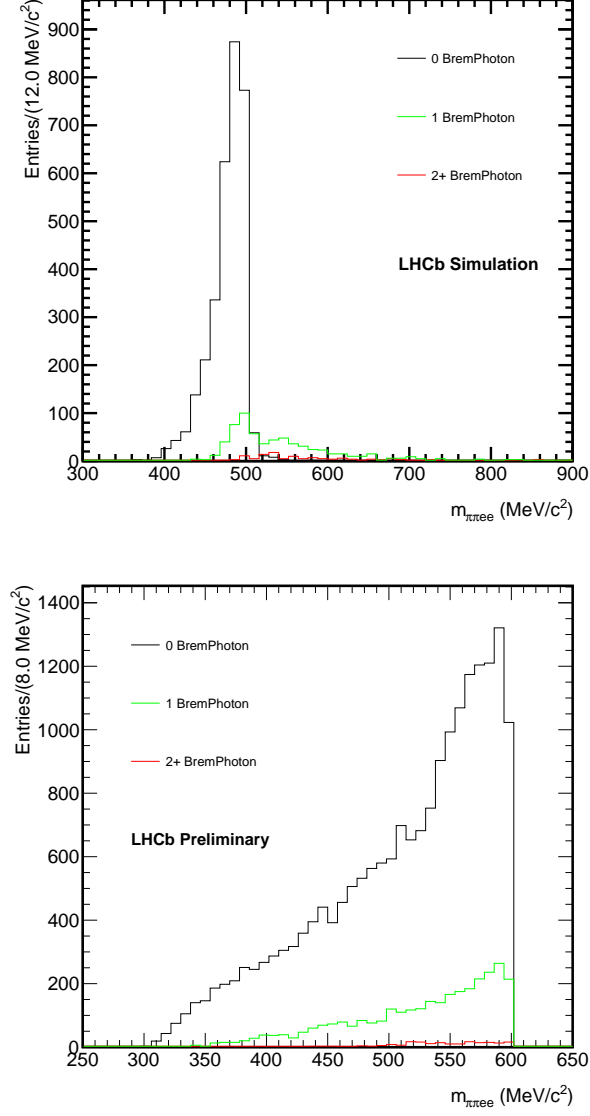
Figure B.1: Invariant mass distributions for MC signal (top) and data (bottom) candidates separated by number of Bremsstrahlung photons associated to the electrons in the decay chain: 0 photons (red), 1 photon (green) and 2 or more photons (black).
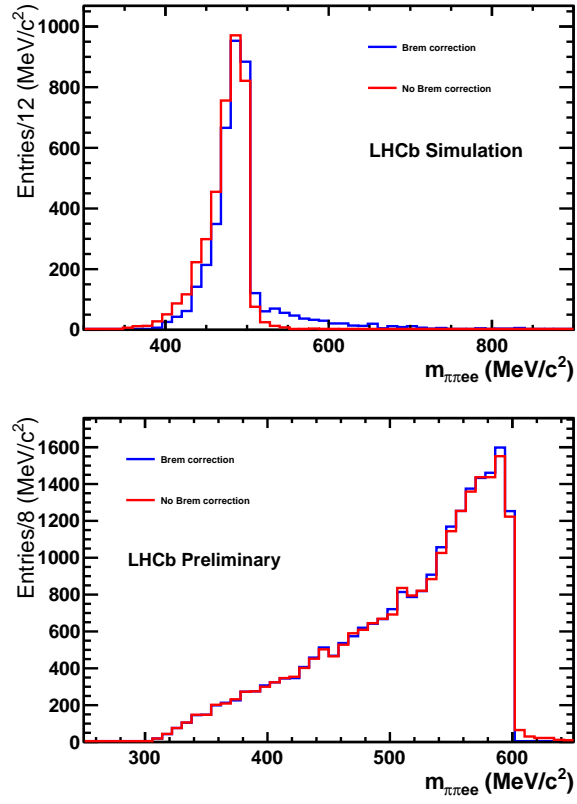
Figure B.2: Invariant mass distributions for MC signal (top) and data (bottom) candidates with the Bremsstrahlung correction applied (blue) and removed (red).

Bibliography

[1] Y. Grossman, *Introduction to flavor physics*, in *Flavianet School on Flavour Physics Karlsruhe, Germany, September 7-18, 2009*, pp. 111–144, 2014. `arXiv:1006.3534`. [73(2014)], doi: 10.5170/CERN-2010-002.111, 10.5170/CERN-2014-003.73.

[2] G. Isidori, *Flavor physics and CP violation*, in *Proceedings, 2012 European School of High-Energy Physics (ESHEP 2012): La Pommeraye, Anjou, France, June 06-19, 2012*, pp. 69–105, 2014. `arXiv:1302.0661`. doi: 10.5170/CERN-2014-008.69.

[3] V. Cirigliano *et al.*, *Kaon Decays in the Standard Model*, Rev. Mod. Phys. **84** (2012) 399, `arXiv:1107.6001`.

[4] A. Paul and D. M. Straub, *Constraints on new physics from radiative B decays*, JHEP **04** (2017) 027, `arXiv:1608.02556`.

[5] W. N. Cottingham and D. A. Greenwood, *An Introduction to the Standard Model of Particle Physics*, Cambridge University Press, 2 ed., 2007. doi: 10.1017/CBO9780511791406.

[6] C. S. Wu *et al.*, *Experimental test of parity conservation in beta decay*, Phys. Rev. **105** (1957) 1413.

[7] F. Englert and R. Brout, *Broken symmetry and the mass of gauge vector mesons*, Phys. Rev. Lett. **13** (1964) 321.

[8] P. W. Higgs, *Broken symmetries and the masses of gauge bosons*, Phys. Rev. Lett. **13** (1964) 508.

[9] G. S. Guralnik, C. R. Hagen, and T. W. B. Kibble, *Global conservation laws and massless particles*, Phys. Rev. Lett. **13** (1964) 585.

[10] ATLAS collaboration, G. Aad *et al.*, *Observation of a new particle in the search for the Standard Model Higgs boson with the ATLAS detector at the LHC*, Phys. Lett. **B716** (2012) 1, `arXiv:1207.7214`.

[11] CMS collaboration, S. Chatrchyan *et al.*, *Observation of a new boson at a mass of 125 GeV with the CMS experiment at the LHC*, Phys. Lett. **B716** (2012) 30, `arXiv:1207.7235`.

[12] R. Bouchendira *et al.*, *New determination of the fine structure constant and test of the quantum electrodynamics*, Phys. Rev. Lett. **106** (2011) 080801, `arXiv:1012.3627`.

[13] UA2, P. Bagnaia *et al.*, *Evidence for $Z \to e^+ e^-$ at the CERN anti-p p Collider*, Phys. Lett. **129B** (1983) 130.

[14] CDF collaboration, F. Abe *et al.*, *Observation of top quark production in $\bar{p}p$ collisions*, Phys. Rev. Lett. **74** (1995) 2626, `arXiv:hep-ex/9503002`.

[15] E598 collaboration, J. J. Aubert *et al.*, *Experimental Observation of a Heavy Particle J*, Phys. Rev. Lett. **33** (1974) 1404.

[16] N. Cabibbo, *Unitary symmetry and leptonic decays*, Phys. Rev. Lett. **10** (1963) 531.

[17] M. Kobayashi and T. Maskawa, *CP Violation in the Renormalizable Theory of Weak Interaction*, Prog. Theor. Phys. **49** (1973) 652.

[18] L. Wolfenstein, *Parametrization of the Kobayashi-Maskawa Matrix*, Phys. Rev. Lett. **51** (1983) 1945.

[19] S. Descotes-Genon and P. Koppenburg, *The CKM Parameters*, Ann. Rev. Nucl. Part. Sci. **67** (2017) 97, `arXiv:1702.08834`.

[20] LHCb collaboration, B. Adeva *et al.*, *Road map for selected key measurements from LHCb.*, Tech. Rep. arXiv:0912.4179. CERN-LHCb-PUB-2009-029, CERN, Geneva, May, 2010. Comments: 379 pages.

[21] S. L. Glashow, J. Iliopoulos, and L. Maiani, *Weak interactions with lepton-hadron symmetry*, Phys. Rev. D **2** (1970) 1285.

[22] K. G. Wilson, *Non-lagrangian models of current algebra*, Phys. Rev. **179** (1969) 1499.

[23] A. J. Buras, *Weak Hamiltonian, CP violation and rare decays*, in *Probing the standard model of particle interactions. Proceedings, Summer School in Theoretical Physics, NATO Advanced Study Institute, 68th session, Les Houches, France, July 28-September 5, 1997. Pt. 1, 2*, pp. 281–539, 1998. `arXiv:hep-ph/9806471`.

[24] G. Buchalla, A. J. Buras, and M. E. Lautenbacher, *Weak decays beyond leading logarithms*, Rev. Mod. Phys. **68** (1996) 1125, `arXiv:hep-ph/9512380`.

[25] G. D'Ambrosio, D. Greynat, and G. Vulvert, *Standard Model and New Physics contributions to K_L and K_S into four leptons*, Eur. Phys. J. **C73** (2013), no. 12 2678, `arXiv:1309.5736`.

[26] KTeV collaboration, A. Alavi-Harati *et al.*, *Measurements of the rare decay $K_L \to e^+e^-e^+e^-$*, Phys. Rev. Lett. **86** (2001) 5425, `arXiv:hep-ex/0104043`.

[27] NA48 collaboration, A. Lai *et al.*, *Measurement of the $K_L \to e^+e^-e^+e^-$ Decay Rate*, `arXiv:hep-ex/0006040arXiv:hep-ex/0006040`, [Phys. Lett.B615,31(2005)].

[28] KTeV collaboration, A. Alavi-Harati *et al.*, *Measurements of the decay $K_L^0 \to e^+e^-\mu^+\mu^-$*, Phys. Rev. Lett. **90** (2003) 141801, `arXiv:hep-ex/0212002`.

[29] LHCb collaboration, R. Aaij *et al.*, *Improved limit on the branching fraction of the rare decay $K_S^0 \to \mu\mu$*, Eur. Phys. J. **C77** (2017) 678, `arXiv:1706.00758`.

[30] LHCb collaboration, R. Aaij *et al.*, *Evidence for the rare decay $\Sigma^+ \to p\mu^+\mu^-$*, LHCb-PAPER-2017-049, CERN-EP-2017-319, in preparation.

[31] G. Hiller and A. Kagan, *Probing for new physics in polarized Λ_b decays at the Z*, Phys. Rev. **D65** (2002) 074038, `arXiv:hep-ph/0108074`.

[32] D. Atwood, M. Gronau, and A. Soni, *Mixing induced CP asymmetries in radiative B decays in and beyond the standard model*, Phys. Rev. Lett. **79** (1997) 185, `arXiv:hep-ph/9704272`.

[33] BaBar collaboration, B. Aubert *et al.*, *Measurement of Branching Fractions and CP and Isospin Asymmetries in $B \to K^*(892)\gamma$ Decays*, Phys. Rev. Lett. **103** (2009) 211802, `arXiv:0906.2177`.

[34] BaBar collaboration, P. del Amo Sanchez *et al.*, *Time-dependent analysis of $B^0 \to K_S^0\pi^-\pi^+\gamma$ decays and studies of the $K^+\pi^-\pi^+$ system in $B^+ \to K^+\pi^-\pi^+\gamma$ decays*, Phys. Rev. **D93** (2016), no. 5 052013, `arXiv:1512.03579`.

[35] Belle collaboration, D. Dutta *et al.*, *Search for $B_s^0 \to \gamma\gamma$ and a measurement of the branching fraction for $B_s^0 \to \phi\gamma$*, Phys. Rev. **D91** (2015), no. 1 011101, `arXiv:1411.7771`.

[36] LHCb collaboration, R. Aaij *et al.*, *Measurement of the ratio of branching fractions $\mathcal{B}(B^0 \to K^{*0}\gamma)/\mathcal{B}(B_s^0 \to \phi\gamma)$ and the direct CP asymmetry in $B^0 \to K^{*0}\gamma$*, Nucl. Phys. **B867** (2013) 1, `arXiv:1209.0313`.

[37] D. Melikhov, N. Nikitin, and S. Simula, *Probing right-handed currents in $B^0 \to K^{*0}\ell^+\ell^-$ transitions*, Phys. Lett. **B442** (1998) 381, `arXiv:hep-ph/9807464`.

[38] Y. Grossman and D. Pirjol, *Extracting and using photon polarization information in radiative B decays*, JHEP **06** (2000) 029, `arXiv:hep-ph/0005069`.

[39] M. Gronau, Y. Grossman, D. Pirjol, and A. Ryd, *Measuring the photon polarization in $B^0 \to K\pi\pi\gamma$*, Phys. Rev. Lett. **88** (2002) 051802, `arXiv:hep-ph/0107254`.

[40] LHCb collaboration, R. Aaij *et al.*, *Observation of photon polarization in the $b \to s\gamma$ transition*, Phys. Rev. Lett. **112** (2014) 161801, `arXiv:1402.6852`.

[41] LHCb collaboration, R. Aaij *et al.*, *Angular analysis of the $B^0 \to K^* e^+ e^-$ decay in the low-q^2 region*, JHEP **04** (2015) 064, `arXiv:1501.03038`.

[42] LHCb collaboration, R. Aaij *et al.*, *First experimental study of photon polarization in radiative B_s^0 decays*, Phys. Rev. Lett. **118** (2017) 021801, `arXiv:1609.02032`.

[43] CDF collaboration, D. e. a. Acosta, *Search for radiative b-hadron decays in $p\overline{p}$ collisions at $\sqrt{s} = 1.8$TeV*, Phys. Rev. D **66** (2002) 112002.

[44] T. Mannel and S. Recksiegel, *Flavor changing neutral current decays of heavy baryons: The Case $\Lambda_b^0 \to \Lambda\gamma$*, J. Phys. **G24** (1998) 979, `arXiv:hep-ph/9701399`.

[45] Y.-m. Wang, Y. Li, and C.-D. Lu, *Rare Decays of $\Lambda_b^0 \to \Lambda\gamma$ and $\Lambda_b^0 \to \Lambda\ell^+\ell^-$ in the Light-cone Sum Rules*, Eur. Phys. J. **C59** (2009) 861, `arXiv:0804.0648`.

[46] T. Mannel and Y.-M. Wang, *Heavy-to-light baryonic form factors at large recoil*, Journal of High Energy Physics **2011** (2011) 67.

[47] L.-F. Gan, Y.-L. Liu, W.-B. Chen, and M.-Q. Huang, *Improved Light-cone QCD Sum Rule Analysis Of The Rare Decays $\Lambda_b \to \Lambda\gamma$ And $\Lambda_b \to \Lambda l^+ l^-$*, Commun. Theor. Phys. **58** (2012) 872, `arXiv:1212.4671`.

[48] R. N. Faustov and V. O. Galkin, *Rare $\Lambda_b \to \Lambda l^+ l^-$ and $\Lambda_b \to \Lambda\gamma$ decays in the relativistic quark model*, Phys. Rev. D **96** (2017) 053006.

[49] G. Buchalla, G. Isidori, and S. J. Rey, *Corrections of order Λ_{QCD}^2/m_c^2 to inclusive rare B decays*, Nucl. Phys. **B511** (1998) 594, `arXiv:hep-ph/9705253`.

[50] F. Legger, *Polarized radiative Λ_b decays at LHCb*, Tech. Rep. LHCb-2006-013. CERN-LHCb-2006-013, CERN, Geneva, Dec, 2006.

[51] C. Patrignani and P. D. Group, *Review of particle physics*, Chinese Physics C **40** (2016), no. 10 100001.

[52] LHCb collaboration, R. Aaij *et al.*, *Measurements of the $\Lambda_b^0 \to J/\psi\Lambda$ decay amplitudes and the Λ_b^0 polarisation in pp collisions at $\sqrt{s} = 7$ TeV*, Phys. Lett. **B724** (2013) 27, `arXiv:1302.5578`.

[53] L. Evans and P. Bryant, *Lhc machine*, Journal of Instrumentation **3** (2008), no. 08 S08001.

[54] LHCb collaboration, A. A. Alves Jr. *et al.*, *The LHCb detector at the LHC*, JINST **3** (2008) S08005.

[55] LHCb collaboration, *LHCb reoptimized detector design and performance: Technical Design Report*, CERN-LHCC-2003-030. LHCb-TDR-009.

[56] LHCb collaboration, R. Aaij *et al.*, *LHCb detector performance*, Int. J. Mod. Phys. **A30** (2015) 1530022, arXiv:1412.6352.

[57] LHCb collaboration, *LHCb VELO (VErtex LOcator): Technical Design Report*, CERN-LHCC-2001-011. LHCb-TDR-005.

[58] LHCb collaboration, *LHCb magnet: Technical Design Report*, CERN-LHCC-2000-007. LHCb-TDR-001.

[59] LHCb collaboration, *LHCb inner tracker: Technical Design Report*, CERN-LHCC-2002-029. LHCb-TDR-008.

[60] LHCb collaboration, *LHCb outer tracker: Technical Design Report*, CERN-LHCC-2001-024. LHCb-TDR-006.

[61] LHCb collaboration, *LHCb RICH: Technical Design Report*, CERN-LHCC-2000-037. LHCb-TDR-003.

[62] P. A. Cherenkov, *Visible emission of clean liquids by action of γ radiation*, Doklady Akademii Nauk SSSR **2** (1934) 451.

[63] LHCb collaboration, *LHCb calorimeters: Technical Design Report*, CERN-LHCC-2000-036. LHCb-TDR-002.

[64] A. Arefev *et al.*, *Beam Test Results of the LHCb Electromagnetic Calorimeter.*, Tech. Rep. LHCb-2007-149. CERN-LHCb-2007-149, CERN, Geneva, May, 2008. revised version submitted on 2008-05-15 09:09:53.

[65] LHCb collaboration, *LHCb muon system: Technical Design Report*, CERN-LHCC-2001-010. LHCb-TDR-004.

[66] M. Calvo Gomez *et al.*, *A tool for γ/π^0 separation at high energies*, Tech. Rep. LHCb-PUB-2015-016. CERN-LHCb-PUB-2015-016, CERN, Geneva, Aug, 2015.

[67] LHCb collaboration, R. Aaij *et al.*, *Measurement of forward J/ψ production cross-sections in pp collisions at $\sqrt{s} = 13$ TeV*, JHEP **10** (2015) 172, Erratum ibid. **05** (2017) 063, arXiv:1509.00771.

[68] LHCb collaboration, R. Aaij *et al.*, *Measurement of the ratio of branching fractions $\mathcal{B}(B^0 \to K^{*0}\gamma)/\mathcal{B}(B_s^0 \to \phi\gamma)$*, Phys. Rev. **D85** (2012) 112013, arXiv:1202.6267.

[69] F. Soomro and V. Belyaev, *HLT2 exclusive selections for $B_s \to \phi\gamma$ and $B_d \to K^*\gamma$*, Tech. Rep. LHCb-PUB-2010-007. CERN-LHCb-PUB-2010-007, CERN, Geneva, Feb, 2010.

[70] M. Williams *et al.*, *The HLT2 Topological Lines*, Tech. Rep. LHCb-PUB-2011-002. CERN-LHCb-PUB-2011-002, CERN, Geneva, Jan, 2011.

[71] A. Puig, *The HLT2 Radiative Topological Lines*, Tech. Rep. LHCb-PUB-2012-002. CERN-LHCb-PUB-2012-002, CERN, Geneva, Feb, 2012.

[72] T. Likhomanenko *et al.*, *LHCb Topological Trigger Reoptimization*, J. Phys. : Conf. Ser. **664** (2015) 082025. 8 p, 21st International Conference on Computing in High Energy Physics (CHEP2015).

[73] V. V. Gligorov and M. Williams, *Efficient, reliable and fast high-level triggering using a bonsai boosted decision tree*, Journal of Instrumentation **8** (2013), no. 02 P02013.

[74] L. Breiman, J. H. Friedman, R. A. Olshen, and C. J. Stone, *Classification and regression trees*, Wadsworth international group, Belmont, California, USA, 1984.

[75] LHCb collaboration, R. Aaij *et al.*, *Search for the rare decay $K_S^0 \to \mu^+\mu^-$*, JHEP **01** (2013) 090, arXiv:1209.4029.

[76] Particle Data Group, K. A. Olive *et al.*, *Review of particle physics*, Chin. Phys. **C38** (2014) 090001, and 2015 update.

[77] T. Skwarnicki, *A study of the radiative cascade transitions between the Upsilon-prime and Upsilon resonances*, PhD thesis, Institute of Nuclear Physics, Krakow, 1986, DESY-F31-86-02.

[78] G. Isidori, *Future prospects in kaon physics: some remarks*, Rare'n'Strange Workshop, CERN.

[79] P. Ilten, J. Thaler, M. Williams, and W. Xue, *Dark photons from charm mesons at LHCb*, Phys. Rev. **D92** (2015), no. 11 115017, arXiv:1509.06765.

[80] A. Lai *et al.*, *Observation of the decay $K_S^0 \to \pi^+\pi^- e^+ e^-$*, Physics Letters B **496** (2000), no. 3–4 137.

[81] J. R. Batley *et al.*, *Precision measurement of the ratio $\mathcal{B}(K_S^0 \to \pi^+\pi^- e^+ e^-)$ / $\mathcal{B}(K_L^0 \to \pi^+\pi^-\pi_d^0)$*, Physics Letters B **694** (2011), no. 4-5 301 .

[82] T. Sjöstrand, S. Mrenna, and P. Skands, *A brief introduction to PYTHIA 8.1*, Comput. Phys. Commun. **178** (2008) 852, arXiv:0710.3820.

[83] I. Belyaev *et al.*, *Handling of the generation of primary events in Gauss, the LHCb simulation framework*, J. Phys. Conf. Ser. **331** (2011) 032047.

[84] Geant4 collaboration, J. Allison *et al.*, *Geant4 developments and applications*, IEEE Trans. Nucl. Sci. **53** (2006) 270.

[85] A. Puig, *The LHCb trigger in 2011 and 2012*, LHCb-PUB-2014-046.

[86] X. Cid Vidal, D. Martinez Santos, and M.-O. Bettler, *Search for $K_s^0 \to \mu^+\mu^-$*, Tech. Rep. LHCb-ANA-2011-101, CERN, Geneva, Jul, 2012.

[87] S. S. Wilks, *The large-sample distribution of the likelihood ratio for testing composite hypotheses*, Ann. Math. Stat. **9** (1938) 60.

[88] C. Marin Benito, L. Garrido Beltran, and X. Cid Vidal, *Feasibility study of $K_S^0 \to \pi^+\pi^- e^+ e^-$ at LHCb*, Tech. Rep. LHCb-INT-2016-030. CERN-LHCb-INT-2016-030, CERN, Geneva, Sep, 2016.

[89] LHCb collaboration, *LHCb Trigger and Online Technical Design Report*, CERN-LHCC-2014-016. LHCb-TDR-016.

[90] LHCb collaboration, R. Aaij *et al.*, *Measurement of the Υ polarization in pp collisions at $\sqrt{s} = 7$ and 8 TeV*, arXiv:1709.01301, submitted to JHEP.

[91] F. Legger, A. Bay, and T. Schietinger, *Contribution to the Development of the LHCb acquisition electronics and Study of polarized radiative Λ_b decays*, 2006. Presented on 08 Sep 2006.

[92] A. Flandi, K. Trabelsi, and A. Puig Navarro, *Search for $\Lambda_b^0 \to \Lambda\gamma$ at LHCb*, tech. rep., EPFL, Laussane, 2015.

[93] T. Sjöstrand, S. Mrenna, and P. Skands, *PYTHIA 6.4 physics and manual*, JHEP **05** (2006) 026, arXiv:hep-ph/0603175.

[94] D. J. Lange, *The EvtGen particle decay simulation package*, Nucl. Instrum. Meth. **A462** (2001) 152.

[95] P. Golonka and Z. Was, *PHOTOS Monte Carlo: A precision tool for QED corrections in Z and W decays*, Eur. Phys. J. **C45** (2006) 97, `arXiv:hep-ph/0506026`.

[96] Geant4 collaboration, S. Agostinelli *et al.*, *Geant4: A simulation toolkit*, Nucl. Instrum. Meth. **A506** (2003) 250.

[97] M. Clemencic *et al.*, *The LHCb simulation application, Gauss: Design, evolution and experience*, J. Phys. Conf. Ser. **331** (2011) 032023.

[98] LHCb collaboration, *Study of the decay $B^+ \to K^+\pi^0$ at LHCb*, LHCb-CONF-2015-001.

[99] LHCb collaboration, R. Aaij *et al.*, *Observation of the suppressed decay $\Lambda_b^0 \to p\pi^-\mu^+\mu^-$*, JHEP **04** (2017) 029, `arXiv:1701.08705`.

[100] M. Pivk and F. R. Le Diberder, *sPlot: A statistical tool to unfold data distributions*, Nucl. Instrum. Meth. **A555** (2005) 356, `arXiv:physics/0402083`.

[101] F. Pedregosa *et al.*, *Scikit-learn: Machine learning in Python*, Journal of Machine Learning Research **12** (2011) 2825.

[102] R. E. Schapire and Y. Freund, *A decision-theoretic generalization of on-line learning and an application to boosting*, J. Comput. Syst. Sci. **55** (1997) 119.

[103] T. Chen and C. Guestrin, *Xgboost: A scalable tree boosting system*, in *Proceedings of the 22Nd ACM SIGKDD International Conference on Knowledge Discovery and Data Mining*, KDD '16, (New York, NY, USA), pp. 785–794, ACM, 2016. doi: 10.1145/2939672.2939785.

[104] G. Punzi, *Sensitivity of searches for new signals and its optimization*, in *Statistical Problems in Particle Physics, Astrophysics, and Cosmology* (L. Lyons, R. Mount, and R. Reitmeyer, eds.), p. 79, 2003. `arXiv:physics/0308063`.

[105] V. J. Rives Molina, A. Puig, and M. Calvo, *Study of b-hadron decays into two hadrons and a photon at LHCb and first observation of b-baryon radiative decays*, Jul, 2016. Presented 17 Oct 2016.

[106] LHCb collaboration, R. Aaij *et al.*, *Study of the kinematic dependences of Λ_b^0 production in pp collisions and a measurement of the $\Lambda_b^0 \to \Lambda_c^+\pi^-$ branching fraction*, JHEP **08** (2014) 143, `arXiv:1405.6842`.

[107] *Generation tables for Pythia8 Sim09* `MagUp` $\Lambda_b^0 \to \Lambda\gamma$ *MC*, `http://lhcb-release-area.web.cern.ch/LHCb-release-area/DOC/STATISTICS/SIM09STAT/RD-WG/Generation_Sim09-Beam6500GeV-2016-MagUp-Nu1.6-25ns-Pythia8.html#15102307`; *Generation tables for Pythia8 Sim09* `MagDown` $\Lambda_b^0 \to \Lambda\gamma$ *MC*, `http://lhcb-release-area.web.cern.ch/LHCb-release-area/DOC/STATISTICS/SIM09STAT/RD-WG/Generation_Sim09-Beam6500GeV-2016-MagDown-Nu1.6-25ns-Pythia8.html#15102307`.

[108] *Generation tables for Pythia8 Sim09* `MagUp` $B^0 \to K^{*0}\gamma$ *MC*, `http://lhcbdoc.web.cern.ch/lhcbdoc/STATISTICS/SIM09STAT/RD-WG/Generation_Sim09-Beam6500GeV-2016-MagUp-Nu1.6-25ns-Pythia8.html#11102202`; *Generation tables for Pythia8 Sim09* `MagDown` $B^0 \to K^{*0}\gamma$ *MC*, `http://lhcbdoc.web.cern.ch/lhcbdoc/STATISTICS/SIM09STAT/RD-WG/Generation_Sim09-Beam6500GeV-2016-MagDown-Nu1.6-25ns-Pythia8.html#11102202`.

[109] L. Anderlini *et al.*, *The PIDCalib package*, Tech. Rep. LHCb-PUB-2016-021. CERN-LHCb-PUB-2016-021, CERN, Geneva, Jul, 2016.

[110] LHCb collaboration, R. Aaij *et al.*, *Study of beauty hadron decays into pairs of charm hadrons*, Phys. Rev. Lett. **112** (2014) 202001, `arXiv:1403.3606`.

[111] V. Bellee, A. Puig Navarro, and K. Trabelsi, *Search for $B_s^0 \to \phi\phi\gamma$ at LHCb*, Tech. Rep. LHCb-INT-2015-024. CERN-LHCb-INT-2015-024, CERN, Geneva, Jun, 2015.

[112] ARGUS, H. Albrecht *et al.*, *Search for Hadronic $b \to u$ Decays*, Phys. Lett. **B241** (1990) 278.

[113] G. A. Cowan, D. C. Craik, and M. D. Needham, *RapidSim: an application for the fast simulation of heavy-quark hadron decays*, Comput. Phys. Commun. **214** (2017) 239, `arXiv:1612.07489`.

[114] LHCb collaboration, R. Aaij *et al.*, *Search for the $\Lambda_b^0 \to \Lambda\eta$ and $\Lambda_b^0 \to \Lambda\eta'$ decays with the LHCb detector*, JHEP **09** (2015) 006, `arXiv:1505.03295`.

[115] LHCb collaboration, *LHCb trigger system: Technical Design Report*, CERN-LHCC-2003-031. LHCb-TDR-010.

[116] R. Aaij *et al.*, *Performance of the LHCb calorimeters*, LHCb-DP-2013-004, in preparation.

[117] S. Tolk, J. Albrecht, F. Dettori, and A. Pellegrino, *Data driven trigger efficiency determination at LHCb*, Tech. Rep. LHCb-PUB-2014-039. CERN-LHCb-PUB-2014-039, CERN, Geneva, May, 2014.

[118] C. Marin Benito and A. Puig Navarro, *$\Lambda_b^0 \to \Lambda\gamma$ status report*, Presented at the Rare Decays meeting on 2018-08-30.

[119] A. Brossa Gonzalo, L. Garrido Beltrán, and C. Marin Benito, *$\Lambda_b^0 \to \Lambda\gamma$ search with Downstream Tracks and Secondary Vertex reconstruction at LHCb*, tech. rep., Universitat de Barcelona, Barcelona, 2017.

[120] W. D. Hulsbergen, *Decay chain fitting with a Kalman filter*, Nucl. Instrum. Meth. **A552** (2005) 566, `arXiv:physics/0503191`.

[121] J. F. Marchand, *$B_s^0 \to \phi\gamma$ using converted photons*, Presented at the Radiative Decays Workshop of 2014.

[122] D. A. Berninghoff, J. Albrecht, and V. Gligorov, *Bremsstrahlung Recovery of Electrons using Multivariate Methods*, Tech. Rep. LHCb-INT-2016-018. CERN-LHCb-INT-2016-018, CERN, Geneva, Apr, 2016.